Electroactive Polymer Composites:

Microscopic and Macroscopic Stability

Thesis submitted in partial fulfillment
of the requirements for the degree of
"DOCTOR OF PHILOSOPHY"

by

Stephan Rudykh

Submitted to the Senate of
Ben-Gurion University of the Negev

2012

Beer-Sheva

Electroactive Polymer Composites:

Microscopic and Macroscopic Stability

Thesis submitted in partial fulfillment

of the requirements for the degree of

"DOCTOR OF PHILOSOPHY"

by

Stephan Rudykh

Submitted to the Senate of

Ben-Gurion University of the Negev

Approved by the advisor

Approved by the Dean of the Kreitman School of Advanced Graduate Studies

2012

Beer-Sheva

This work was carried out under the supervision of

Professor Gal deBotton

Department of Mechanical Engineering,

Ben-Gurion University of the Negev,

Beer-Sheva, Israel

Acknowledgments

Now, when the mysterious journey is nearing its end and the mist of terra incognita has been scattered, revealing the beautiful detailed picture, there comes the time to thank those who stood behind me supporting and encouraging.

I am in deep debt to my parents, Ludmila and Alexander. They made many sacrifices so that I may pursue my education in the cruel times of the 1990's in Russia. To my deep sorrow, my father will not see the fruits of my work; he passed away just a few months ago.

I would like to thank my lovely wife Anastasia and our daughters Anna and Daria. I truly love you much more than this thesis, even though you may not believe so.

I would like to thank my advisor Prof. Gal deBotton - you have been like a father for me in the scientific world, introducing me to the mystery of mechanics (I recall the first lesson you gave me standing by the "historical" board and writing the basics of continuum mechanics...). Together we overcame the moments of desperation and celebrated the excitements of new discoveries... I have already started missing those days. I am sincerely grateful for all that I have learned from you and for you setting an example with your inexhaustible scientific curiosity. Gal, thank you!

I was lucky to get the chance of working with Prof. Kaushik Bhattacharya who advised me during my visit at Caltech. The semester I spent there was very special and provided me with an important experience of working in Prof. Bhattacharya's leading research group. We discussed many ideas and I believe that pursuing all of them would have led me to write several more theses. Truly, each discussion we had enriched and inspired me in a unique way.

Finally, I thank Prof. Katia Bertoldi for fruitful discussions of various problems on instabilities over the years via e-mails. At the very final stage of my study, I got the chance of working with Prof. Bertoldi in Harvard University, thanks to the financial support of the *BSF Prof. Rahamimoff Award for Young Scientists*. I thank Prof. Bertoldi for the kind invitation and the opportunity to be a part of the outstanding solid mechanics group.

From Beer-Sheva to Pasadena... on to Cambridge and back to Beer-Sheva, with the help of all the good people along the way - here I am to submit the manuscript!

Contents

List of Figures

Abstract

This thesis is concerned with theoretical aspects of instability development in heterogeneous dielectrics capable of large elastic deformations. A general instability criterion is introduced to identify the limiting case of large-scale or macroscopic instabilities. Multiscale instabilities are determined by application of Bloch-Floquet technique to periodic media. I begin with the purely mechanical case, and develop a criterion for the onset of macroscopic instabilities in spatial composites with randomly distributed aligned fibers. This states that the composite fails when the compression in the fiber direction reaches a certain value given by a compact explicit expression. The results are confirmed by 3-D finite element simulations for which a unique algorithm of instability onset identification was developed.

Motivated by experiments and possible applications, a coupled electromechanical analysis is conducted in terms of the physically relevant referential electric field as well as in terms of the electric displacement. In terms of the former, a closed form solution is derived for the macroscopic instabilities for the class of layered neo-Hookean dielectrics. A criterion for the onset of electromechanical multiscale instabilities for the layered composites with *anisotropic* phases is formulated too. These reveal the essential influence of the microstructure on the onset of instabilities. Specifically, it is found that

(i) *macroscopic* instabilities dominate at moderate volume fractions of the stiffer phase

(ii) *interface* instabilities appear at small volume fractions of the stiffer phase

(iii) instabilities of *finite* length scales comparable with the microstructure size, take place at large volume fractions of the stiffer phase

The instabilities of type (iii) do not appear in the purely mechanical case and dominate in the region of high stiffer phase volume fractions. The unstable domains evolve with an increase of the electric field: expand, meet, unite and create new unstable domains in a certain way.

Finally, an exact solution for thick spherical balloons subjected to inflating pressure and electric excitation is derived and possible applications of the observed instability phenomenon to micro-pumps is discussed.

Chapter 1

Introduction

1.1 Motivation

Electroactive polymers (EAPs) respond to external electric stimuli by changing their size and shape. These soft dielectrics can be utilized to convert electrical energy into mechanical work. As promising actuators, EAPs offer the benefits of light weight, short response time and simple principle of work. An example of an EAP planar actuator is shown in Fig. 1. The top and bottom surfaces are covered with compliant electrodes that enable to induce an electric field through the material thickness. The so-called *Maxwell stresses* induced by the electrostatic field act to reduce the material thickness and thanks to the Poisson's effect lead to in-plane extension of the material.
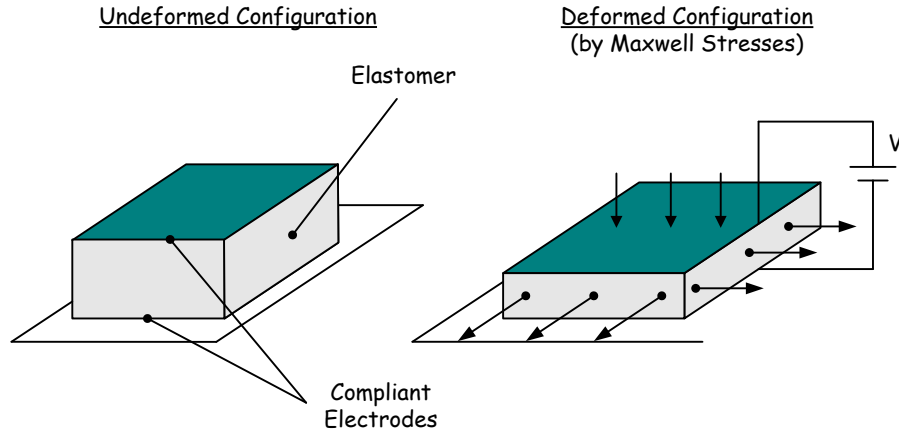
Fig. 1. A planar EAP actuator.

The field of EAPs has been intensively studied experimentally and theoretically in the last decade and consequently have now become feasible to use as actuators (Pelrine et al., 2000; Bar-Cohen, 2001; Bhattacharya et al., 2001; Lacour et al., 2004; Carpi and DeRossi, 2005; Carpi et al., 2007; O'Halloran et al., 2008; Stoyanov et al., 2011). However, in spite of the significant progress, these materials are limited by the extremely strong electric fields they require for meaningful actuation. The reason for this is the poor electromechanical coupling in typical polymers which have a limited ratio of dielectric to elastic modulus. One approach to tackle this issue is to make electroac-

tive polymer composites (EAPC) by combining an elastomer with a high dielectric or even conductive material (Zhang et al., 2002; Huang et al., 2004). This approach has shown to be promising in several experiments (e.g., Huang and Zhang, 2004; Stoyanov et al., 2011). Moreover, theoretical estimations (deBotton et al., 2007; Tian et al., 2012; Rudykh et al., 2011) have shown that the experimental results are only a beginning, and proper optimization of microstructures can lead to orders of magnitude improvement in the electromechanical coupling.

An important aspect of the EAPC behavior concerns the possible development of instabilities under certain electromechanical loading conditions. On one hand, instabilities are commonly considered as negative phenomena associated with failure. On the other, they can be viewed as a trigger for giant deformations of specific structures (Mockensturm and Goulbourne, 2006; Rudykh et al., 2012b) or for manipulating microstructural patterns in composite media (Singamaneni et al., 2009, for purely mechanical case). The latter can be utilized for controlling material properties, with a large variety of possible applications such as wave guide filtering (Gei et al., 2010).

Before tackling the more complex problem of coupled instabilities, herein the corresponding purely mechanical problem is investigated. A fundamental study of mechanical instabilities in composite materials was performed by Biot (1965), who developed a theory for pre-stressed rubber-like solids in finite deformation. Rosen (1965) estimated the compressive strength of fiber composites based on a beam theory. A general discussion concerning the bifurcation phenomena was provided by Hill and Hutchinson (1975). Among the methods that take into account imperfections in fiber composites one should mention the works of Budiansky (1983); Fleck (1997) and Merodio and Pence (2001). The problem of a localized failure at the free surface of orthotropic materials was examined by deBotton and Schulgasser (1996).

In composite materials, bifurcations may occur at a scale which is significantly smaller than the size of the specimen. Triantafyllidis and Maker (1985) determined the onset of purely mechanical instabilities in periodic layered media at such *microscopic* levels, as well as at the *macroscopic* level. These investigators noted that macroscopic instabilities that occur at a scale significantly larger than the scale of the microstructure can be detected with the help of the homogenized tensor of elastic moduli. The onset of these instabilities is associated with loss of ellipticity of the homogenized governing equations. Detecting instabilities at a smaller scale requires the use of more complicated techniques such as Bloch wave analysis (*e.g.*, Kittel, 2004). Geymonat et al. (1993) showed that Floquet theorem or Bloch wave technique can be applied for analyzing the characteristic unit cell and predicting the onset of failures at any scale.

Nestorovic and Triantafyllidis (2004) determined loss of stability in 2-D layered com-

posites subjected to combined shear and compression. Periodic fiber composites subjected to in-plane *transverse* deformation were numerically examined by Triantafyllidis et al. (2006) for the case of neo-Hookean phases, and by Bertoldi and Boyce (2008) for both neo-Hookean and Gent phases. Michel et al. (2007) compared numerical results for the transverse behavior and loss of stability of periodic porous fiber composites with corresponding predictions of the variational estimate of Lopez-Pamies and Ponte Castañeda (2004). The 2-D finite element (FE) analyses performed in the above mentioned works did not cover instabilities due to compression *along* the fibers. In this work the onset of this important mode of failure (*e.g.,* Merodio and Ogden, 2002; Qiu and Pence, 1997) is analyzed. A numerical analysis requires examination of 3-D models subjected to finite-strain loading conditions. Accordingly, in contrast to the FE models used in previous works, a 3-D model is developed and appropriate techniques are applied for determining the onset of instabilities. Complementary to the numerical study, analytical predictions for the onset of stability loss in composites with random distribution of aligned fibers are determined. An important result of the study of the purely mechanical stability is that *the onset of macroscopic instability occurs whenever the compression in the fiber direction reaches the stretch ratio*

$$\lambda_n = \left(1 - \frac{\tilde{\mu}}{\bar{\mu}}\right)^{1/3},\tag{1}$$

where $\tilde{\mu}$ and $\bar{\mu}$ are the out-of-plane and isochoric shear moduli of the composite. This result was reported by deBotton (2008); Rudykh and deBotton (2012) and Agoras et al. (2009b). Additionally, a new upper estimate for composites with *Gent* phases is introduced. Differently from the results of Agoras et al. (2009b), an analytical closed form expression is derived for the onset of instabilities in these composites.

Towards the treatment of the coupled electromechanical problem, I recall that the basic theory of elastic dielectrics that accounts for the Maxwell electrostatic stresses was introduced by Toupin (1956). More recently, McMeeking and Landis (2005), Dorfmann and Ogden (2005) and Suo et al. (2008) extended this theory.

While purely mechanical instabilities have been studied intensively for decades, the coupled instability is a new topic and no results were available until lately. Electromechanical instabilities such as pull-in instabilities (Plante and Dubowsky, 2006), electrical breakdown (Kofod et al., 2003; Stoyanov et al., 2011) and failure mechanisms at high electric fields (Wang et al., 2011) in homogeneous electroactive materials were studied experimentally. Liu et al. (2010) and Molberg et al. (2010) investigated the electrical breakdown of EAP composites with random distribution of high dielectric particles.

Dorfmann and Ogden (2010) examined the problem of surface instabilities accounting for the incremental governing equations in *isotropic* dielectrics. Recently, Bertoldi
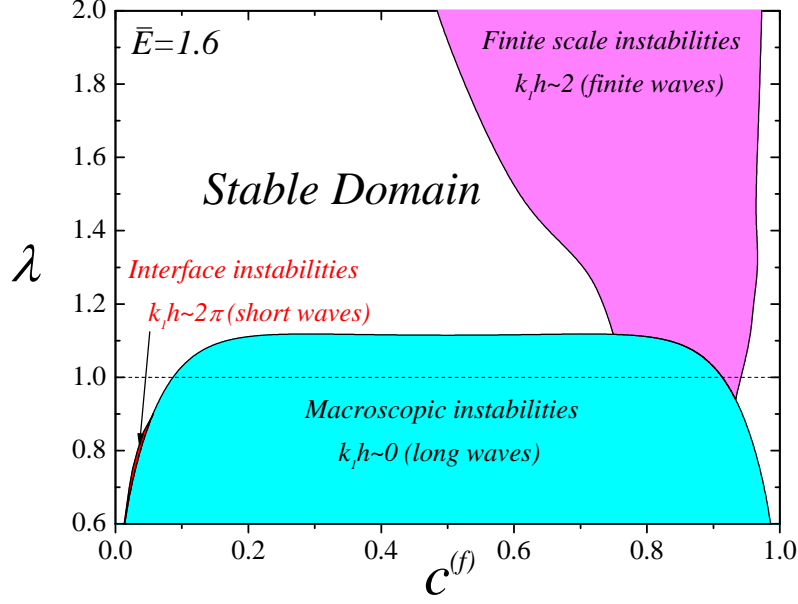
Fig. 2. The unstable domains of layered soft dielectric subjected to an electric excitation and pre-stretch λ. A different types of instabilities and their domains are presented as functions of the volume fraction of the stiffer phase $c^{(f)}$.

and Gei (2011) investigated instabilities in soft layered dielectrics with isotropic phases in which the electric field is perpendicular to the layers and pre-stretch is applied along the layers. It is worth reminding that for this configuration no enhancement of the actuation due to heterogeneity can be achieved. In contrast to this, when one of the phases is anisotropic a significant enhancement of up to two orders of magnitude can be achieved (Tevet-Deree, 2008; Tian et al., 2012; Rudykh et al., 2011). This motivates the investigation of the onset of instabilities in composites with *anisotropic* phases.

In the context of macroscopic instabilities, an extension of the work by Dorfmann and Ogden (2010) to a general class of *multiphase* electroactive materials undergoing large deformations is introduced. Herein, a *general criterion* for the onset of macroscopic instability in anisotropic media for planar problems is developed.

Previous works (Dorfmann and Ogden, 2010; Bertoldi and Gei, 2011) involve the electrical displacement as a primary variable. However, this mathematically convenient approach demands from experimentalists to control surface charge. This task is rather difficult and hardly likely to be adopted in future since in potential applications the electric excitation is induced by voltage. Contrary to the above mentioned works, in this study the analysis is conducted in terms of a comprehensive variable, namely the referential electric field. The latter is directly related to the applied voltage $\Delta\phi$ as $E^0 = \Delta\phi/d$, where d is the distance between the electrodes in the undeformed configuration.

Beyond the practicality of the proposed concept, it reveals a few important aspects of

the behavior that are hard to capture by making use of the "surface charge" formulation. Among these are the identification of critical morphologies for which the composite becomes extremely unstable and determination of critical voltages above which the medium loses its stability or, conversely, becomes stable. The major result of this study may be summarized as follow: *in layered electroactive media three primary modes of instabilities can be distinguished. These are characterized by different wavelengths and are allocated depending on the composite morphology.* These modes are shown in Fig. 2 as functions of the pre-stretch λ and the volume fraction of the stiffer phase $c^{(f)}$.

(i) The first mode is characterized by instabilities at long wavelengths and dominates at moderate volume fractions of the stiffer phase.

(ii) The second mode corresponds to instabilities at short wavelengths and appears at low volume fractions of the stiffer phase.

(iii) The third mode represents instabilities at finite wavelengths comparable with the microstructure characteristic size. The instabilities of this mode occur at high volume fractions of the stiffer phase.

The unstable domains evolve with the applied electric field: expand, meet, unite and create new unstable domains in a certain way such that the overall unstable domain extends with an increase of the electric field. The morphology and geometry of the microstructure significantly impact the onset of instabilities.

The results for the purely mechanical instabilities in fiber composites are summarized in Chapter 2 and are based on the work of Rudykh and deBotton (2012). The analysis of electromechanical instabilities in anisotropic soft dielectrics with application to layered media (Rudykh and deBotton, 2011) is presented in Chapter 3. The results related to multiscale electromechanical instabilities (Rudykh et al., 2012a) are summarized in Chapter 4. An example of usage of the electromechanical instability phenomenon with possible application for micro-pumps is demonstrated in Chapter 5. The results of the last chapter rely on the work of Rudykh et al. (2012b).

1.2   General Theoretical Background

The Cartesian position vector of a material point in a reference configuration of a body $\mathscr{B}_0$ is $\mathbf{X}$, and its position vector in the deformed configuration $\mathscr{B}$ is $\mathbf{x}$. The deformation of the body is characterized by the mapping

$$\mathbf{x} = \boldsymbol{\chi}(\mathbf{X}). \tag{2}$$

The deformation gradient is

$$\mathbf{F} = \frac{\partial \boldsymbol{\chi}(\mathbf{X})}{\partial \mathbf{X}}. \tag{3}$$

It is assumed that the deformation is invertible and hence $\mathbf{F}$ is non-singular, accordingly

$$J \equiv \det \mathbf{F} \neq 0. \tag{4}$$

Physically, J is the volume ratio between the volumes of an element in the deformed and the reference configurations, and hence $J = \frac{dv}{dV} > 0$.

The differential operators in the reference configuration are denoted $\mathrm{Div}(\bullet)$ and $\mathrm{Curl}(\bullet)$ and the corresponding operators in the current configuration are $\mathrm{div}(\bullet)$ and $\mathrm{curl}(\bullet)$, respectively. The deformation is assumed to be quasi-static and no magnetic field is assumed to be present. Consequently, Maxwell equations reduce to

$$\mathrm{div}\mathbf{D} = 0, \quad \mathrm{curl}\mathbf{E} = 0. \tag{5}$$

Here $\mathbf{D}$ is the electric displacement and $\mathbf{E}$ is the electric field in the *current* configuration.

Following Dorfmann and Ogden (2005), these equations can be rewritten in terms of the referential electric field $\mathbf{E}^0 = \mathbf{F}^T \mathbf{E}$ and the referential electric displacement $\mathbf{D}^0 = J\mathbf{F}^{-1}\mathbf{D}$ as

$$\mathrm{Div}\mathbf{D}^0 = 0 \quad \text{and} \quad \mathrm{Curl}\mathbf{E}^0 = 0. \tag{6}$$

In the absence of body forces the equilibrium equation is

$$\mathrm{Div}\mathbf{P} = 0, \tag{7}$$

where $\mathbf{P}$ is the *total* nominal stress tensor which is the sum of purely elastic and electrostatically induced Maxwell stresses. The corresponding total true or Cauchy stress tensor is related to the nominal stress tensor via the relation $\boldsymbol{\sigma} = J^{-1}\mathbf{P}\mathbf{F}^T$.

Consider hyperelastic dielectrics whose behaviors are characterized by a scalar-valued energy-density function $\Psi(\mathbf{F}, \mathbf{E}^0)$

$$\mathbf{P} = \frac{\partial \Psi(\mathbf{F}, \mathbf{E}^0)}{\partial \mathbf{F}} \quad \text{and} \quad \mathbf{D}^0 = -\frac{\partial \Psi(\mathbf{F}, \mathbf{E}^0)}{\partial \mathbf{E}^0} \tag{8}$$

For an incompressible material the nominal stress tensor is

$$\mathbf{P} = \frac{\partial \Psi(\mathbf{F}, \mathbf{E}^0)}{\partial \mathbf{F}} - p\mathbf{F}^{-T}, \tag{9}$$

where p is an arbitrary pressure.

The boundary conditions are

$$[[\mathbf{u}]] = \mathbf{0}, \quad [[\boldsymbol{\sigma}]] \cdot \mathbf{n} = \mathbf{0}, \quad [[\mathbf{D}]] \cdot \mathbf{n} = 0 \quad \text{and} \quad \mathbf{n} \times [[\mathbf{E}]] = \mathbf{0}, \tag{10}$$
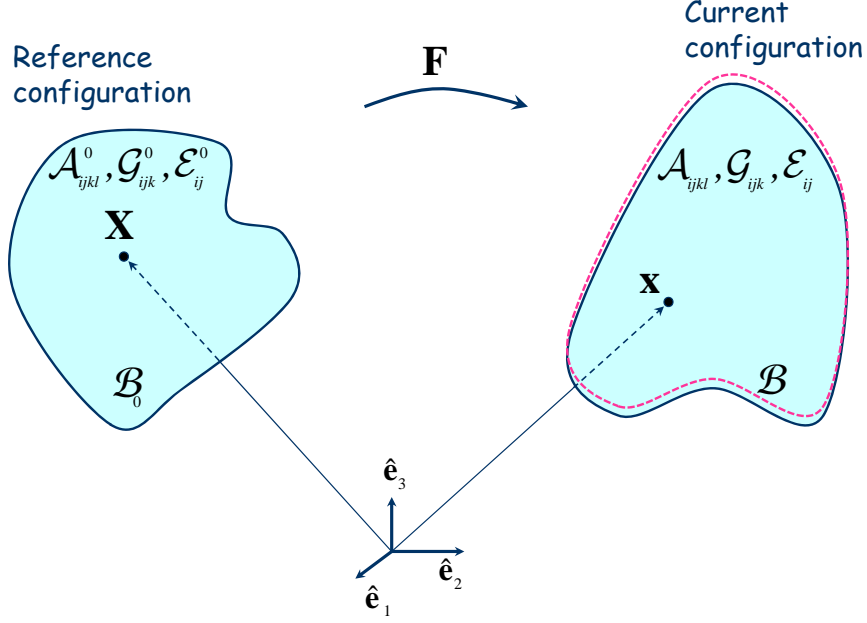
Fig. 3. The kinematics of the incremental changes in the fields.

where $\mathbf{u} = \mathbf{x} - \mathbf{X}$ is the displacement vector and $\mathbf{n} = J\mathbf{F}^{-T}\hat{\mathbf{N}}$ is normal to the boundary at the current configuration. The notation $[[\bullet]] \equiv (\bullet)^+ - (\bullet)^-$ denotes the jump between the fields in the material and surrounding across the boundary. In general, the body may be surrounded by another material as in the case of a multiphase medium, or by vacuum in the case of an isolated body.

The incremental governing equations are (Dorfmann and Ogden, 2010)

$$\mathrm{Div}\dot{\mathbf{P}} = 0, \quad \mathrm{Div}\dot{\mathbf{D}}^0 = 0 \quad \text{and} \quad \mathrm{Curl}\dot{\mathbf{E}}^0 = 0. \tag{11}$$

where $\dot{\mathbf{P}}$, $\dot{\mathbf{D}}^0$ and $\dot{\mathbf{E}}^0$ are infinitesimal changes in the nominal stress, electric displacement and electrical field, respectively. The linearized constitutive equations are provided via the electroelastic moduli tensors

$$\mathcal{A}^0_{i\alpha k\beta} = \frac{\partial^2 \Psi}{\partial F_{i\alpha}\partial F_{k\beta}}, \quad \mathcal{G}^0_{i\alpha\beta} = \frac{\partial^2 \Psi}{\partial F_{i\alpha}\partial E^0_\beta} \quad \text{and} \quad \mathcal{E}^0_{\alpha\beta} = \frac{\partial^2 \Psi}{\partial E^0_\alpha\partial E^0_\beta}, \tag{12}$$

namely,

$$\dot{P}_{ij} = \mathcal{A}^0_{ijkl}\dot{F}_{kl} + \mathcal{G}^0_{ijk}\dot{E}^0_k \quad \text{and} \quad -\dot{D}^0_i = \mathcal{G}^0_{jki}\dot{F}_{jk} + \mathcal{E}^0_{ij}\dot{E}^0_j. \tag{13}$$

For an incompressible material the linearized constitutive relations are

$$\dot{P}_{ij} = \mathcal{A}^0_{ijkl}\dot{F}_{kl} + \mathcal{G}^0_{ijk}\dot{E}^0_k - \dot{p}F^{-T}_{ij} + pF^{-1}_{jk}\dot{F}_{kl}F^{-1}_{li}, \quad -\dot{D}^0_i = \mathcal{G}^0_{jki}\dot{F}_{jk} + \mathcal{E}^0_{ij}\dot{E}^0_j, \tag{14}$$

where $\dot{p}$ is an incremental change in pressure. Consider the current configuration as a new reference configuration (see Fig. 3). Recall that $\dot{\mathbf{F}} = (\mathrm{grad}\,\mathbf{v})\mathbf{F}$, where $v_i = \dot{x}_i$ is

an incremental displacement. The incremental "push-forward" of $\dot{\mathbf{P}}$, $\dot{\mathbf{E}}^0$ and $\dot{\mathbf{D}}^0$ to the current configuration are

$$\dot{\mathbf{T}} = J^{-1}\dot{\mathbf{P}}\mathbf{F}^T, \quad \dot{\mathbf{D}} = J^{-1}\mathbf{F}\dot{\mathbf{D}}^0 \quad \text{and} \quad \dot{\mathbf{E}} = \mathbf{F}^{-T}\dot{\mathbf{E}}^0. \tag{15}$$

In terms of these increments, the linearized constitutive equations are

$$\dot{T}_{ij} = \mathcal{A}_{ijkl}v_{k,l} + \mathcal{G}_{ijk}\dot{E}_k - \dot{p}\delta_{ij} + pv_{j,i}, \quad -\dot{D}_i = \mathcal{G}_{jki}v_{j,k} + \mathcal{E}_{ij}\dot{E}_j, \tag{16}$$

where

$$\mathcal{A}_{ijkl} = J^{-1}F_{j\alpha}F_{l\beta}\mathcal{A}^0_{i\alpha k\beta}, \quad \mathcal{G}_{ijk} = J^{-1}F_{j\alpha}F_{k\beta}\mathcal{G}^0_{i\alpha\beta}, \quad \mathcal{E}_{ij} = J^{-1}F_{i\alpha}F_{j\beta}\mathcal{E}^0_{\alpha\beta}. \tag{17}$$

The electroelastic moduli possess the symmetries

$$\mathcal{A}_{ijkl} = \mathcal{A}_{klij}, \quad \mathcal{G}_{ijk} = \mathcal{G}_{jik} \quad \text{and} \quad \mathcal{E}_{ij} = \mathcal{E}_{ji}. \tag{18}$$

The incremental governing equations (11) become

$$\operatorname{div}\dot{\mathbf{T}} = 0, \quad \operatorname{div}\dot{\mathbf{D}} = 0 \quad \text{and} \quad \operatorname{curl}\dot{\mathbf{E}} = 0. \tag{19}$$

Upon substitution of the linearized relations (16) in (19), the following equations are obtained

$$\mathcal{A}_{ijkl}v_{k,lj} + \mathcal{G}_{ijk}\dot{E}_{k,j} - \dot{p}_{,i} = 0 \quad \text{and} \quad \mathcal{G}_{jki}v_{j,ki} + \mathcal{E}_{ij}\dot{E}_{j,i} = 0. \tag{20}$$

The boundary conditions of the incremental fields are

$$[[\mathbf{v}]] = \mathbf{0}, \quad [[\dot{\mathbf{T}}]] \cdot \mathbf{n} = \mathbf{0}, \quad [[\dot{\mathbf{D}}]] \cdot \mathbf{n} = 0 \quad \text{and} \quad \mathbf{n} \times [[\dot{\mathbf{E}}]] = 0. \tag{21}$$

While Eqs. (5), (7) and (8) together with boundary conditions (10) define the electromechanical boundary value problem, possible bifurcations of the solution are analyzed by making use of the incremental Eqs. (19) together with boundary conditions (21).

Alternatively, an energy density function Φ can be written in terms of independent variables $\mathbf{F}$ and $\mathbf{D}^0$ (Dorfmann and Ogden, 2005) such that

$$\mathbf{P} = \frac{\partial\Phi(\mathbf{F}, \mathbf{D}^0)}{\partial\mathbf{F}} \quad \text{and} \quad \mathbf{E}^0 = \frac{\partial\Phi(\mathbf{F}, \mathbf{D}^0)}{\partial\mathbf{D}^0}. \tag{22}$$

Then the linearized constitutive equations are

$$\dot{P}_{ij} = \mathcal{A}^0_{ijkl}\dot{F}_{kl} + \mathcal{K}^0_{ijk}\dot{D}^0_k \quad \text{and} \quad \dot{E}^0_i = \mathcal{K}^0_{jki}\dot{F}_{jk} + \mathcal{D}^0_{ij}\dot{D}^0_j, \tag{23}$$

where

$$\mathcal{K}^0_{i\alpha\beta} = \frac{\partial^2\Phi}{\partial F_{i\alpha}\partial D^0_\beta} \quad \text{and} \quad \mathcal{D}^0_{\alpha\beta} = \frac{\partial^2\Phi}{\partial D^0_\alpha\partial D^0_\beta}. \tag{24}$$

9

For an incompressible material the incremental change in the nominal stress tensor is

$$\dot{P}_{ij} = \mathcal{A}^0_{ijkl}\dot{F}_{kl} + \mathcal{K}^0_{ijk}\dot{D}^0_k - \dot{p}F^{-T}_{ij} + pF^{-1}_{jk}\dot{F}_{kl}F^{-1}_{li}. \tag{25}$$

The corresponding "push-forward" increments are

$$\dot{T}_{ij} = \mathcal{A}_{ijkl}v_{k,l} + \mathcal{K}_{ijk}\dot{D}_k - \dot{p}\delta_{ij} + pv_{j,i}, \quad \dot{E}_i = \mathcal{K}_{jki}v_{j,k} + \mathcal{D}_{ij}\dot{D}_j, \tag{26}$$

where

$$\mathcal{K}_{ijk} = F_{j\alpha}F^{-1}_{\beta k}\mathcal{K}^0_{i\alpha\beta}, \quad \mathcal{D}_{ij} = JF^{-1}_{\alpha i}F^{-1}_{\beta j}\mathcal{D}^0_{\alpha\beta}. \tag{27}$$

Similar to (18), the moduli possess the symmetries

$$\mathcal{K}_{ijk} = \mathcal{K}_{jik} \quad \text{and} \quad \mathcal{D}_{ij} = \mathcal{D}_{ji}. \tag{28}$$

Chapter 2

Macroscopic Stability of Fiber Composites

Composite materials are widely used in various engineering areas. Therefore characterization of their properties is of importance for both engineering applications and theoretical development of methods that can reduce the need for high-cost experiments. An important and hard to predict characteristic is the one associated with loss of stability, also referred to as "local buckling". This phenomenon is mostly considered as a failure mode that should be predicted and avoided. However, in some cases, such as in "snap-through" mechanisms this phenomenon can be used for our benefit (*e.g.,* O'Halloran et al., 2008). In this chapter, only purely mechanical instabilities are considered.

2.1 Theory

In the purely mechanical case the energy-density function Ψ of an isotropic material can be expressed in terms of the three invariants of the Cauchy-Green strain tensor $\mathbf{C} \equiv \mathbf{F}^T\mathbf{F}$. It is common to express these invariants in the form

$$I_1 = \text{Tr}\mathbf{C}, \quad I_2 = \frac{1}{2}(I_1^2 - \text{Tr}(\mathbf{C}^2)), \quad I_3 = \det\mathbf{C}. \tag{29}$$

A widely used isotropic and incompressible model that enables to capture the "lock-up" effect of the molecular chain extension limit is the Gent (1996) model (*e.g.,* Horgan and Saccomandi (2002))

$$\Psi_G = -\frac{1}{2}\mu J_m \ln\left(1 - \frac{I_1 - 3}{J_m}\right). \tag{30}$$

Here μ is the initial shear modulus and J_m is a dimensionless *locking parameter* corresponding to the lock-up phenomenon such that in the limit $(I_1 - 3) \to J_m$, there is a dramatic rise of the stresses and the material locks up. In the limit $J_m \to \infty$ this model is reduced to the neo-Hookean model, namely

$$\Psi_H = \frac{\mu}{2}\left(I_1 - 3\right). \tag{31}$$

The strain energy-density function of a transversely isotropic (TI) material, whose preferred direction in the reference configuration is along the unit vector $\hat{\mathbf{N}}$, depends on two additional invariants

$$I_4 = \hat{\mathbf{N}} \cdot \mathbf{C}\hat{\mathbf{N}} \quad \text{and} \quad I_5 = \hat{\mathbf{N}} \cdot \mathbf{C}^2\hat{\mathbf{N}}. \tag{32}$$
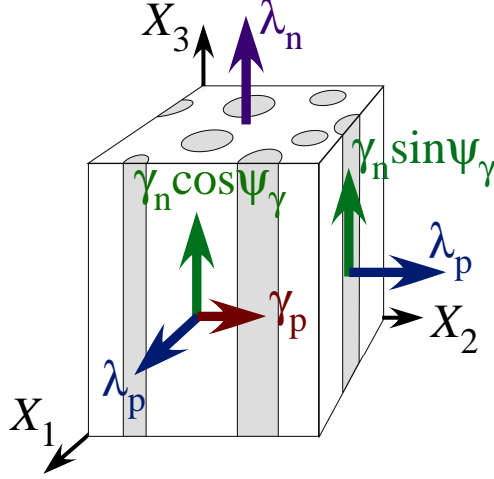
Fig. 4. A scheme of a transversely isotropic composite and the associated physically motivated invariants.

Following Ericksen and Rivlin (1954), an alternative set of invariants was proposed in deBotton et al. (2006), namely

$$\lambda_n^2 = I_4, \tag{33}$$

$$\lambda_p^2 = \sqrt{\frac{I_3}{I_4}}, \tag{34}$$

$$\gamma_n^2 = \frac{I_5}{I_4} - I_4, \tag{35}$$

$$\gamma_p^2 = I_1 - \frac{I_5}{I_4} - 2\sqrt{\frac{I_3}{I_4}}. \tag{36}$$

The fifth invariant ψ_γ, whose exact expression is given in deBotton et al. (2006), is the only invariant that depends on I_2 . The reverse relations can be readily obtained. The motivation for this set of invariants stems from the fact that they can be associated with specific modes of deformation. Thus, λ_n is the stretch measure along the preferred direction $\hat{\mathbf{N}}$, λ_p is the measure of the in-plane transverse dilatation, γ_n is the measure of the amount of out-of-plane shear, and γ_p is the amount of shear in the transverse plane. The fifth invariant ψ_γ describes the coupling between the shearing modes. A schematic drawing of the physical interpretation of these invariants is given in Fig. 4.

Following Ogden (1997) and Merodio and Ogden (2002), the tensor of elastic moduli is defined as

$$\boldsymbol{\mathcal{A}^0} = \frac{\partial \mathbf{P}}{\partial \mathbf{F}}. \tag{37}$$

Accordingly, the 1st Piola-Kirchhoff stress increment is

$$\delta \mathbf{P} = \boldsymbol{\mathcal{A}^0} \delta \mathbf{F}, \tag{38}$$

12

where $\delta\mathbf{F}$ is an infinitesimal variation in the deformation gradient from the current configuration. If the deformation is homogeneous then $\mathcal{A}^0_{i\alpha j\beta}$ is independent of $\mathbf{X}$ and the incremental equilibrium equation can be written in the form

$$\mathcal{A}^0_{i\alpha j\beta}\frac{\partial^2\delta\chi_j}{\partial X_\alpha \partial X_\beta} = 0, \tag{39}$$

where $\boldsymbol{\delta\chi}$ is the incremental displacement associated with $\delta\mathbf{F}$. For incompressible materials the equilibrium equation is

$$\mathcal{A}^0_{i\alpha j\beta}\frac{\partial^2\delta\chi_j}{\partial X_\alpha \partial X_\beta} + \frac{\partial\delta p}{\partial x_i} = 0, \tag{40}$$

where δp is a pressure increment. Incompressibility implies zero divergence of the displacement field, that is

$$\nabla \cdot \boldsymbol{\delta\chi} = 0. \tag{41}$$

I seek a solution for Eq. (40) in the form of a standing plane wave, namely

$$\boldsymbol{\delta\chi} = \hat{\mathbf{v}}f(\mathbf{x}\cdot\hat{\mathbf{a}}), \quad \delta p = qf(\mathbf{x}\cdot\hat{\mathbf{a}}), \tag{42}$$

where $\hat{\mathbf{v}}$ and $\hat{\mathbf{a}}$ are two unit vectors. Function f represents the disturbance shape and should be sufficiently continuously differentiable. To ensure the property the function is chosen to be an exponential function

$$\boldsymbol{\delta\chi} = \hat{\mathbf{v}}e^{i\hat{\mathbf{a}}\cdot\mathbf{x}}, \quad \delta p = qe^{i\hat{\mathbf{a}}\cdot\mathbf{x}}. \tag{43}$$

Note that for both forms of the solution, either for general form f or the exponential form (43), the identical condition is derived. The incompressibility constraint Eq. (41) leads to the requirement

$$\hat{\mathbf{a}} \cdot \hat{\mathbf{v}} = 0. \tag{44}$$

By application of the chain rule, the incremental equilibrium equations (40) can be written in the form

$$\mathcal{A}_{ipjq}\frac{\partial^2\delta\chi_j}{\partial x_p \partial x_q} + \frac{\partial\delta p}{\partial x_i} = 0, \tag{45}$$

where

$$\mathcal{A}_{ipjq} = J^{-1}F_{p\alpha}F_{q\beta}\mathcal{A}^0_{i\alpha j\beta}. \tag{46}$$

Substitution of Eq. (43) into Eq. (45) results in the equation

$$\mathbf{Q}\hat{\mathbf{v}} + iq\hat{\mathbf{a}} = 0, \tag{47}$$

where

$$Q_{ij} \equiv \mathcal{A}_{piqj}\hat{a}_p\hat{a}_q, \tag{48}$$

13

is the acoustic tensor.

Finally, I note that the ellipticity condition implies that $Q_{ij}\hat{v}_i\hat{v}_j \neq 0$ for all vectors $\hat{\mathbf{a}}$ and $\hat{\mathbf{v}}$ such that $\hat{\mathbf{a}} \otimes \mathbf{v} \neq 0$. However, since negative values of $Q_{ij}\hat{v}_i\hat{v}_j$ are not physical, the strong ellipticity conditions can be written as

$$Q_{ij}\hat{v}_i\hat{v}_j > 0. \tag{49}$$

The unit vector $\mathbf{v}$ is the normal to a surface, in the deformed configuration, which is referred to as a *weak surface* (*e.g.*, Merodio and Ogden (2002)). Once the critical deformation corresponding to the onset of ellipticity loss is achieved, the deformation in the weak surface occurs along the direction of the vector $\hat{\mathbf{a}}$.

2.2 Fiber Reinforced Composites

The strain energy-density function of a n-phase composite is

$$\Psi(\bar{\mathbf{F}}, \mathbf{X}) = \sum_{r=1}^{n} \varphi^{(r)}(\mathbf{X})\Psi^{(r)}(\mathbf{F}), \tag{50}$$

where

$$\varphi^{(r)}(\mathbf{X}) = \begin{cases} 1 & \text{if } \mathbf{X} \in \mathscr{B}_0^{(r)}, \\ 0 & \text{otherwise}, \end{cases} \tag{51}$$

In Eq. (51) $\mathscr{B}_0^{(r)}$ denotes the domain occupied by r-phase. The volume fraction of the r-phase is

$$c^{(r)} = \int_{\mathscr{B}_0} \varphi^{(r)}(\mathbf{X})dV. \tag{52}$$

Following the works of Hill (1972) and Ogden (1974), I apply homogeneous boundary conditions $\mathbf{x} = \mathbf{F}_0\mathbf{X}$ on the boundary of the composite $\partial\mathscr{B}_0$, where $\mathbf{F}_0$ is a constant matrix with $\det \mathbf{F}_0 > 0$. It can be shown that $\bar{\mathbf{F}} = \mathbf{F}_0$ where

$$\bar{\mathbf{F}} = \frac{1}{V}\int_{\mathscr{B}_0} \mathbf{F}(\mathbf{X})dV, \tag{53}$$

is the average deformation gradient. The average 1st Piola-Kirchhoff stress tensor is

$$\bar{\mathbf{P}} = \frac{1}{V}\int_{\mathscr{B}_0} \mathbf{P}(\mathbf{X})dV. \tag{54}$$

By application of the principle of minimum energy, the *effective* strain energy-density function is

$$\tilde{\Psi}(\bar{\mathbf{F}}) = \inf_{\mathbf{F}\in\mathcal{K}(\bar{\mathbf{F}})} \left\{ \frac{1}{V}\int_{\mathscr{B}_0} \Psi(\mathbf{F}, \mathbf{X})dV \right\}, \tag{55}$$

where $\mathcal{K}(\mathbf{F}) \equiv \left\{ \mathbf{F} \mid \mathbf{F} = \dfrac{\partial \boldsymbol{\chi}(\mathbf{X})}{\partial \mathbf{X}}, \mathbf{X} \in \mathscr{B}_0; \boldsymbol{\chi}(\mathbf{X}) = \bar{\mathbf{F}}\mathbf{X}, \mathbf{X} \in \partial\mathscr{B}_0 \right\}$ is the set of kinematically admissible deformation gradients. The corresponding macroscopic constitutive relation is

$$\bar{\mathbf{P}} = \frac{\partial \tilde{\Psi}(\bar{\mathbf{F}})}{\partial \bar{\mathbf{F}}}. \tag{56}$$

Generally, application of the variational principle (55) to heterogeneous materials can lead to bifurcations corresponding to dramatic changes in the nature of the solution to the optimization problem. As discussed by Triantafyllidis and Maker (1985) and Geymonat et al. (1993), these instabilities may occur at different wavelengths ranging from the size of a typical heterogeneity to that of the entire composite specimen. The calculation of microscopic instabilities at wavelengths that are smaller than the typical size of the specimen is quite complicated, and for periodic microstructures requires analyses of the Bloch wave type. Analysis of macroscopic bifurcations at wave lengths that are comparable with the size of the specimen are accomplished by treating the composite as a homogeneous medium. In this limit usage of the primary solution for Eq. (55) is made in conjunction with the procedure outlined in the previous section for determining loss of strong ellipticity. Geymonat et al. (1993) further showed that the domain characterizing the onset of macroscopic instabilities is an upper bound for the one characterizing the onset of instabilities at a smaller wavelength. In some cases, however, the macroscopic instabilities are the ones that occur first (*e.g.,* Nestorovic and Triantafyllidis (2004)).

In this work the *nonlinear-comparison* (NLC) variational method is used to estimate the effective properties of composites as defined in Eq. (55). The method is based on the derivation of a lower bound for the effective strain energy-density function with the aid of an appropriate estimate for the effective strain energy-density function of a non-linear comparison composite (deBotton and Shmuel (2010)). The NLC variational estimate for $\tilde{\Psi}(\bar{\mathbf{F}})$ states that

$$\hat{\Psi}(\bar{\mathbf{F}}) = \hat{\Psi}_0(\bar{\mathbf{F}}) + \sum_{r=1}^{n} c^{(r)} \inf_{\mathbf{F}} \left\{ \Psi^{(r)}(\mathbf{F}) - \Psi_0^{(r)}(\mathbf{F}) \right\}, \tag{57}$$

where $\hat{\Psi}_0$ is an estimate for the effective SEDF of a comparison hyperelastic composite whose phase behaviors are governed by the SEDFs $\Psi_0^{(r)}$, and their distributions are characterized by the functions $\varphi^{(r)}$ given in Eq. (51). The term appearing in the second part of Eq. (57) is denoted the *corrector term*, and I note that it depends only on the properties of the phases of the two composites.

Fiber composites are heterogeneous materials that are commonly made out of stiffer fibers that are embedded in a softer phase. Here I assume that the fibers are all aligned

in a particular direction $\hat{\mathbf{N}}$. If I further assume that their distribution in the transverse plane is random, the overall behavior of the composite is transversely isotropic. I examine two-phase transversely isotopic fiber composites whose phases strain energy-density functions are $\Psi^{(f)}$ and $\Psi^{(m)}$ for the fiber and the matrix phases, respectively. Both $\Psi^{(f)}$ and $\Psi^{(m)}$ are incompressible, isotropic and depend only on I_1. With the aid of the TIH model of deBotton et al. (2006) for a neo-Hookean fiber composite as the comparison composite, the NLC estimate for the effective strain energy density function is described by the optimization problem

$$\hat{\Psi}^{(TI)}\left(\bar{\lambda}_p^2, \bar{\lambda}_n^2, \bar{\gamma}_p^2, \bar{\gamma}_n^2\right) = \inf_{\omega}\left(c^{(m)}\Psi^{(m)}\left(\tilde{I}_1^{(m)}\left(\bar{\mathbf{F}}, \hat{\mathbf{N}}, \omega\right)\right) + c^{(f)}\Psi^{(f)}\left(\tilde{I}_1^{(f)}\left(\bar{\mathbf{F}}, \hat{\mathbf{N}}, \omega\right)\right)\right),$$
(58)

where

$$\tilde{I}_1^{(r)}(\bar{\mathbf{F}}, \hat{\mathbf{N}}, \omega) = \bar{\lambda}_n^2 + 2\bar{\lambda}_p^2 + \alpha^{(r)}\left(\bar{\gamma}_n^2 + \bar{\gamma}_p^2\right),$$
(59)

with

$$\alpha^{(f)} = \left(1 - c^{(m)}\omega\right)^2,$$
(60)

and

$$\alpha^{(m)} = \left(1 + c^{(f)}\omega\right)^2 + c^{(f)}\omega^2.$$
(61)

The details of the derivation of expression (58) from the NLC variational statement in Eq. (57) are given in deBotton and Shmuel (2010).

I denote by $\tilde{\omega}$ the value of ω that yields the solution for the Euler-Lagrange equation associated with Eq. (58). Clearly, $\tilde{\omega}$ is a function of the average deformation gradient, that is

$$\tilde{\omega} = \tilde{\omega}(\bar{\mathbf{F}}).$$
(62)

In some cases $\tilde{\omega}$ can be determined analytically, otherwise it must be calculated numerically. Since the partial derivative of $\hat{\Psi}^{(TI)}$ with respect to ω identically vanishes at $\tilde{\omega}$, the expression for the macroscopic stress can be evaluated analytically without the need for differentiating $\tilde{\omega}$ with respect to $\bar{\mathbf{F}}$. Specifically, the macroscopic nominal stress is

$$\hat{\mathbf{P}} = \sum_{r=m, f} c^{(r)} \frac{\partial \hat{\Psi}^{(TI)}}{\partial \tilde{I}_1^{(r)}} \frac{\partial \tilde{I}_1^{(r)}}{\partial \bar{\mathbf{F}}} + p\bar{\mathbf{F}}^{-T},$$
(63)

where

$$\frac{\partial \tilde{I}_1^{(r)}}{\partial \mathbf{F}}(\bar{\mathbf{F}}) = 2\left(\tilde{\alpha}^{(r)}\bar{\mathbf{F}} + \left(1 - \tilde{\alpha}^{(r)}\right)\left(1 - \frac{\lambda_p^2}{\lambda_n^2}\right)\bar{\mathbf{F}}\hat{\mathbf{N}} \otimes \hat{\mathbf{N}}\right),$$
(64)

and $\tilde{\alpha}^{(r)} = \alpha^{(r)}(\tilde{\omega})$.

The corresponding estimate for the tensor of the effective instantaneous elastic moduli can be written as

$$\hat{\boldsymbol{\mathcal{A}}} = \sum_{r=m, f}\left(\frac{\partial^2 \hat{\Psi}^{(TI)}}{\partial \tilde{I}_1^{(r)} \partial \tilde{I}_1^{(r)}}\mathbf{S}^{(r)}(\tilde{\omega}, \bar{\mathbf{F}})\mathbf{S}^{(r)}(\tilde{\omega}, \bar{\mathbf{F}}) + \frac{\partial \hat{\Psi}^{(TI)}}{\partial \tilde{I}_1^{(r)}}\boldsymbol{\mathcal{G}}^{(r)}(\tilde{\omega}, \bar{\mathbf{F}})\right),$$
(65)

where

$$\mathbf{S}^{(r)}(\tilde{\omega}, \bar{\mathbf{F}}) = \frac{\partial \tilde{I}_1^{(r)}}{\partial \bar{\mathbf{F}}}(\bar{\mathbf{F}}) + \frac{\partial \tilde{I}_1^{(r)}}{\partial \omega}(\tilde{\omega}) \frac{\partial \tilde{\omega}}{\partial \bar{\mathbf{F}}}, \tag{66}$$

and

$$\mathcal{G}^{(r)}(\tilde{\omega}, \bar{\mathbf{F}}) = \frac{\partial^2 \tilde{I}_1^{(r)}}{\partial \mathbf{F} \partial \mathbf{F}}(\bar{\mathbf{F}}) + 2 \frac{\partial \tilde{I}_1^{(r)}}{\partial \omega}(\tilde{\omega}) \frac{\partial^2 \tilde{\omega}}{\partial \mathbf{F} \partial \mathbf{F}} + \mathbf{Z}^{(r)} \frac{\partial \tilde{\omega}}{\partial \mathbf{F}} + \left(\mathbf{Z}^{(r)} \frac{\partial \tilde{\omega}}{\partial \mathbf{F}} \right)^T. \tag{67}$$

The first derivatives of $\tilde{I}_1^{(r)}(\bar{\mathbf{F}})$ with respect to $\bar{\mathbf{F}}$ are given in Eq. (64), and the first derivatives with respect to ω are

$$\frac{\partial \tilde{I}_1^{(m)}}{\partial \omega}(\tilde{\omega}) = 4c^{(f)} \left(1 + \tilde{\omega} + c^{(f)}\tilde{\omega} \right) \left(\bar{\gamma}_n^2 + \bar{\gamma}_p^2 \right), \tag{68}$$

and

$$\frac{\partial \tilde{I}_1^{(f)}}{\partial \omega}(\tilde{\omega}) = -4c^{(m)} \left(1 - c^{(m)}\tilde{\omega} \right) \left(\bar{\gamma}_n^2 + \bar{\gamma}_p^2 \right). \tag{69}$$

The second derivative of $\tilde{I}_1^{(r)}(\bar{\mathbf{F}})$ with respect to $\bar{\mathbf{F}}$ in Eq. (67) is

$$\frac{\partial^2 \tilde{I}_1^{(r)}}{\partial \bar{F}_{ij} \partial \bar{F}_{kl}}(\bar{\mathbf{F}}) = 2 \left(\tilde{\alpha}^{(r)} \delta_{ik} \delta_{jl} + \left(1 - \tilde{\alpha}^{(r)} \right) \left(\left(1 - \frac{\bar{\lambda}_p^2}{\bar{\lambda}_n^2} \right) \delta_{ik} + \frac{3\bar{\lambda}_p^2}{\lambda_n^4} \bar{F}_{ip} \bar{F}_{ks} \hat{L}_s \hat{L}_p \right) \hat{L}_l \hat{L}_j \right). \tag{70}$$

The terms $\mathbf{Z}^{(r)}$ in the Eq. (67) are

$$\mathbf{Z}^{(m)} = 4c^{(f)} \left(1 + \tilde{\omega} + c^{(f)}\tilde{\omega} \right) \left(\bar{\mathbf{F}} - \left(1 - \frac{\bar{\lambda}_p^2}{\bar{\lambda}_n^2} \right) \bar{\mathbf{F}} \hat{\mathbf{N}} \otimes \hat{\mathbf{N}} \right) \tag{71}$$

and

$$\mathbf{Z}^{(f)} = -4c^{(m)} \left(1 - c^{(m)}\tilde{\omega} \right) \left(\bar{\mathbf{F}} - \left(1 - \frac{\bar{\lambda}_p^2}{\bar{\lambda}_n^2} \right) \bar{\mathbf{F}} \hat{\mathbf{N}} \otimes \hat{\mathbf{N}} \right). \tag{72}$$

Note that the terms that do not include derivatives of $\tilde{\omega}(\bar{\mathbf{F}})$ with respect to $\bar{\mathbf{F}}$ can be evaluated apriori with substitution of $\tilde{\omega}$ after the solution of the optimization problem is obtained either analytically or numerically. Additionally,

$$\frac{\partial \tilde{\omega}}{\partial \bar{\mathbf{F}}} = \frac{\partial \tilde{\omega}}{\partial \lambda_n^2} \frac{\partial \bar{\lambda}_n^2}{\partial \bar{\mathbf{F}}} + \frac{\partial \tilde{\omega}}{\partial \lambda_p^2} \frac{\partial \bar{\lambda}_p^2}{\partial \bar{\mathbf{F}}} + \frac{\partial \tilde{\omega}}{\partial \gamma_n^2} \frac{\partial \bar{\gamma}_n^2}{\partial \bar{\mathbf{F}}} + \frac{\partial \tilde{\omega}}{\partial \gamma_p^2} \frac{\partial \bar{\gamma}_p^2}{\partial \bar{\mathbf{F}}}, \tag{73}$$

and

$$\begin{aligned} \frac{\partial^2 \tilde{\omega}}{\partial \bar{\mathbf{F}} \partial \bar{\mathbf{F}}} =& \frac{\partial^2 \tilde{\omega}}{\partial \lambda_n^2 \partial \bar{\mathbf{F}}} \frac{\partial \bar{\lambda}_n^2}{\partial \bar{\mathbf{F}}} + \frac{\partial \tilde{\omega}}{\partial \lambda_n^2} \frac{\partial^2 \bar{\lambda}_n^2}{\partial \bar{\mathbf{F}} \partial \bar{\mathbf{F}}} + \frac{\partial^2 \tilde{\omega}}{\partial \lambda_p^2 \partial \bar{\mathbf{F}}} \frac{\partial \bar{\lambda}_p^2}{\partial \bar{\mathbf{F}}} + \frac{\partial \tilde{\omega}}{\partial \lambda_p^2} \frac{\partial^2 \bar{\lambda}_p^2}{\partial \bar{\mathbf{F}} \partial \bar{\mathbf{F}}} \\ &+ \frac{\partial^2 \tilde{\omega}}{\partial \gamma_n^2 \partial \bar{\mathbf{F}}} \frac{\partial \bar{\gamma}_n^2}{\partial \bar{\mathbf{F}}} + \frac{\partial \tilde{\omega}}{\partial \gamma_n^2} \frac{\partial^2 \bar{\gamma}_n^2}{\partial \bar{\mathbf{F}} \partial \bar{\mathbf{F}}} + \frac{\partial^2 \tilde{\omega}}{\partial \gamma_p^2 \partial \bar{\mathbf{F}}} \frac{\partial \bar{\gamma}_p^2}{\partial \bar{\mathbf{F}}} + \frac{\partial \tilde{\omega}}{\partial \gamma_p^2} \frac{\partial^2 \bar{\gamma}_p^2}{\partial \bar{\mathbf{F}} \partial \bar{\mathbf{F}}}, \end{aligned} \tag{74}$$

where the explicit expressions for the derivatives of the invariants $\bar{\lambda}_n^2$, $\bar{\lambda}_p^2$, $\bar{\gamma}_n^2$, and $\bar{\gamma}_p^2$ are given in appendix A. Note that, in general, the derivatives of $\tilde{\omega}$ with respect to $\bar{\lambda}_n^2$,

$\bar{\lambda}_p^2$, $\bar{\gamma}_n^2$, and $\bar{\gamma}_p^2$ must be determined numerically unless an analytical solution for the optimization problem Eq. (58) can be derived. Finally, once the elastic moduli tensor (65) is determined, the strong ellipticity condition (49) can be checked.

When both phases of the composite are neo-Hookean, the optimization problem (58) yields

$$\widetilde{\omega}^{(H)} = \frac{\mu^{(f)} - \mu^{(m)}}{c^{(m)}\mu^{(f)} + (1 + c^{(f)})\mu^{(m)}}, \tag{75}$$

and the effective strain energy density function takes the form introduced by deBotton et al. (2006),

$$\hat{\Psi}^{TIH} = \bar{\mu}\left(\bar{\lambda}_n^2 + 2\bar{\lambda}_p^2 - 3\right) + \tilde{\mu}_p\bar{\gamma}_p^2 + \tilde{\mu}_n\bar{\gamma}_n^2, \tag{76}$$

where

$$\tilde{\mu}_p = \tilde{\mu}_n = \tilde{\mu} = \mu^{(m)}\frac{\left(1 + c^{(f)}\right)\mu^{(f)} + \left(1 - c^{(f)}\right)\mu^{(m)}}{\left(1 - c^{(f)}\right)\mu^{(f)} + \left(1 + c^{(f)}\right)\mu^{(m)}}, \tag{77}$$

is the expression for both the in-plane shear $\tilde{\mu}_p$ (deBotton (2005)), and the out-of-plane shear $\tilde{\mu}_n$ (deBotton and Hariton (2006)), and

$$\bar{\mu} = c^{(f)}\mu^{(f)} + c^{(m)}\mu^{(m)}, \tag{78}$$

is the isochoric shear modulus (*e.g.,* deBotton et al. (2006); He et al. (2006)). More recently Lopez-Pamies and Idiart (2010) extended the work of deBotton (2005) and demonstrated that Eq. (76) is an *exact* expression for the effective strain energy-density function of neo-Hookean sequentially-coated laminates. The tensor of elastic moduli associated with the strain energy-density function Eq. (76) together with Eq. (77) is

$$\mathcal{A}_{ijkl}^0 = \tilde{\mu}\delta_{ik}\delta_{jl} + (\bar{\mu} - \tilde{\mu})\left(\frac{3\bar{\lambda}_p^2}{\bar{\lambda}_n^4}\bar{F}_{ip}\bar{F}_{ks}\hat{L}_s\hat{L}_p + \left(1 - \frac{\bar{\lambda}_p^2}{\bar{\lambda}_n^2}\right)\delta_{ik}\right)\hat{L}_l\hat{L}_j. \tag{79}$$

Applying the strong ellipticity condition (49) to the case of compression along the fibers, a simple expression for the critical stretch ratio $\bar{\lambda}_c$ is obtained, namely

$$\bar{\lambda}_c = \left(1 - \frac{\tilde{\mu}}{\bar{\mu}}\right)^{1/3}. \tag{80}$$

Note that Agoras et al. (2009b) derived expressions (79) and (80) from the SEDF $\hat{\Psi}^{TIH}$ of deBotton et al. (2006). These investigators also derived the corresponding expressions that result from the LC variational method for composites with neo-Hookean phases. Under compression along the fibers both methods lead to expression (80), however for more general loading conditions the expression resulting from the LC method is more complicated than Eq. (79) and requires a solution of a quartic polynomial in parallel with Eq. (49). Agoras et al. (2009b) computed the onset of ellipticity loss under general loading conditions and found that in some cases the predictions of the LC variational

estimate are in agreement with the predictions resulting from the SEDF $\hat{\Psi}^{TIH}$ that corresponds to a *realizable* composite.

As was mentioned in the introduction, Agoras et al. (2009b) also determined estimates for the onset of instabilities in fiber composites with Gent phases by application of the LC variational estimate. For this class of composites the resulting expressions are more involved and require a solution of two nonlinear equations in conjunction with the strong ellipticity condition (49). Contrarily, even with Gent phases the optimization problem stemming from the NLC variational estimate of deBotton and Shmuel (2010) can be solved *analytically* to end up with an *explicit estimate* for the effective SEDF. In particular, the resulting Euler-Lagrange equations admit the form of a cubic polynomial in ω, from which explicit analytical expressions for $\tilde{\omega}$ and $\mathcal{A}^0_{ijkl}$ are obtained. For later reference note that

$$\tilde{\omega}^{(G)} = \tilde{\omega}^{(G)}\left(\bar{\mathbf{F}},\, c^{(f)},\, k,\, \mu^{(m)},\, r,\, J_m^{(m)}\right), \tag{81}$$

where

$$k = \mu^{(f)}/\mu^{(m)}, \tag{82}$$

is the ratio between the initial shear moduli of the fiber and the matrix, and

$$r = J_m^{(f)}/J_m^{(m)}, \tag{83}$$

is the ratio between the locking parameters.

I emphasize that the analytical procedure described so far can be used to estimate the macroscopic stable domains of hyperelastic fiber composites under general loading conditions. However, in the sequel I restrict the attention to plane-strain loading condition where the constrained direction of the deformation is normal to the direction of the fibers (*e.g.,* Qiu and Pence (1997)). This allows to examine the onset of instabilities due to compression along the fibers and to compare the analytical predictions with corresponding finite element simulations.

For convenience, I distinguish between the *principal* coordinate system of the right Cauchy-Green deformation tensor and the *material* coordinate system. Without loss of generality I define the material coordinate system such that in the reference state the direction of the fiber $\hat{\mathbf{N}}$ is aligned with the X_3-axis (see Fig. 4). Specifically, I set $F_{11} = 1$. Note, that with this choice the X_1-axis is common for both the principal and the material systems. Accordingly, in the principal coordinate system the plane-strain average deformation gradient is

$$\bar{\mathbf{F}}' = \begin{pmatrix} 1 & 0 & 0 \\ 0 & \lambda^{-1} & 0 \\ 0 & 0 & \lambda \end{pmatrix}. \tag{84}$$
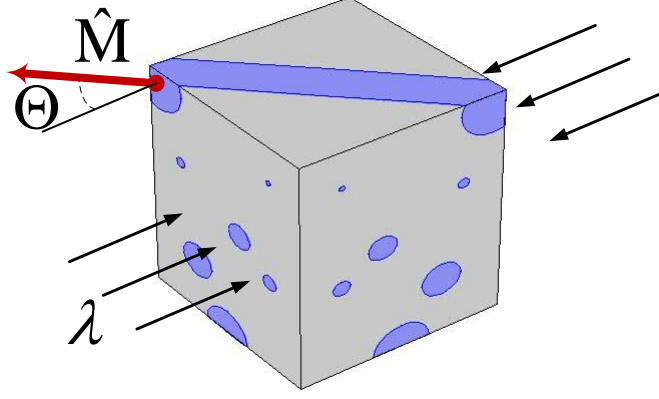
Fig. 5. Schematic representation of the loading direction angle Θ.

This is related to the average deformation gradient in the material coordinate system via the relation

$$\bar{\mathbf{F}} = \mathbf{R}^T \bar{\mathbf{F}}' \mathbf{R}, \tag{85}$$

where

$$\mathbf{R} = \begin{pmatrix} 1 & 0 & 0 \\ 0 & \cos\Theta & \sin\Theta \\ 0 & -\sin\Theta & \cos\Theta \end{pmatrix}, \tag{86}$$

is a rotation tensor. Here Θ is the referential angle between the direction of the principal stretch and the fiber direction (see Fig. 5).

In accordance with the plane-strain assumption, I also restrict the solution of Eq. (43) with a choice of infinitesimal planar deformation along the vectors $\hat{\mathbf{a}} = (0, \cos\phi, \sin\phi)$ and $\hat{\mathbf{v}} = (0, \sin\phi, -\cos\phi)$. While this choice of deformation is consistent with the plane-strain assumption, on physical grounds a choice of non-planar infinitesimal deformation is admissible. For instance, the solution ensued from this choice coincides with the solution obtained by Agoras et al. (2009b) with the choice $\hat{\mathbf{a}} = (0, 1, 0)$ and $\hat{\mathbf{v}} = (\sin\phi, 0, -\cos\phi)$.

2.3 Finite Element Simulation

I construct 3-D finite element models of fiber composites to estimate their macroscopic behaviors and stability regimes. I also construct 2-D laminated models as basis for comparison since these models are frequently used for estimation of the onset of failures in fiber composites. Note that the analytical treatment considered in the previous section corresponded to fiber composites with transversely isotropic symmetry. Khisaeva and Ostoja-Starzewski (2006) and Moraleda et al. (2009) considered periodic FE models with a few tens of fibers in the unit cell in order to approximate the macroscopically
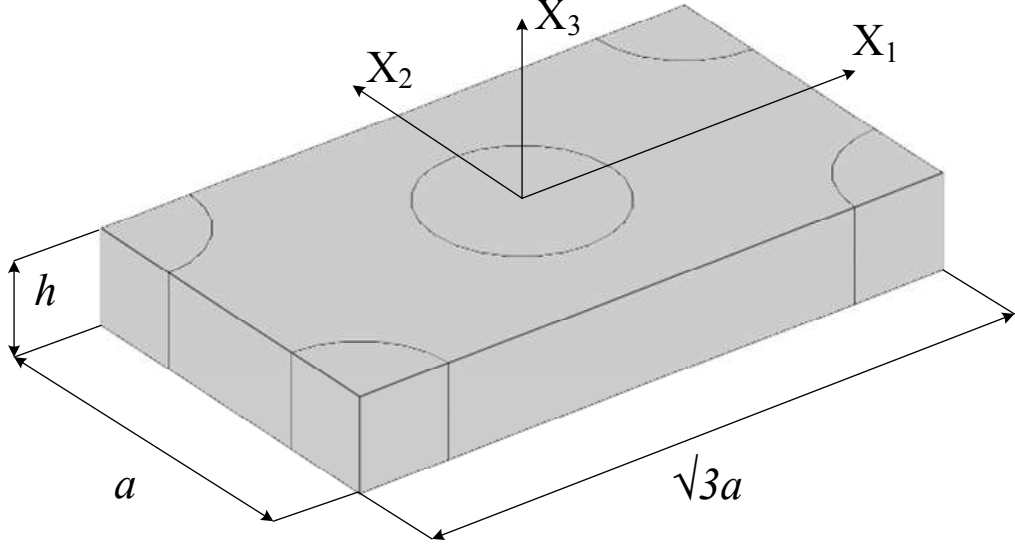
Fig. 6. The hexagonal unit cell modeled in the finite element code COMSOL.

isotropic response of TI composites in the transverse plane. In this work I consider the less computationally extensive model of periodic composites with hexagonal unit cells. These materials are orthotropic materials, however, in the limit of infinitesimal deformations they behave like transversely isotropic materials. This property makes them fair candidates for comparison with our analytical results (*e.g.,* Aravas et al. (1995); Michel et al. (2007); Shmuel and deBotton (2010)). This is particularly relevant in the context of instabilities due to compression along the fibers since the critical stretch ratios are usually larger than 0.95. I further note that in the loading modes that I consider in this work (compression and out-of-plane shear along the fibers) the precise distribution of the fibers in the transverse plane is not a crucial parameter.

A representative 3-D unit cell of a periodic composite with hexagonal arrangement of the fibers is shown in Fig. 6. The fibers are aligned along the X_3 axis and the ratio between the long to the short faces in the transverse plane is $\sqrt{3}$. The unit cell occupies the domain

$$-\frac{\sqrt{3}a}{2} \leq X_1 \leq \frac{\sqrt{3}a}{2}, \qquad -\frac{a}{2} \leq X_2 \leq \frac{a}{2}, \qquad -\frac{h}{2} \leq X_3 \leq \frac{h}{2}, \tag{87}$$

in the reference configuration. The response of the composite is obtained by applying periodic displacement boundary conditions and determining the average stress field in the unit cell from the resulting traction on the boundaries. The boundary conditions are extracted from the average deformation gradient tensor in Eq. (85) and imposed on the six faces of the unit cell as follows:

21

(1) The top $\left(X_3 = \dfrac{h}{2}\right)$ and bottom $\left(X_3 = -\dfrac{h}{2}\right)$ faces are related via

$$\begin{cases} u_1^B = u_1^T + \bar{F}_{13}h \\ u_2^B = u_2^T + \bar{F}_{23}h \\ u_3^B = u_3^T + \left(\bar{F}_{33} - 1\right)h \end{cases} , \tag{88}$$

(2) The front $\left(X_2 = \dfrac{a}{2}\right)$ and rear $\left(X_2 = -\dfrac{a}{2}\right)$ faces are related via

$$\begin{cases} u_1^F = u_1^{Re} + \bar{F}_{12}a \\ u_2^F = u_2^{Re} + \left(\bar{F}_{22} - 1\right)a \\ u_3^F = u_3^{Re} + \bar{F}_{32}a \end{cases} , \tag{89}$$

(3) The right $\left(X_1 = \dfrac{a\sqrt{3}}{2}\right)$ and left $\left(X_1 = -\dfrac{a\sqrt{3}}{2}\right)$ faces are related via

$$\begin{cases} u_1^L = u_1^R + \left(\bar{F}_{11} - 1\right)a\sqrt{3} \\ u_2^L = u_2^R + \bar{F}_{21}a\sqrt{3} \\ u_3^L = u_3^R + \bar{F}_{31}a\sqrt{3} \end{cases} . \tag{90}$$

The analysis of loss of ellipticity requires determination of the instantaneous tensor of elastic moduli. To this end I perform a set of additional incremental deformations from the deformed configuration. These incremental deformations lead to a macroscopic response of the model and result in an incremental variation of the average nominal stress. By making use of relation (38) in the principal coordinate system one obtains the expression

$$\delta\bar{\mathbf{P}}' = \bar{\boldsymbol{\mathcal{A}}}'\delta\bar{\mathbf{F}}', \tag{91}$$

from which the instantaneous macroscopic elastic moduli are estimated. When the deformation gradient is restricted to the planar form of Eq. (85), there is no deformation in the X_1 direction and the following three plane tests can be performed, namely

$$\bar{\mathbf{F}}'^{(1)} = \begin{pmatrix} 1 & 0 & 0 \\ 0 & \lambda^{-1} & \delta\bar{\gamma} \\ 0 & 0 & \lambda \end{pmatrix}, \quad \bar{\mathbf{F}}'^{(2)} = \begin{pmatrix} 1 & 0 & 0 \\ 0 & \lambda^{-1} & 0 \\ 0 & \delta\bar{\gamma} & \lambda \end{pmatrix}, \tag{92}$$

and the biaxial test

$$\bar{\mathbf{F}}'^{(3)} = \begin{pmatrix} 1 & 0 & 0 \\ 0 & (\lambda + \delta\lambda)^{-1} & 0 \\ 0 & 0 & \lambda + \delta\lambda \end{pmatrix}, \tag{93}$$

where $\delta\bar{\gamma}$ and $\delta\lambda$ are small increments. The deformation gradient and the nominal stress tensor increments in the principal coordinate system are

$$\delta\bar{\mathbf{F}}'^{(i)} = \bar{\mathbf{F}}'^{(i)} - \bar{\mathbf{F}}' \quad \text{and} \quad \delta\bar{\mathbf{P}}'^{(i)} = \bar{\mathbf{P}}'^{(i)} - \bar{\mathbf{P}}', \tag{94}$$

respectively.

Note that it is impossible to fully characterize the elastic properties of transversely isotropic materials on the basis of plane tests alone (*e.g.,* Ogden (2008)). This means that some of the terms of the tensor of macroscopic elastic moduli cannot be determined. Nonetheless, the condition for the loss of ellipticity can be extracted from appropriate *combinations* of the terms of the elastic tensor obtained from the planar tests. Specifically, the strong ellipticity condition (49), rewritten in the principal coordinate system of the left Cauchy-Green strain tensor, together with the incompressibility constraint (44) is

$$\begin{aligned}
\left((\bar{\mathcal{A}}'_{0\,3333} - \bar{\mathcal{A}}'_{0\,3322}) + (\bar{\mathcal{A}}'_{0\,2222} - \bar{\mathcal{A}}'_{0\,3322}) - 2\bar{\mathcal{A}}'_{0\,2332}\right) n_3^2 n_2^2 + \bar{\mathcal{A}}'_{0\,3232} n_3^4 + \\
\bar{\mathcal{A}}'_{0\,2323} n_2^4 + 2\left((\bar{\mathcal{A}}'_{0\,2232} - \bar{\mathcal{A}}'_{0\,3332}) n_3^3 n_2 + (\bar{\mathcal{A}}'_{0\,3323} - \bar{\mathcal{A}}'_{0\,2223}) n_2^3 n_3\right) > 0.
\end{aligned} \tag{95}$$

Though the individual terms $\bar{\mathcal{A}}'_{0\,3333}$, $\bar{\mathcal{A}}'_{0\,3322}$ and $\bar{\mathcal{A}}'_{0\,2222}$ cannot be determined, the combinations $\left(\bar{\mathcal{A}}'_{0\,3333} - \bar{\mathcal{A}}'_{0\,3322}\right)$ and $\left(\bar{\mathcal{A}}'_{0\,2222} - \bar{\mathcal{A}}'_{0\,3322}\right)$ can be extracted from the biaxial plane test (93) by making use of Eq. (91), Eq. (46) and the incremental incompressibility condition

$$\delta\mathbf{F} : \mathbf{F}^{-T} = 0. \tag{96}$$

Thus,

$$\delta\bar{F}'_{22} = -\delta\bar{F}'_{33}\frac{\bar{F}'_{22}}{\bar{F}'_{33}} = -\frac{\delta\bar{F}'_{33}}{\bar{F}'^2_{33}}. \tag{97}$$

Applying the biaxial test deformation $\bar{\mathbf{F}}'^{(3)}$, and using relation (46) together with Eq. (97), I end up with

$$\begin{aligned}
\bar{\mathcal{A}}'_{0\,3333} - \bar{\mathcal{A}}'_{0\,3322} &= \bar{F}'_{33}\bar{F}'_{33}\bar{\mathcal{A}}'_{3333} - \bar{F}'_{33}\bar{F}'_{22}\bar{\mathcal{A}}'_{3322} = \\
&= \bar{F}'_{33}\bar{F}'_{33}\left(\bar{\mathcal{A}}'_{3333} - \bar{\mathcal{A}}'_{3322}\frac{\bar{F}'_{22}}{\bar{F}'_{33}}\right) = \bar{F}'_{33}\bar{F}'_{33}\frac{\delta\bar{P}'^{(3)}_{33}}{\delta\bar{F}'^{(3)}_{33}},
\end{aligned} \tag{98}$$

and

$$\begin{aligned}
\bar{\mathcal{A}}'_{0\,2222} - \bar{\mathcal{A}}'_{0\,3322} &= \bar{F}'_{22}\bar{F}'_{22}\bar{\mathcal{A}}'_{2222} - \bar{F}'_{33}\bar{F}'_{22}\bar{\mathcal{A}}'_{3322} = \\
&= \bar{F}'_{22}\bar{F}'_{22}\left(\bar{\mathcal{A}}'_{2222} - \bar{\mathcal{A}}'_{3322}\frac{\bar{F}'_{33}}{\bar{F}'_{22}}\right) = \bar{F}'_{22}\bar{F}'_{22}\frac{\delta\bar{P}'^{(3)}_{22}}{\delta\bar{F}'^{(3)}_{22}}.
\end{aligned} \tag{99}$$

The rest of the terms, namely, $\bar{\mathcal{A}}'_{0\,3323}$, $\bar{\mathcal{A}}'_{0\,2223}$, $\bar{\mathcal{A}}'_{0\,2232}$, $\bar{\mathcal{A}}'_{0\,3332}$, $\bar{\mathcal{A}}'_{0\,3232}$ and $\bar{\mathcal{A}}'_{0\,2323}$ are obtained directly from the shear tests (92) by using Eq. (91) and Eq. (46).

The simulations were carried out by application of the commercial FE code COMSOL. The deformation is defined in the principal coordinate system in terms of $\bar{\mathbf{F}}'$, and I make use of Eq. (85) to impose the boundary conditions (88)-(90) on the unit cell in the material coordinate system where the FE simulation is executed. Next, the resulting output, in terms of the mean nominal stress tensor, is transformed back to the principal coordinate system via the relation

$$\bar{\mathbf{P}}' = \mathbf{R}\bar{\mathbf{P}}\mathbf{R}^T. \tag{100}$$

An identical procedure was used to simulate the 2-D models for the laminated composites.

Compressible SEDFs were defined directly in COMSOL code. The neo-Hookean strain energy-density functions of the phases are

$$\Psi_H^{(r)} = \frac{\mu^{(r)}}{2}\left(J_1 - 3\right) + \kappa^{(r)}\left(J - 1\right)^2, \tag{101}$$

where $J_1 = J^{-2/3}I_1$ and κ is a bulk modulus. The Gent strain energy-density functions are

$$\Psi_G^{(r)} = -\frac{\mu^{(r)}}{2}J_m^{(r)}\ln\left(1 - \frac{I_1 - 3}{J_m^{(r)}}\right) - \mu^{(r)}\ln J^{(r)} + \left(\frac{\kappa^{(r)} - 2\mu^{(r)}/3}{2} - \frac{\mu^{(r)}}{J_m^{(r)}}\right)\left(J^{(r)} - 1\right)^2. \tag{102}$$

Incompressibility was approximated by choosing bulk modulus $\kappa^{(r)}$ in each phase that is two orders of magnitude larger than the corresponding shear modulus $\mu^{(r)}$. A component of the average nominal stress on a given face of the unit cell is calculated by summing the corresponding components of the internal forces acting on the nodes of that face and dividing the resultant force by the area of the face in the undeformed configuration.

2.4 Applications

I make use of the results of the previous sections to determine numerical and analytical estimates for the loss of stability of fiber composites with neo-Hookean and Gent phases. First, I examine the case when both phases are neo-Hookean. When the composite is compressed along the fibers (*i.e.*, $\Theta = 0$ in Eq. (86)) the analytical expression for the critical stretch ratio is given in Eq. (80). The corresponding predictions obtained for composites with two different contrasts between the shear moduli of the phases are shown in Fig. 7 as functions of the fiber volume fraction. The solid curves correspond to $k = 100$ and 10.
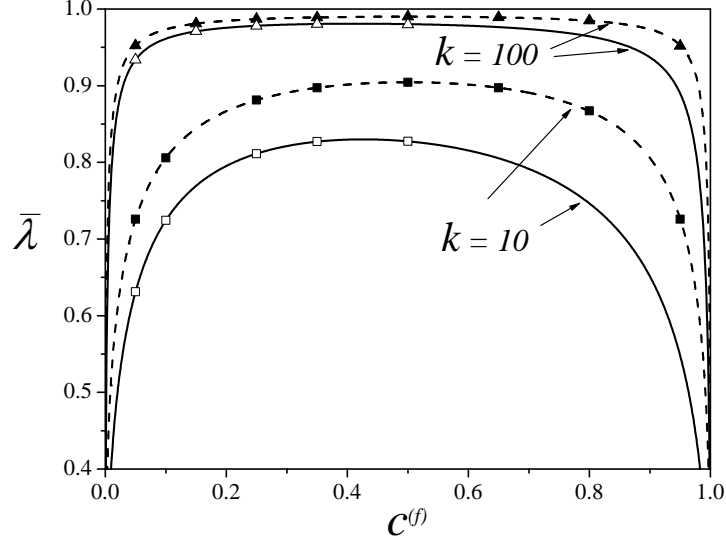
Fig. 7. The dependence of the critical stretch ratio on the fiber volume fraction. The solid curves correspond to fiber composites and the dashed curves to laminated composites. The results of the numerical simulations are marked by triangles for $k = 100$ and squares for $k = 10$.

The corresponding expression for laminated composites that was obtained by Triantafyllidis and Maker (1985) is

$$\bar{\lambda}_c = \left(1 - \frac{\hat{\mu}}{\bar{\mu}}\right)^{1/4}, \tag{103}$$

where

$$\hat{\mu} = \left(\frac{c^{(m)}}{\mu^{(m)}} + \frac{c^{(f)}}{\mu^{(f)}}\right)^{-1}, \tag{104}$$

and in this case $\mu^{(f)}$ and $\mu^{(m)}$ are shear moduli of the stiffer and the softer layers, respectively. For comparison, the predictions of this solution are presented in Fig. 7 by the dashed curves for $k = 100$ and 10. The corresponding results of the numerical simulations are marked by triangles for $k = 100$ and squares for $k = 10$. In all cases the numerical results are in excellent agreement with the analytical ones for both the laminated and the fiber composites.

Note that under these loading conditions $\phi = \pi/2$ (*i.e.*, $\hat{\mathbf{m}} = \hat{\mathbf{L}}$), meaning that at the onset of the instability the weak surface is perpendicular to the fibers and the deformation occurs along this surface. As was mentioned in Agoras et al. (2009b), in agreement with experimental findings this instability is associated with vanishing shear response in the plane transverse to the fibers. This observation is also in agreement with the earlier findings of Qiu and Pence (1997) and Merodio and Ogden (2002).

In comparison with composites with intermediate volume fraction of fibers, the onset of ellipticity loss occurs much later in composites with low and high fiber volume fractions. As expected, the composites become more sensitive to compression as the ratio
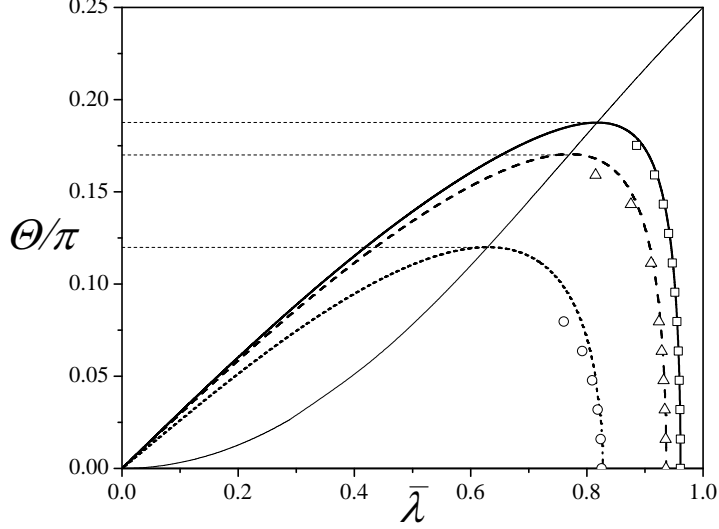
Fig. 8. The dependence of the critical stretch ratio on the loading direction. The solid, dashed and short-dash curves correspond to composites with fiber to matrix shear moduli ratio $k = 50$, 30 and 10, respectively. The simulation results are marked by squares, triangles and circles for $k = 50$, 30 and 10, respectively. The thin continuous curve shows the maximal loading angle Θ_m at which instability may occur. For all curves $c^{(f)} = 0.5$.

between the shear moduli increases. A comparison between the results for the laminated and the fiber composites reveals that the stable domain for the fiber composites is larger than the one for the laminated composite, though the trends of the curves are similar. In contrast with the results for the laminated composites, the results for the fiber composite are not symmetric with respect to $c^{(f)} = 0.5$. Thus, at low fiber volume fraction, the composite is more sensitive to compression than at high fiber volume fraction.

A few representative results for the critical stretch ratio under non-aligned compression are shown in Fig. 8. The corresponding expression for $\bar{\lambda}_c$ was determined by Agoras et al. (2009b) for the TIH model introduced in deBotton et al. (2006) in terms of the quartic polynomial equation

$$\bar{\lambda}_c^4 \cos^2 \Theta - \bar{\lambda}_c^2 \left(1 - \frac{\tilde{\mu}}{\bar{\mu}} \right)^{2/3} + \sin^2 \Theta = 0. \tag{105}$$

The solid, dashed and short-dashed curves correspond to fiber-to-matrix shear moduli ratios $k = 50$, 30 and 10, respectively. In all cases the volume fraction of the fiber is $c^{(f)} = 0.5$. The results of the corresponding numerical simulations are marked by squares, triangles and circles for $k = 50$, 30 and 10, respectively. The curves are symmetric with respect to the loading direction $\Theta = 0$, that is $\bar{\lambda}_c(\Theta) = \bar{\lambda}_c(-\Theta)$, and are also π-periodic, that is, $\bar{\lambda}_c(\Theta) = \bar{\lambda}_c(\Theta + \pi j)$, $j = 1, 2, 3...$. Additionally I note that $\bar{\lambda}_c(\Theta) = 1/\bar{\lambda}_c(\Theta + \pi/2)$.

Comparing the analytical solution to the numerical simulations, one can observe a

26
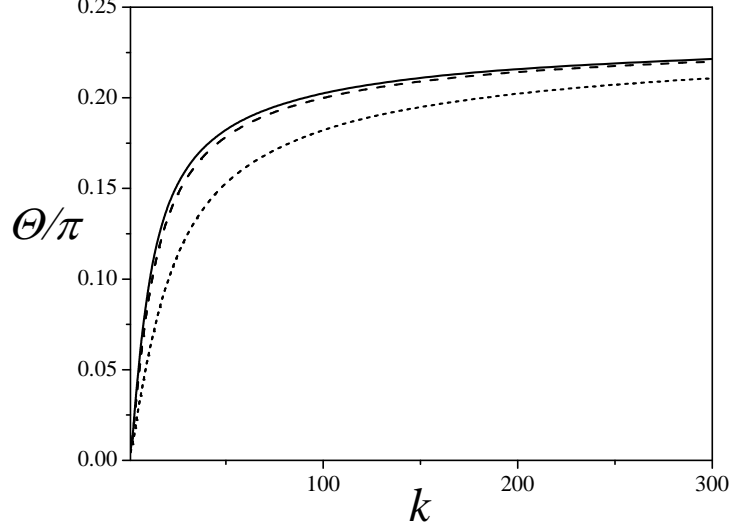
Fig. 9. The dependence of the maximal loading direction angle on the ratio between the shear moduli. The solid, dashed and short-dash curves correspond to volume fractions of the fiber $c^{(f)} = 0.1$, 0.25 and 0.5, respectively.

better agreement for higher shear moduli ratios k. However, for all cases the characteristic behavior is similar and the analytical solution is the more conservative estimation for the onset of failure. The reason for the difference is related to the fact that the analytical solution is obtained for incompressible composites while in the FE simulations the phases are slightly compressible. I emphasize that a decrease in the compressibility of the phases, in terms of an increase in the bulk to shear moduli ratio, resulted in an earlier onset of ellipticity loss and hence to a better agreement between the two estimates. This influence of incompressibility on the onset of failure is in agreement with the observation of Triantafyllidis et al. (2006). Additionally, I recall that the microstructure used in the numerical simulation, while providing a fair estimate for composites with randomly distributed fibers, is not an actual TI material.

In consistent with expectations, the value of $\bar{\lambda}_c$ approaches unity asymptotically as $k \to \infty$. Note that as the angle between the loading and the fiber directions increases there exist an angle (Θ_m) beyond which no macroscopic instability occurs. The critical stretch ratio corresponding to this angle is

$$\lambda_m = \frac{1}{\sqrt{2}\cos\Theta_m} \left(1 - \frac{\tilde{\mu}}{\bar{\mu}}\right)^{1/3}, \tag{106}$$

and it is represented in Fig. 8 by the thin continuous curve. Obviously, Θ_m depends on the fiber volume fraction and shear moduli ratio, and from Eq. (105) it is easy to see that

$$\Theta_m = \frac{1}{2}\arcsin\left(1 - \frac{\tilde{\mu}}{\bar{\mu}}\right)^{2/3}. \tag{107}$$
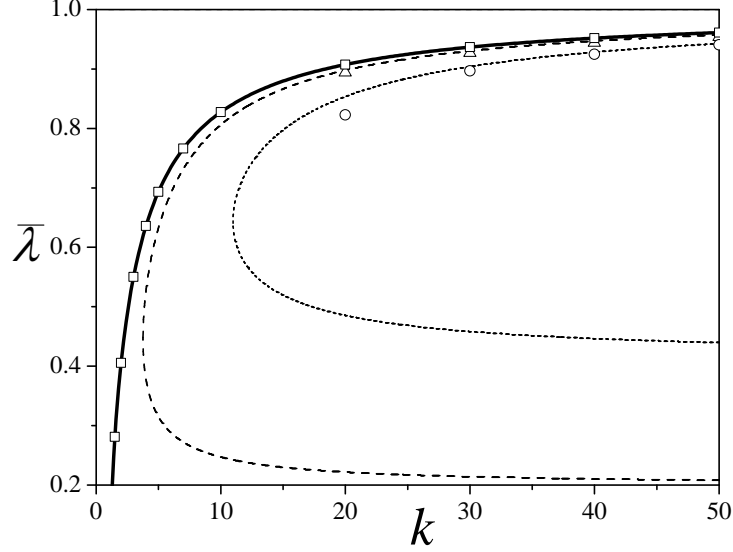
Fig. 10. The critical stretch ratio as a function of the contrast between the phases shear moduli for different loading directions. The continuous, dash and short-dashed curves correspond to $\Theta = 0$, $\pi/16$ and $\pi/8$, respectively. The results of the numerical simulation are marked by squares, triangles and circles for $\Theta = 0$, $\pi/16$ and $\pi/8$, respectively.

The dependence of the maximal angle Θ_m on the ratio between the shear moduli is shown in Fig. 9 for fiber volume fractions $c^{(f)} = 0.5$, 0.25 and 0.1 by solid, dashed, and short-dashed curves, respectively. The domain above the curve is the one for which no instability was detected, while in the region beneath the curve critical stretch ratios corresponding to ellipticity loss were found. Obviously, when the shear moduli contrast k becomes large the load direction Θ_m tends to $\pi/4$, corresponding to a switch of the load along the fibers from compression to tension. Combining Eq. (106) and Eq. (107) I end up with the expression

$$\Theta_m = \arctan \lambda_m^2. \tag{108}$$

The physical reasoning for this value becomes clear when the rotation of the fibers under non-aligned load is followed (*e.g.,* deBotton and Shmuel (2009)). Thus, in the deformed configuration the angle between the fiber and the loading directions is

$$\theta = \arctan\left(\lambda^{-2} \tan \Theta\right). \tag{109}$$

Eq. (108) and Eq. (109) lead to $\theta_m = \pi/4$. At this angle the loading on the fibers switches from compression to tension. Consequently, beyond this point no instability is detected. Thus, one can find that the maximal loading angle Θ_m corresponds to the state at which in the *current configuration* $\theta(\bar{\lambda}_c) = \pi/4$.

The dependence of the critical stretch on the contrast between the fiber to the matrix shear moduli is presented in Fig. 10 for different loading directions. The solid, dashed

and short-dashed curves correspond to the analytical solution for $\Theta = 0$, $\pi/16$ and $\pi/8$, respectively. The numerical simulation results are presented by squares, triangles and circles for $\Theta = 0$, $\pi/16$ and $\pi/8$, respectively.

The numerical simulation results are in good agreement with the analytical solution for low values of the loading angles. However, for relatively high values of this angle the deformation needed for the onset of ellipticity loss increases and hence the effect of the phases compressibility becomes significant. This, in turn, results in an increase in the difference between the analytical and the numerical predictions. This is on top of the difference stemming from the different microstructures associated with the two estimations.

Next, I examine the responses of composites whose phases behaviors are described by the Gent model Eq. (30). As was mentioned before, the variational estimate applied to this model results in a close-form solution of Eq. (62) in terms of a cubic polynomial. With this solution, the tensor of elastic moduli $\hat{\boldsymbol{\mathcal{A}}}$ given by Eq. (65) is evaluated at each step of the loading path which is described by the loading parameters λ and Θ. When the left-hand side of Eq. (49) becomes non-positive, instability may occur.

Remarkably, I find that for a wide range of materials and loading parameters (λ, Θ, k, $\mu^{(m)}$, $c^{(f)}$, r, $J_m^{(m)}$) the value of $\tilde{\omega}^{(G)}$, the solution of the optimization problem (58), is very close to $\tilde{\omega}^{(H)}$ which is the corresponding solution for the neo-Hookean composite given in Eq. (75). Upon substitution of this expression in Eq. (58) I end up with the following upper estimate (UE) for $\hat{\Psi}^{(TI)}$, namely,

$$\hat{\Psi}^{(UE)} = -\frac{1}{2} \sum_{r=m,f} c^{(r)} \mu^{(r)} J_m^{(r)} \ln \left(1 - \frac{\tilde{I}_1^{(r)}(\tilde{\omega}^{(H)}) - 3}{J_m^{(r)}} \right). \tag{110}$$

Moreover, one finds that for a large range of materials and loading parameters the derivatives of $\tilde{\omega}^{(G)}$ with respect to $\bar{\mathbf{F}}$ are negligible and hence not only the stresses can be analytically derived from Eq. (110), but also the tensor of elastic moduli can be easily derived. Thus, I have that

$$\hat{\boldsymbol{\mathcal{A}}}^{(UE)} = \sum_{r=m,f} \left(\frac{\partial^2 \hat{\Psi}^{(UE)}}{\partial \tilde{I}_1^{(r)} \partial \tilde{I}_1^{(r)}} \frac{\partial \tilde{I}_1^{(r)}}{\partial \bar{\mathbf{F}}}(\bar{\mathbf{F}}) \frac{\partial \tilde{I}_1^{(r)}}{\partial \bar{\mathbf{F}}}(\bar{\mathbf{F}}) + \frac{\partial \hat{\Psi}^{(UE)}}{\partial \tilde{I}_1^{(r)}} \frac{\partial^2 \tilde{I}_1^{(r)}}{\partial \bar{\mathbf{F}} \partial \bar{\mathbf{F}}}(\bar{\mathbf{F}}) \right). \tag{111}$$

Application of the strong ellipticity condition (49) and Eq. (46) with Eq. (111) results in closed-form estimates for the onset of macroscopic instabilities in Gent composites. In particular, when the fiber and the matrix lock-up stretches are identical (*i.e.*, $r = 1$), for the case of compression along the fibers the critical stretch ratio can be estimated

from the solution of the polynomial equation

$$\left(\left(\bar{\lambda}_c^3 - 1\right)\left(c^{(f)}\mu^{(f)}\alpha^{(m)} + c^{(m)}\mu^{(m)}\alpha^{(f)}\right) + \bar{\mu}\alpha^{(f)}\alpha^{(m)}\right)\left(1 - 2\bar{\lambda}_c + \bar{\lambda}_c^2\right) +$$
$$\left(\bar{\mu}(\bar{\lambda}_c^3 - 1) + \tilde{\mu}\right)\left(\bar{\lambda}_c^4 + 2\bar{\lambda}_c - \bar{\lambda}_c^2(J_m + 3)\right) = 0. \tag{112}$$

Note that as $J_m \to \infty$ this equation is reduced to the corresponding expression for the neo-Hookean composite as given in Eq. (80).

To estimate the applicability range of Eq. (111), the appropriate domain in the seven dimensional space of λ, Θ, k, $\mu^{(m)}$, $c^{(f)}$, r, $J_m^{(m)}$ should be identified. In this domain, the derivatives of $\tilde{\omega}^{(G)}$ with respect to $\bar{\mathbf{F}}$ should be negligible and $\tilde{\omega}^{(G)}$ can be approximated by $\tilde{\omega}^{(H)}$. In a way of an example, I examine the dependence of $\tilde{\omega}^{(G)}$ and $\dfrac{\partial \tilde{\omega}^{(G)}}{\partial \lambda}$ on λ. This is demonstrated in Fig. 11 for composites with fiber volume fraction $c^{(f)} = 0.5$, shear moduli ratio $k = 100$, $\mu^{(m)} = 10^6$ Pa, $r = 1$ and loading direction $\Theta = 0$. The continuous curves correspond to $\tilde{\omega}(\lambda)$ for $J_m = 0.1$, 1, 10, 100 and the dashed curves to the corresponding derivatives. The thin short-dash line corresponds to $\tilde{\omega}^{(H)}$ (which is independent of λ). One can observe two regions of the functions $\tilde{\omega}^{(G)}$ and $\dfrac{\partial \tilde{\omega}^{(G)}}{\partial \lambda}$, a "fast" region and a "slow" one. The value of λ_s that separates these two regions is given by the solution of the equation

$$\tilde{\omega}^{(G)}(\lambda_s) - \frac{\partial \tilde{\omega}^{(G)}}{\partial \lambda}(\lambda_s) = 0. \tag{113}$$

In Fig. 11, the curve crossings that represent the solution of Eq. (113) are marked by squares. One can observe that as long as $\lambda > \lambda_s$, that is in the "slow" region of the two functions, $\tilde{\omega}^{(G)}$ is almost identical to $\tilde{\omega}^{(H)}$. In the scale of this plot the critical stretch ratios for the four composites examined are very close and hence are marked by a single triangle mark. Since $\bar{\lambda}_c > \lambda_s$, in these composites the ellipticity loss occurs before the λ_s is achieved. Even in the case when $\bar{\lambda}_c < \lambda_s$ the upper estimate is still usable, but the difference in the predicted solution becomes large.

The results obtained by application of the upper estimate (112) for the critical stretch ratio are shown in Fig. 12 for the case of aligned compression ($\Theta = 0$). The solid curve corresponds to shear moduli ratio $k = 100$, and the dashed curve to $k = 50$. I emphasize that for the results shown in Fig. 12, the curves determined via the full solution of the variational estimate (that is with $\tilde{\omega}^{(G)}$ and its derivatives) lay on top of those determined via the upper estimate of Eq. (112). The dotted curve describes the solution of the lock-up equation due to loading in the form of Eq. (84)

$$\lambda_{lock} = \frac{1}{2}\left(\sqrt{J_m + 4} - \sqrt{J_m}\right). \tag{114}$$

The thin dashed lines are the corresponding estimates for the neo-Hookean composites. The results of the numerical simulations are also shown in Fig. 12. The square and
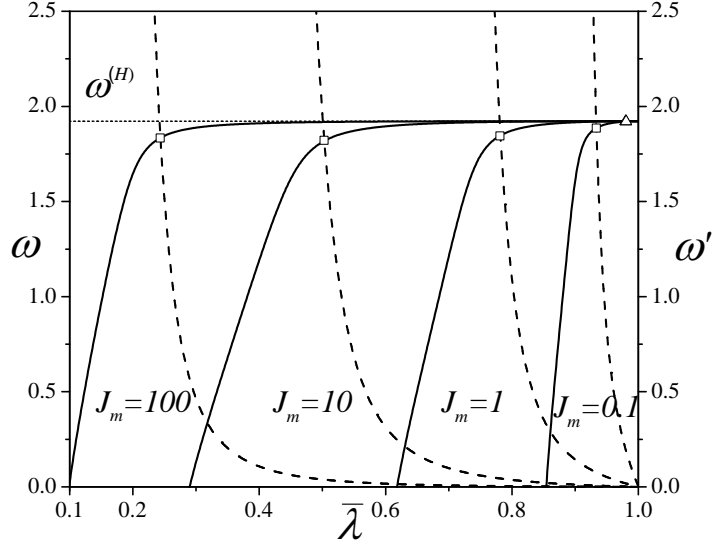
Fig. 11. The dependence of $\tilde{\omega}^{(G)}$ and $(\tilde{\omega}^{(G)})'$ on the stretch ratio λ for the Gent composite with $\Theta = 0$, $c^{(f)} = 0.5$, $k = 100$ and $r = 1$. The continuous curves correspond to $\tilde{\omega}^{(G)}(\lambda)$ for $J_m = 0.1$, 1, 10, 100 from right to left, while the dashed curves to $(\tilde{\omega}^{(G)})'(\lambda)$. The thin short-dash line corresponds to $\tilde{\omega}^{(H)}$ for the neo-Hookean composite. The curve crossings are marked by squares. The triangle indicates the critical stretch ratio for these composites.

circle marks correspond to simulations with $k = 100$ and 50, respectively. The numerical results are in good agreement with the analytical ones even in the region where the locking effect becomes significant. In a manner similar to one mentioned in connection with the neo-Hookean composites, the differences between the analytical and the numerical results are due to the effect of compressibility in the simulations and the different microstructures.

Note that in the region where the locking effect becomes significant, both phases markedly stiffen and hence the contrast between their stiffnesses decreases. Consequently, for small enough locking parameter of the Gent phases no instabilities are detected. Specifically, as can be deduced for the two families of Gent composites shown in Fig. 12, composites with $k = 100$ and $J_m < 0.018$ are stable, as well as composites with $k = 50$ and $J_m < 0.067$. I denote the minimal value of the locking parameter beneath which the composite is stable $J_m^{(c)}$. This value depends on the phase properties but particularly on k. The critical stretch ratios corresponding to $J_m^{(c)}$ are represented in Fig. 12 by a thin continuous curve.

In case when the matrix is characterized by a locking parameter smaller than that of the fiber phase (*e.g.,* $r < 1$), the matrix stiffens faster than the fiber and the contrast between the phases decreases with the deformation. In this case the composite becomes more stable in a manner similar to the case $tr = 1$. The situation changes when the fiber phase stiffens faster than the matrix phase (*e.g.,* $r > 1$). In this case, the contrast

31
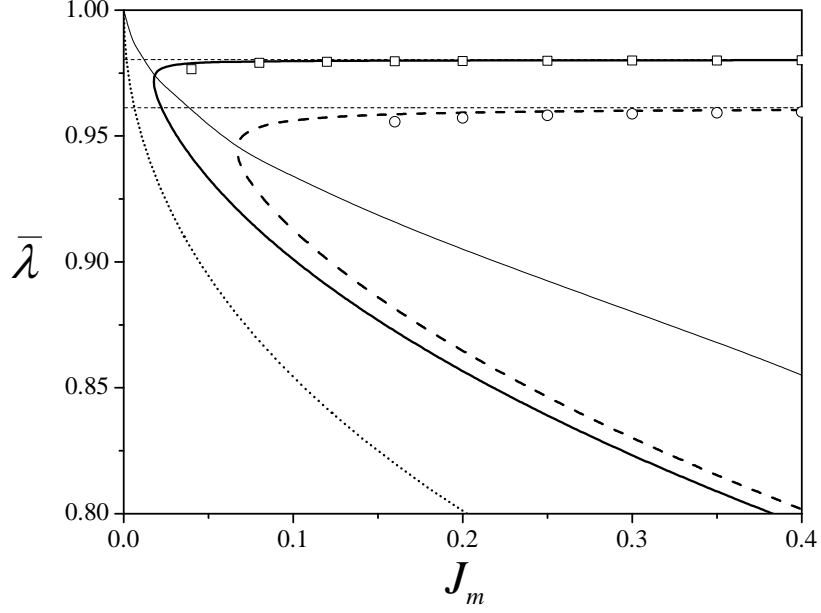
Fig. 12. The dependence of the critical stretch ratio $\bar{\lambda}_c$ on the locking parameter J_m. The solid line corresponds to shear moduli ratio $k = 100$, and the dashed curve to $k = 50$. The dotted curve represents the lock-up stretch ratio. The numerical simulation results are marked by squares and circles for $k = 100$ and 50, respectively.

between the phase responses increases with the deformation, and the composite becomes more sensitive to compression. This finding is consistent with corresponding findings of Agoras et al. (2009b) that were determined via the LC variational method.

Finally, the influence of the loading direction is demonstrated for composites with $c^{(f)} = 0.5$ and $k = 100$ in Fig. 13. Shown is the dependence of the critical stretch ratio $\bar{\lambda}_c$ on the locking parameter J_m. The solid curve corresponds to aligned compression ($\Theta = 0$), the dashed and short-dashed curves represent non-aligned compression with $\Theta = \pi/16$ and $\pi/8$ respectively. The results of the numerical simulations are marked by squares, triangles and circles for $\Theta = 0$, $\pi/16$ and $\pi/8$, respectively. The corresponding solutions for the neo-Hookean composites are marked by thin dashed curves. The dotted curve describes the lock-up stretch ratios according to Eq. (114).

The difference between the numerical simulations and the analytical predictions is due to the compressibility and microstructure differences. In a manner similar to the one observed for the neo-Hookean composites, an increase of the loading angle requires a decrease of the stretch ratio to achieve the onset of a failure. Additionally, for a given locking parameter J_m there exists a loading angle $\Theta^{(c)}$ beyond which the composite becomes stable. The curve corresponding to this loading angle, which terminates at $J_m^{(c)}$ when $\Theta = 0$, is presented in Fig. 13 by the thin continuous curve.

I conclude this section noting that in both cases of aligned loading (Fig. 12) and
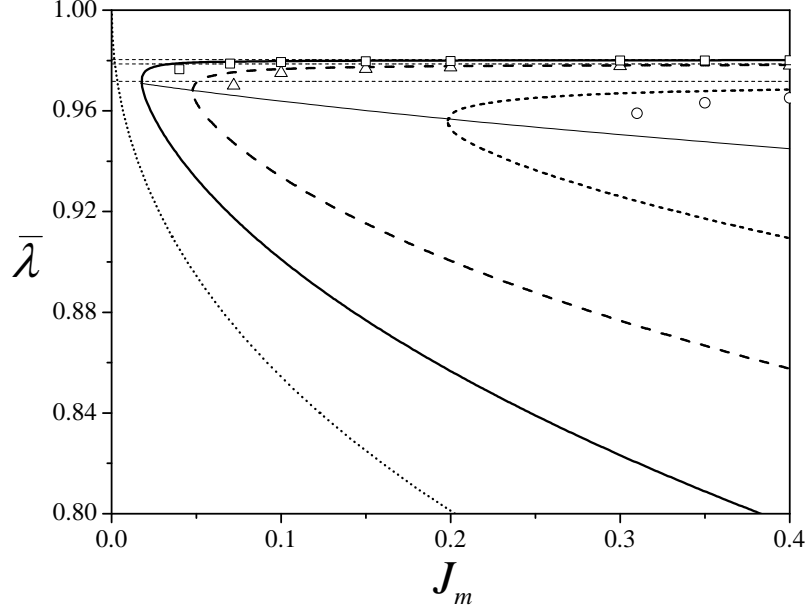
Fig. 13. The dependence of the critical stretch ratio $\bar{\lambda}_c$ on the locking parameter J_m for $k = 100$. The solid, dashed and short-dashed curves correspond to $\Theta = 0$, $\pi/16$ and $\pi/8$, respectively. The results of the numerical simulations are marked by squares, triangles and circles for $\Theta = 0$, $\pi/16$ and $\pi/8$, respectively. The corresponding solutions for the neo-Hookean composites are marked by dashed thin lines. The locking curve is the dotted one. The thin continuous curve represents the maximal loading angle for which instabilities were detected.

non-aligned loading (Fig. 13), the onset of failures in the Gent composites can be conservatively estimated by the corresponding predictions for the neo-Hookean composites even for relatively small values of J_m. The proximity between the estimates for the critical stretches is in agreement with corresponding results computed by Bertoldi and Boyce (2008) and Agoras et al. (2009b). Bertoldi and Boyce (2008) noted that for $J_m > 1$ the numerical estimates for both microscopic and macroscopic critical stretch ratios at the onset of ellipticity loss in porous composites with Gent and neo-Hookean matrices are almost identical when their microstructures are identical. Based on estimates computed for specific composites with neo-Hookean and Gent phases, Agoras et al. (2009b) infer that macroscopic instabilities may develop in non-linear incompressible fiber composites whenever $\bar{\lambda}_n$ reaches the critical value predicted by Eq. (80) that was derived from the TIH model of deBotton et al. (2006). Specifically, it was proposed that the estimates for the effective isochoric and out-of-plane shear moduli of the non-linear composite in the reference configuration will be substituted for $\bar{\mu}$ and $\tilde{\mu}$ in Eq. (80), respectively.

A fundamental reasoning for the proximity of the various estimates computed for composites with identical microstructures and different behaviors of the phases was given in deBotton and Shmuel (2010). These investigators noted that the structure of the variational estimate (57) hints at the fact that bifurcations exhibited by the compos-

ite should be related to corresponding bifurcations of the associated comparison composite. This is because the corrector term depends only on the properties of the phases, and hence bifurcations cannot be associated with this term. Accordingly, whenever a secondary solution that is associated with a lower energy state branches out from the primary solution, a corresponding secondary solution will branch out from the primary solution for the comparison composite as well. While the precise configurations at which the bifurcations occur in the composite and the comparison composite do not have to be identical, if the corrector terms are small the two states should be quite close. I further note that the proximity of the critical stretch ratios at the onset of instability in the two composites is not limited to the vicinity of the reference configuration (as concluded by Agoras et al. (2009b)). In fact, with an appropriate optimization over the properties of the comparison composite, estimates for instabilities that occur at large stretch ratios can be deduced from instability analysis of the comparison composite. Moreover, while estimate (58) that was used throughout this work was obtained by making use of a comparison composite with neo-Hookean phases, the general variational estimate Eq. (57) allows to make use of comparison composites with other types of phases. Usage of available estimates for composites with two-terms, such as Yeoh (1993) model (*e.g.,* Shmuel and deBotton (2010)) or anisotropic phases (*e.g.,* deBotton and Shmuel (2009); Lopez-Pamies and Idiart (2010)) will improve the resulting estimates for critical stretch ratios away from the reference configuration.

I finally note that the proximity of the critical loading states is anticipated for the critical stretch ratios since in Eq. (57) the macroscopic deformation gradient $\bar{\mathbf{F}}$ appears in the expressions for the energy-density functions of both the composite $\hat{\Psi}$ and the comparison composite $\hat{\Psi}_0$. The same cannot be inferred for the corresponding critical stresses at the onset of ellipticity loss in the two composites since the slopes of $\hat{\Psi}$ and $\hat{\Psi}_0$ may differ quite a bit. This observation explains why Agoras et al. (2009b) found that while the estimates they computed for the critical stretch ratios of the neo-Hookean and the Gent composites are in good agreement, the same cannot be said for the corresponding estimates computed for the critical stresses.

2.5 Conclusions

In this chapter I examined both analytically and numerically the instability phenomenon in hyperelastic fiber composites. I focused on predictions of the onset of failure due to loss of ellipticity of the governing equations describing the homogenized behavior of the composites. The analytical model involved a TI composite in which aligned stiffer fibers in a softer matrix are randomly distributed in the transverse plane. The

nonlinear-comparison variational method of deBotton and Shmuel (2010) was utilized to estimate the composites effective response. In particular, I examined composites with neo-Hookean and Gents phases. Additionally, a new upper estimate for Gent composites was introduced. In parallel, I developed a 3-D FE model and extended techniques for numerically determining the onset of ellipticity loss.

The analytical models resulted in closed-form estimates for the critical stretch ratio corresponding to the onset of failure. The critical stretch ratio depends mainly on the volume fraction of the fiber and the contrast between the moduli of the fiber and the matrix. The higher the contrast, the less compressive strain is needed for the appearance of instabilities. The influence of the fiber volume fraction is weak for the common range of fiber volume fraction $0.2 < c^{(f)} < 0.5$ but becomes significant in the limits of low and high volume fractions.

In accordance with the analytical findings, the numerical simulations yielded different results for laminate and fiber composites. It was shown that the layered composites are more sensitive to compression than the fiber composites. Additionally, in contrast to the layered materials, the fiber composites are more stable in the range of high fiber volume fractions than at low ones. For non-aligned compression it is found that above a certain loading angle no instability occurs. I demonstrate that this loading angle corresponds to the state when the angle between the fiber and the load in the *deformed configuration* is $\pi/4$. At this angle the loading on the fibers switches from compression to tension.

In the limit of small locking parameter the Gent composites become stable. This is due to the stiffening of both the fiber and the matrix phases resulting in a decrease of the contrast between the instantaneous moduli. Consequently, the critical stretch ratio decreases towards the stretch ratio at which the material locks up and practically no instability occurs. At larger values of the locking parameter it is found that the onset of failure of the Gent composites can be quite satisfactory predicted by the corresponding estimate for neo-Hookean composites. This finding, which is in agreement with corresponding results of Bertoldi and Boyce (2008) and Agoras et al. (2009b), is explained in the light of the nonlinear comparison variational estimate of deBotton and Shmuel (2010).

Chapter 3

Macroscopic Instabilities in Anisotropic Soft Dielectrics

In this chapter I extend the work of Dorfmann and Ogden (2010) to the class of *anisotropic* electroactive materials undergoing large deformations. I introduce a *general criterion* for the onset of instability for plane problems. In a way of an example I examine the class of layered media with isotropic behavior of the layers. I chose this class for two reasons. The first is related to the fact that expressions for the coupled electromechanical behaviors of anisotropic EAPs are not available in the literature, and since layered materials can be manufactured the outcome will correspond to a feasible class of anisotropic materials. For this reason I also chose a widely accepted form for the phases behavior, one that can provide an approximation to more complicated behaviors in the limit of small to moderate deformations. The second reason stems from the fact that for this class of materials a rigorous *explicit* expression for the homogenized anisotropic energy-density function can be determined (deBotton and Tevet-Deree, 2006; Bertoldi and Gei, 2011). By making use of this expression for their overall energy-density function, I identify the stable domain of these materials under different loading conditions and demonstrate the significance of their overall symmetry.

3.1 Theory

In order to determine the onset of instabilities I seek a solution for Eq. (20) in the form

$$v_i = \tilde{v}_i f(\hat{\mathbf{a}} \cdot \mathbf{x}), \quad \dot{p} = \tilde{q} f'(\hat{\mathbf{a}} \cdot \mathbf{x}), \quad \dot{D}_i = \tilde{d}_i f'(\hat{\mathbf{a}} \cdot \mathbf{x}), \tag{115}$$

where f is a continuous and sufficiently differentiable function and $\hat{\mathbf{a}}$ is a unit vector.

Assume that the material undergoes *plane-strain* deformations and there is no out-of-plane component of the electric displacement field. By making use of the incompressibility constraint div $\mathbf{v} = 0$ together with Maxwell equation for $\dot{\mathbf{D}}$, it can be found that $\tilde{v}_i \hat{a}_i = 0$ and $\tilde{d}_i \hat{a}_i = 0$ and hence $\tilde{d}_i = \gamma \tilde{v}_i$, where γ is a real coefficient. Thus, upon substitution of Eq. (115) together with the relation $\tilde{d}_i = \gamma \tilde{v}_i$ in Eq. (20) and eliminating the pressure increment, I end up with a polynomial equation for $\xi \equiv a_2/a_1$, namely

$$\Gamma_6 \xi^6 + \Gamma_5 \xi^5 + \Gamma_4 \xi^4 + \Gamma_3 \xi^3 + \Gamma_2 \xi^2 + \Gamma_1 \xi + \Gamma_0 = 0. \tag{116}$$

The coefficients Γ_i are given in terms of the electroelastic moduli

$$\Gamma_0 = \mathcal{K}_{122}^2 - \mathcal{A}_{2121}\mathcal{D}_{22},$$

$$\Gamma_1 = 2\left(\mathcal{A}_{2121}\mathcal{D}_{12} + \left(\mathcal{A}_{1121} - \mathcal{A}_{2122}\right)\mathcal{D}_{22} - \mathcal{K}_{122}\left(\mathcal{K}_{112} + \mathcal{K}_{121} - \mathcal{K}_{222}\right)\right),$$

$$\Gamma_2 = -\mathcal{A}_{2121}\mathcal{D}_{11} - 4\left(\mathcal{A}_{1121} - \mathcal{A}_{2122}\right)\mathcal{D}_{12} - \left(\mathcal{A}_{1111} - 2\mathcal{A}_{1122} - 2\mathcal{A}_{1221} + \mathcal{A}_{2222}\right)\mathcal{D}_{22}$$
$$+ 2\mathcal{K}_{122}\left(\mathcal{K}_{111} - \mathcal{K}_{122} - \mathcal{K}_{221}\right) + \left(\mathcal{K}_{112} + \mathcal{K}_{121} - \mathcal{K}_{222}\right)^2,$$

$$\Gamma_3 = 2((\mathcal{A}_{1121} - \mathcal{A}_{2122})\mathcal{D}_{11} + (\mathcal{A}_{1111} - 2\mathcal{A}_{1122} - 2\mathcal{A}_{1221} + \mathcal{A}_{2222})\mathcal{D}_{12}$$
$$+ \left(\mathcal{A}_{1222} - \mathcal{A}_{1112}\right)\mathcal{D}_{22} + (\mathcal{K}_{121}\mathcal{K}_{122} - (\mathcal{K}_{111} - \mathcal{K}_{122} - \mathcal{K}_{221})(\mathcal{K}_{112} + \mathcal{K}_{121} - \mathcal{K}_{222}))),$$

$$\Gamma_4 = -\left(\mathcal{A}_{1111} - 2\mathcal{A}_{1122} - 2\mathcal{A}_{1221} + \mathcal{A}_{2222}\right)\mathcal{D}_{11} + 4\left(\mathcal{A}_{1112} - \mathcal{A}_{1222}\right)\mathcal{D}_{12}$$
$$- \mathcal{A}_{1212}\mathcal{D}_{22} + \left(\mathcal{K}_{122} + \mathcal{K}_{221} - \mathcal{K}_{111}\right)^2 - 2\mathcal{K}_{121}\left(\mathcal{K}_{112} + \mathcal{K}_{121} - \mathcal{K}_{222}\right),$$

$$\Gamma_5 = 2\left(\left(\mathcal{A}_{1222} - \mathcal{A}_{1112}\right)\mathcal{D}_{11} + \mathcal{A}_{1212}\mathcal{D}_{12} + \mathcal{K}_{121}(\mathcal{K}_{111} - \mathcal{K}_{122} - \mathcal{K}_{221})\right),$$

$$\Gamma_6 = \mathcal{K}_{121}^2 - \mathcal{A}_{1212}\mathcal{D}_{11}.$$

$$(117)$$

Whenever a real solution for Eq. (116) exists, instabilities may occur. The corresponding value of γ that relates the amplitudes of the incremental changes in the electric displacement and the displacement is

$$\gamma = \frac{\mathcal{K}_{121}\xi^3 + \left(\mathcal{K}_{111} - \mathcal{K}_{122} - \mathcal{K}_{221}\right)\xi^2 + \left(\mathcal{K}_{222} - \mathcal{K}_{112} - \mathcal{K}_{121}\right)\xi + \mathcal{K}_{122}}{\mathcal{D}_{22} + \left(\mathcal{D}_{11}\xi - 2\mathcal{D}_{12}\right)\xi}. \qquad (118)$$

I conclude this section noting that condition (116) is an extension to the class of anisotropic materials of the corresponding result derived by Dorfmann and Ogden (2010) for the class of isotropic materials. In the following section I apply this general criterion to a specific class of anisotropic materials for which analytical expressions for the electroelastic moduli can be determined. Yet, before I proceed to this task, I stress that condition (116) can be used in conjunction with numerical simulations of more general anisotropic materials for which analytical solutions cannot be determined. In these cases estimates for the electroelastic moduli can be determined with appropriate simulations of small variations in the boundary conditions.

3.2 Applications to Soft Dielectric Laminates.

In a way of an example I examine the class of layered composites with two isotropic and incompressible phases. As was mentioned in the introduction, from a practical viewpoint this is a feasible class of materials and from a theoretical viewpoint their overall behavior can be determined explicitly (deBotton et al. (2007); Tevet-Deree (2008)). The resulting closed form expressions for the electroelastic moduli can be conveniently utilized in the

stability analysis. Bertoldi and Gei (2011) considered this class of composites under specific loading conditions that are aligned with the layers. Here, I extend this analysis and examine the influence of more general loadings on the onset of instabilities. In this regard it is worth mentioning that enhancement of the mechanical response to electrical excitation crucially depends on the ability to furnish appropriate soft modes of deformation by controlling the angle between the layers and the electrical excitation field deBotton et al. (2007); Tevet-Deree (2008).

The volume fractions of the phases are $c^{(m)}$ and $c^{(f)} = 1 - c^{(m)}$. Geometrically, the layers are characterized by their thicknesses $h^{(m)} = c^{(m)}h$ and $h^{(f)} = c^{(f)}h$, where $h = h^{(m)} + h^{(f)}$. Here and thereafter I denote a field in phase r by $(\bullet)^{(r)}$, in particular $(\bullet)^{(f)}$ and $(\bullet)^{(m)}$ correspond to the stiffer and the softer phases, respectively. The direction normal to the layers plane in the undeformed configuration is the laminate direction $\hat{\mathbf{N}}$, and $\hat{\mathbf{M}}$ is a unit vector tangent to the interface (see Fig. 20). Specifically, in terms of the referential lamination angle Θ,

$$\hat{\mathbf{N}} = \sin\Theta\,\hat{\mathbf{e}}_1 + \cos\Theta\,\hat{\mathbf{e}}_2 \quad \text{and} \quad \hat{\mathbf{M}} = \cos\Theta\,\hat{\mathbf{e}}_1 - \sin\Theta\,\hat{\mathbf{e}}_2. \tag{119}$$

Assuming that all fields are homogeneous in each phase, I have that the mean deformation gradient, the nominal electric field and the electric displacement are

$$\bar{\mathbf{F}} = c^{(m)}\mathbf{F}^{(m)} + c^{(f)}\mathbf{F}^{(f)}, \quad \bar{\mathbf{E}}^0 = c^{(m)}\mathbf{E}^{0\,(m)} + c^{(f)}\mathbf{E}^{0\,(f)}, \quad \bar{\mathbf{D}}^0 = c^{(m)}\mathbf{D}^{0\,(m)} + c^{(f)}\mathbf{D}^{0\,(f)}. \tag{120}$$

Following deBotton (2005), by making use of the displacement continuity condition across the interface

$$\mathbf{F}^{(m)} = \bar{\mathbf{F}}\left(\mathbf{I} + c^{(f)}\alpha\hat{\mathbf{M}} \otimes \hat{\mathbf{N}}\right), \quad \mathbf{F}^{(f)} = \bar{\mathbf{F}}\left(\mathbf{I} - c^{(m)}\alpha\hat{\mathbf{M}} \otimes \hat{\mathbf{N}}\right), \tag{121}$$

where the scalar α is obtained from the traction continuity condition

$$\left(\mathbf{P}^{(m)} - \mathbf{P}^{(f)}\right) \cdot \hat{\mathbf{N}} = 0. \tag{122}$$

Similarly, since the interfaces are charge free, the continuity condition for the electric displacement is

$$\left(\mathbf{D}^{0\,(m)} - \mathbf{D}^{0\,(f)}\right) \cdot \hat{\mathbf{N}} = 0 \quad \text{or} \quad \mathbf{D}^{0\,(m)} - \mathbf{D}^{0\,(f)} = \beta\hat{\mathbf{M}}, \tag{123}$$

and, together with the last of Eq. (120), I conclude that

$$\mathbf{D}^{0\,(m)} = \bar{\mathbf{D}}^0 + c^{(f)}\beta\hat{\mathbf{M}} \quad \text{and} \quad \mathbf{D}^{0\,(f)} = \bar{\mathbf{D}}^0 - c^{(m)}\beta\hat{\mathbf{M}}, \tag{124}$$

where β is a scalar to be determined from the continuity condition for the nominal electric field

$$\left(\mathbf{E}^{0\,(m)} - \mathbf{E}^{0\,(f)}\right) \cdot \hat{\mathbf{M}} = 0. \tag{125}$$

The energy-density function of the isotropic phases can be expressed in terms of the invariants of the Cauchy-Green strain tensor $\mathbf{C} \equiv \mathbf{F}^T\mathbf{F}$ and the referential electric displacement $\mathbf{D}^0$ Dorfmann and Ogden (2005). A set of six invariants can be expressed in the form

$$I_1 = \mathrm{Tr}\mathbf{C}, \quad I_2 = \frac{1}{2}(I_1^2 - \mathrm{Tr}(\mathbf{CC})), \quad I_3 = \det\mathbf{C},$$
$$I_{4e} = \mathbf{D}^0 \cdot \mathbf{D}^0, \quad I_{5e} = \mathbf{D}^0 \cdot \mathbf{CD}^0, \quad I_{6e} = \mathbf{D}^0 \cdot \mathbf{C}^2\mathbf{D}^0. \tag{126}$$

Thus, the energy-density functions of the isotropic phases can be written as scalar functions of these six invariants in terms of the local fields $\mathbf{F}^{(r)}$ and $\mathbf{D}^{0\,(r)}$. In particular, for composites with neo-Hookean dielectric phases the energy-density functions are

$$\Phi^{(r)}(\mathbf{F}^{(r)}, \mathbf{D}^{0\,(r)}) = \frac{\mu^{(r)}}{2}\left(I_1^{(r)} - 3\right) + \frac{1}{2\epsilon^{(r)}}I_{5e}^{(r)}, \tag{127}$$

where $\mu^{(r)}$ are the shear moduli and $\epsilon^{(r)}$ are the dielectric constants of the two phases. In this work I restrict the attention to this class of phase behaviors for two reasons. The first stems from the fact that explicit expressions for the corresponding effective electroelastic moduli can be determined. The second is that, at moderate stretch levels where instabilities frequently onset, this energy-density function can be viewed as a first order estimate for more general energy-density functions (e.g., Shmuel and deBotton, 2010). Moreover, in the purely mechanical case it was recently found that the critical stretch ratios at which instabilities occur in composites with neo-Hookean phases can serve as good estimates for corresponding critical stretch ratios for composites with Gent phases (Bertoldi and Boyce, 2008; Agoras et al., 2009b; Rudykh and deBotton, 2012).

Upon substitution of Eq. (127), with the aid of Eqs. (22) for $\mathbf{P}^{(r)}$ and $\mathbf{E}^{0(r)}$, in Eqs. (122) and (125) it can be found that

$$\alpha = \frac{\mu^{(f)} - \mu^{(m)}}{c^{(m)}\mu^{(f)} + c^{(f)}\mu^{(m)}}\frac{\bar{\mathbf{F}}\hat{\mathbf{N}} \cdot \bar{\mathbf{F}}\hat{\mathbf{M}}}{\bar{\mathbf{F}}\hat{\mathbf{M}} \cdot \bar{\mathbf{F}}\hat{\mathbf{M}}}, \tag{128}$$

and

$$\beta = \frac{\mu^{(m)}\epsilon^{(m)} - \mu^{(f)}\epsilon^{(f)}}{(c^{(m)}\mu^{(f)} + c^{(f)}\mu^{(m)})\bar{\epsilon}}\frac{\bar{\mathbf{F}}\bar{\mathbf{D}}^0 \cdot \bar{\mathbf{F}}\hat{\mathbf{M}}}{\bar{\mathbf{F}}\hat{\mathbf{M}} \cdot \bar{\mathbf{F}}\hat{\mathbf{M}}} + \frac{\mu^{(f)} - \mu^{(m)}}{c^{(m)}\mu^{(f)} + c^{(f)}\mu^{(m)}}\bar{\mathbf{D}}^0 \cdot \hat{\mathbf{M}}, \tag{129}$$

where $\bar{\epsilon} = c^{(m)}\epsilon^{(m)} + c^{(f)}\epsilon^{(f)}$.

Once the solution for the boundary value problem is given in terms of the local fields in both phases, the expression for the macroscopic energy-density function of the composite can be expressed as the weighted sum of the energy-density functions of the two phases, namely

$$\tilde{\Phi}(\bar{\mathbf{F}}, \bar{\mathbf{D}}^0) = \sum_{r=m,f} c^{(r)}\Phi^{(r)}(\bar{\mathbf{F}}, \bar{\mathbf{D}}^0). \tag{130}$$
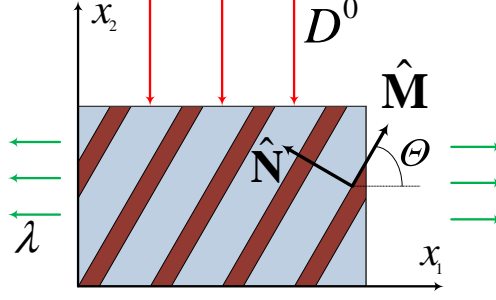
Fig. 14. Electroactive layered composite subjected to electric excitation

The expressions for the average nominal stress and electric field are

$$\bar{\mathbf{P}} = \frac{1}{2} \sum_{r=m,f} c^{(r)} \left(\mu^{(r)} \frac{\partial I_1^{(r)}}{\partial \bar{\mathbf{F}}} + \frac{1}{\epsilon^{(r)}} \frac{\partial I_5^{(r)}}{\partial \bar{\mathbf{F}}} \right) - p\bar{\mathbf{F}}^{-T}, \tag{131}$$

and

$$\bar{\mathbf{E}}^0 = \frac{1}{2} \sum_{r=m,f} \frac{c^{(r)}}{\epsilon^{(r)}} \frac{\partial I_5^{(r)}}{\partial \bar{\mathbf{D}}^0}. \tag{132}$$

The corresponding overall electroelastic moduli are

$$\begin{aligned}
\mathcal{A}^0_{ijkl} &= \frac{1}{2} \sum_{r=m,f} c^{(r)} \left(\mu^{(r)} \frac{\partial^2 I_1^{(r)}}{\partial \bar{\mathbf{F}} \partial \bar{\mathbf{F}}} + \frac{1}{\epsilon^{(r)}} \frac{\partial^2 I_5^{(r)}}{\partial \bar{\mathbf{F}} \partial \bar{\mathbf{F}}} \right), \\
\mathcal{G}^0_{ijk} &= \frac{1}{2} \sum_{r=m,f} \frac{c^{(r)}}{\epsilon^{(r)}} \frac{\partial^2 I_5^{(r)}}{\partial \bar{\mathbf{F}} \partial \bar{\mathbf{D}}^0}, \\
\mathcal{E}^0_{ij} &= \frac{1}{2} \sum_{r=m,f} \frac{c^{(r)}}{\epsilon^{(r)}} \frac{\partial^2 I_5^{(r)}}{\partial \bar{\mathbf{D}}^0 \partial \bar{\mathbf{D}}^0}.
\end{aligned} \tag{133}$$

Finally, with the aid of Eqs. (117) the appropriate coefficients can be determined and substituted in the general instability condition (116).

I examine the behavior of a composite which is subjected to electric excitation corresponding to a nominal electric displacement in the form

$$\bar{\mathbf{D}}^0 = \bar{D}^0 \left(\cos \phi \hat{\mathbf{e}}_1 + \sin \phi \hat{\mathbf{e}}_2 \right), \tag{134}$$

and macroscopically stretched according to the homogeneous deformation gradient

$$\bar{\mathbf{F}} = \lambda \hat{\mathbf{e}}_1 \otimes \hat{\mathbf{e}}_1 + \lambda^{-1} \hat{\mathbf{e}}_2 \otimes \hat{\mathbf{e}}_2 + \hat{\mathbf{e}}_3 \otimes \hat{\mathbf{e}}_3. \tag{135}$$

Consider first the case when $\phi = \pi/2$ and the angle of lamination relative to the applied loading varies. The loading configuration is schematically shown in Fig. 20. I make use of Eqs. (116) and (133) to determine the stable domain of the layered EAP.

40
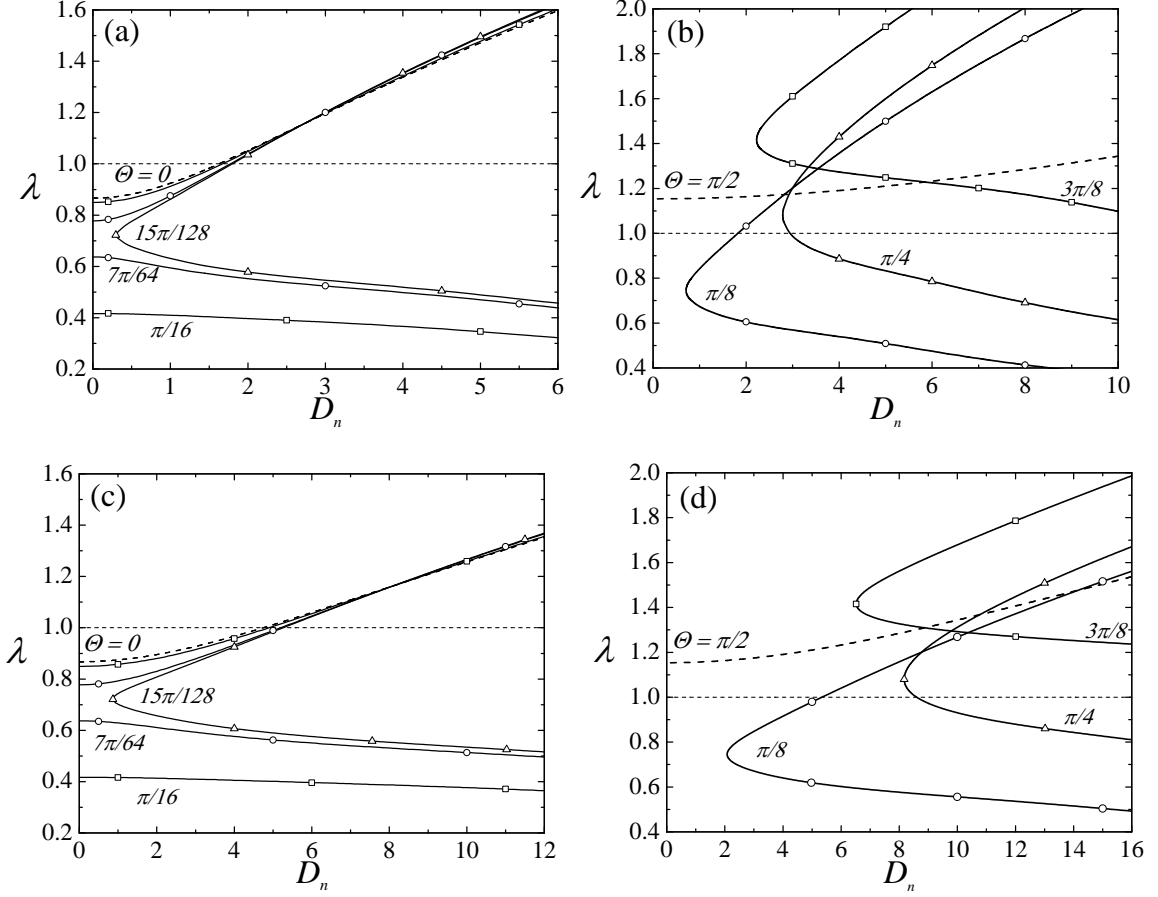
Fig. 15. Bifurcation diagrams of layered materials with different lamination angles as functions of the critical stretch ratio and electric displacement field. The volume fractions of the stiffer phase is $c^{(f)} = 0.2$ for (a) and (b) and $c^{(f)} = 0.8$ for (c) and (d); the phase constant ratios are $k = t = 10$. Figures (a) and (c) are for small lamination angles, and figures (b) and (d) are for large lamination angles.

Shown in Fig. 15 are the analytical estimates for the onset of instabilities in materials with $c^{(f)} = 0.2$ (Figs. 15a and 15b) and $c^{(f)} = 0.8$ (Figs. 15c and 15d), stiffer to softer shear moduli ratio $k \equiv \mu^{(f)}/\mu^{(m)} = 10$ and dielectric constants ratio $t \equiv \epsilon^{(f)}/\epsilon^{(m)} = 10$. Following Triantafyllidis et al. (2006), I plot *failure surfaces* that separate stable domains from those in which instabilities may develop. These bifurcation diagrams are presented as functions of the critical stretch ratio λ_c and the critical electrostatic excitation $D_n = \bar{D}^0/\sqrt{\mu^{(m)}\epsilon^{(m)}}$ for composites with different lamination angles.

Note that in agreement with earlier findings (*e.g.,* Triantafyllidis and Maker, 1985; Nestorovic and Triantafyllidis, 2004; Agoras et al., 2009b; Rudykh and deBotton, 2012), in the purely mechanical case ($D_n = 0$) the composites become unstable only under compression in the lamination direction. Moreover, as the angle between the loading and the lamination directions increases there exists an angle beyond which no macroscopic
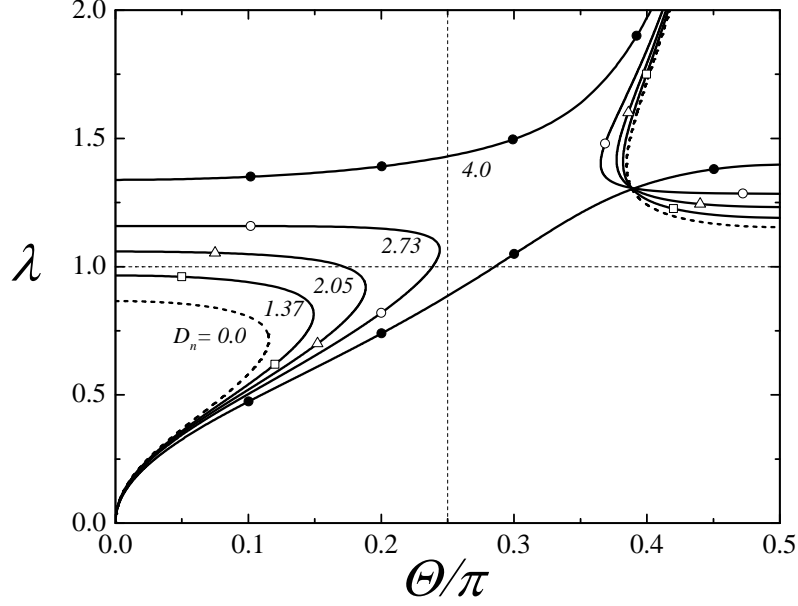
Fig. 16. Bifurcation diagrams of layered materials as functions of the critical stretch ratio and the lamination angle at different levels of electric excitations. The volume fraction of the stiffer phase is $c^{(f)} = 0.2$, the shear moduli ratio is $k = 10$, and the dielectric constants ratio is $t = 10$.

instability occurs (Agoras et al., 2009b). This corresponds to the situation where the layers rotate to an angle $\theta = \pi/4$ in the deformed configuration (Rudykh and deBotton, 2012). At this angle the loading on the layers switches from compression to tension. Consequently, beyond this point no instability is detected. In contrast to the purely mechanical case, under coupled electromechanical loadings instabilities may develop in composites with lamination angles beyond the critical one. The failure surfaces of composites with lamination angles smaller than the critical angle are shown in Figs. 15a and 15c and those of composites with lamination angles larger than the critical one are shown in Figs. 15b and 15d. To highlight the transition from small to large lamination angles I added the curves for the failure surface of a composite with a lamination angle slightly larger than the critical angle ($\Theta = 15\pi/128$) to Figs. 15a and 15c.

One can observe that, in a manner similar to that observed in the purely mechanical case, at low electrostatic fields an increase of the lamination angle stabilizes the composites. However, this effect decays as the applied excitation field is increased, and beyond a certain value the effect is reversed. Specifically, as can be seen in Figs. 15a and 15c, at values of D_n larger than ~ 3.0 for $c^{(f)} = 0.2$ and ~ 10.0 for $c^{(f)} = 0.8$, an increase in Θ may result in earlier onsets of instabilities.

Note that whenever $\Theta = n\pi$ and $\pi/2 + n\pi$, or $n = 0, 1, 2...$, the coefficients $\Gamma_1, \Gamma_3, \Gamma_5$ in Eq. (170) vanish and the condition for ellipticity loss can be written in terms of

42

the bi-cubic polynomial

$$\Gamma_6 \xi^6 + \Gamma_4 \xi^4 + \Gamma_2 \xi^2 + \Gamma_0 = 0. \tag{136}$$

For the case $\Theta = 0$ this result was previously determined by Bertoldi and Gei (2011). The corresponding relation between the critical stretch ratio and the electric excitation is

$$\lambda_c = \left(1 - \frac{\check{\mu}}{\bar{\mu}} + \frac{D^2}{\bar{\mu}\check{\epsilon}} \left(1 - \frac{\check{\epsilon}}{\bar{\epsilon}} \right) \right)^{1/4}, \tag{137}$$

where

$$\bar{\mu} = c^{(m)}\mu^{(m)} + c^{(f)}\mu^{(f)}, \quad \check{\mu} = \left(\frac{c^{(m)}}{\mu^{(m)}} + \frac{c^{(f)}}{\mu^{(f)}} \right)^{-1} \quad \text{and} \quad \check{\epsilon} = \left(\frac{c^{(m)}}{\epsilon^{(m)}} + \frac{c^{(f)}}{\epsilon^{(f)}} \right)^{-1}. \tag{138}$$

Here I find that for the case $\Theta = \pi/2$ the critical stretch ratio is

$$\lambda_c = \left(1 - \frac{\check{\mu}}{\bar{\mu}} \right)^{-1/4} \left(1 + \frac{D^2}{\bar{\mu}\check{\epsilon}} \left(1 - \frac{\check{\epsilon}}{\bar{\epsilon}} \right) \right)^{1/4}. \tag{139}$$

In the purely mechanical case ($D_n = 0$), both expressions (137) and (139) appropriately reduce to the well-known result of Triantafyllidis and Maker (1985).

The bifurcation diagrams of composites with phase volume fractions $c^{(f)} = 0.2$ and material constants similar to the ones considered previously are shown in Fig. 16. To highlight the role of the anisotropy of the material this time the critical stretch ratios are presented as functions of the lamination angle for different electrostatic loading conditions. The curves with square, triangle, white circle and black circle marks correspond to excitation fields $D_n = 1.37$, 2.05, 2.73 and 4.0, respectively. The dashed curve represents the purely mechanical case. This curve is symmetric with respect to the loading direction $\Theta = 0$, that is $\lambda_c(\Theta) = \lambda_c(-\Theta)$, and is also π-periodic, that is, $\lambda_c(\Theta) = \lambda_c(\Theta + \pi j)$, $j = 1, 2, 3...$. Additionally, I note that $\lambda_c(\Theta) = 1/\lambda_c(\Theta + \pi/2)$. In contrast to the purely mechanical case, in general, the electromechanical failure surfaces do not possess the last symmetry due to the different contributions of the electric excitation in the two perpendicular cases.

One can observe that in the purely mechanical case composites with larger lamination angle become more stable (Nestorovic and Triantafyllidis, 2004). This is also true at moderate levels of electric excitations where I note that the topmost curves that emerge from the $\Theta = 0$ axis have a negative slope up to a certain lamination angle beyond which no instability is detected. However, at large enough electrostatic excitation the direction of the slope is reversed (*e.g.,* the curve marked by black circles that corresponds to $\bar{\mathbf{D}}_n = 4.0$). Furthermore, under large electrostatic fields instabilities may occur at any lamination angle.
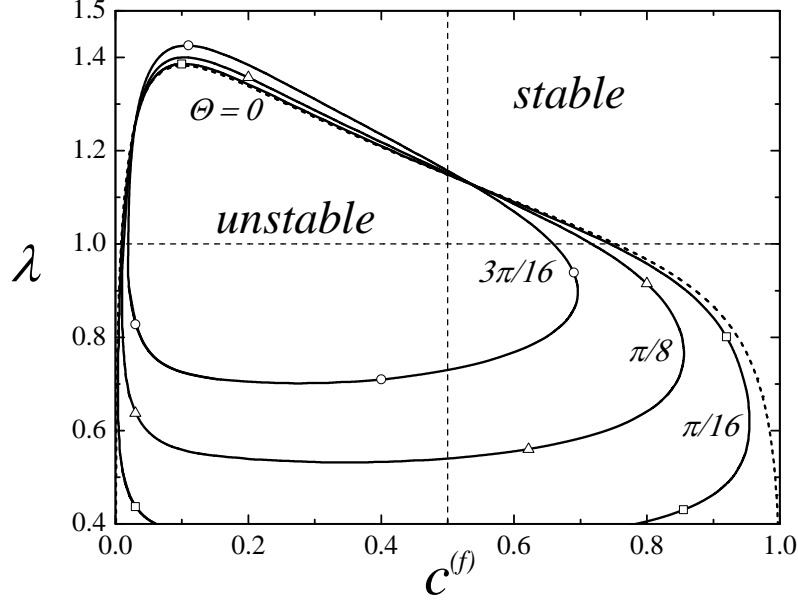
Fig. 17. The failure surfaces of layered composites with different lamination angles as functions of the critical stretch ratio and volume fraction of the stiffer phase subjected to a fixed electrostatic excitation $D_n = 4.0$. The shear moduli ratio is $k = 10$, and the dielectric constants ratio is $t = 10$.

A somewhat different observation is associated with the case where the layers are aligned with the electric field (*i.e.,* $\Theta = \pi/2$). In this limit the electric field stabilizes the material and larger tensile stretch ratios (that correspond to larger compressions along the layers) are required for the onset of instabilities. At moderate levels of electric fields, as the lamination angle of the composite is decreased towards $\Theta = 0$ the critical stretch ratio increases. However, once again at large levels of electric excitations the trend is reversed (see the curve corresponding to $\bar{\mathbf{D}}_n = 4.0$). In this case, as the lamination angle is decreased from $\Theta = \pi/2$ instabilities may occur at lower stretch ratios.

The influence of the volume fraction of the phases on the stability of the composites is depicted in Fig. 17. Bifurcation diagrams for composites with lamination angles $\Theta = 0$, $\pi/16$, $\pi/8$ and $3\pi/16$ subjected to electric excitation $D_n = 4.0$ are plotted as functions of the volume fraction of the stiffer phase (the dashed curve and the continuous curves marked by squares, triangles and circles, respectively).

At both limits of dilute volume fractions of the stiff and the soft phases the materials are stable. Note, however, that the composites with low volume fractions of the stiffer phase are less stable than those with higher concentration of the stiff phase. This tendency is more pronounced for composites with larger lamination angles, for which at the low concentration end the critical stretch ratio is higher than the one for composites with $\Theta = 0$. Conversely, when the volume fraction of the stiffer phase is higher, the critical stretch ratio is lower than the one determined for $\Theta = 0$ and at high enough

44
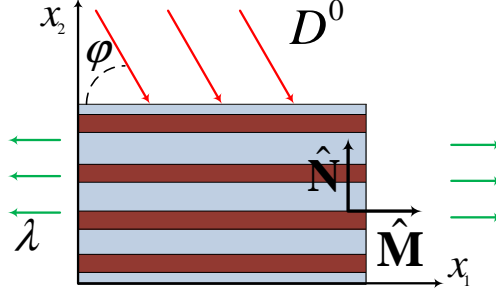
Fig. 18. Electroactive layered composite subjected to electric excitation

volume fractions the material is stable under the applied electrostatic excitation. I emphasize however that at higher electrostatic excitations this trend is reversed, and composites with large lamination angle become less stable even with $c^{(f)} > 0.5$. This can be deduced from Fig. 15c that corresponds to materials with $c^{(f)} = 0.8$. Specifically, note the failure surface for $\Theta = 15\pi/128$ (marked with clear triangles) that demonstrates that at $D_n > 10$ the unstable domain of this material is larger than the ones for composites with smaller lamination angles.

Next, consider the case when the composite is subjected to aligned deformation, *i.e.,* $\Theta = 0$ in Eq. (135) and the angle of applied electric field ϕ in Eq. (134) varies. A schematic representation of this loading mode is depicted in Fig. 18. In this case, the non-zero components of the electroelastic moduli are

$$\mathcal{E}_{11} = 1/\bar{\epsilon}, \quad \mathcal{E}_{22} = \mathcal{E}_{33} = 1/\check{\epsilon}, \tag{140}$$

$$\frac{1}{2}\mathcal{G}_{111} = \mathcal{G}_{122} = \mathcal{G}_{133} = \mathcal{G}_{212} = \mathcal{G}_{313} = \frac{\bar{D}^0 \lambda \cos\phi}{\bar{\epsilon}}, \quad \mathcal{G}_{121} = \mathcal{G}_{211} = \frac{\bar{D}^0 \sin\phi}{\lambda\bar{\epsilon}}$$
$$\frac{1}{2}\mathcal{G}_{222} = \mathcal{G}_{233} = \mathcal{G}_{323} = \frac{\bar{D}^0 \sin\phi}{\lambda\check{\epsilon}}, \tag{141}$$

$$\mathcal{A}_{1111} = \mathcal{A}_{3131} = \mathcal{A}_{3232} = \lambda^2 \left(\bar{\mu} + \frac{\bar{D}^{0\,2} \cos^2\phi}{\bar{\epsilon}} \right),$$

$$\mathcal{A}_{1121} = \mathcal{A}_{1211} = \mathcal{A}_{2122} = \mathcal{A}_{2221} = \mathcal{A}_{3132} = \mathcal{A}_{3231} = \frac{\bar{D}^{0\,2} \cos\phi \sin\phi}{\bar{\epsilon}},$$

$$\mathcal{A}_{1313} = \mathcal{A}_{2323} = \mathcal{A}_{3333} = \bar{\mu}, \quad \mathcal{A}_{1212} = \left(\check{\mu} + \frac{\bar{D}^{0\,2} \sin^2\phi}{\bar{\epsilon}} \right) \lambda^{-2}, \tag{142}$$

$$\mathcal{A}_{1221} = \mathcal{A}_{2112} = \frac{\bar{D}^{0\,2}}{2\lambda^2} \frac{\check{\epsilon} - \bar{\epsilon}}{\check{\epsilon}\bar{\epsilon}} (1 - \cos 2\phi) + \frac{\check{\mu} - \bar{\mu}}{\lambda^2}$$

$$\mathcal{A}_{2121} = \mathcal{A}_{1111} + \mathcal{A}_{1221}, \quad \mathcal{A}_{2222} = \mathcal{A}_{3232} = \left(\bar{\mu} + \frac{\bar{D}^{0\,2} \sin^2\phi}{\check{\epsilon}} \right) \lambda^{-2}.$$

Obviously, for the cases when $\phi = n\pi$ and $\pi/2 + n\pi$, where $n = 0, 1, 2, ...$, the condition for ellipticity loss (116) reduces to the bi-cubic polynomial Eq. (136). In the case when

45
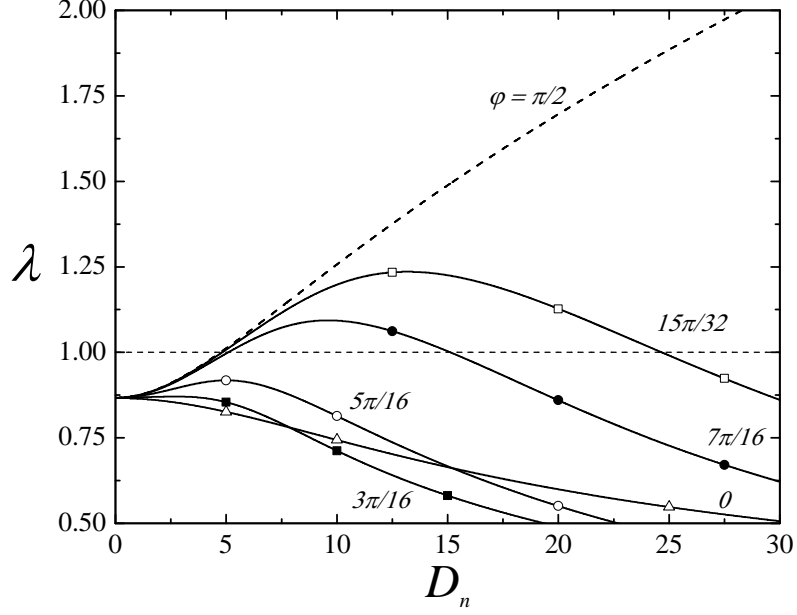
Fig. 19. Bifurcation diagrams of layered materials subjected to aligned stretch and electrostatic excitation at different angles as functions of the critical stretch ratio and electric displacement. The volume fraction of the stiff phase is $c^{(f)} = 0.8$ and the contrasts between the elastic and dielectric moduli are $k = t = 10$.

$\phi = n\pi$ the critical stretch ratio can be explicitly determined.

$$\lambda_c = \left(1 - \frac{\breve{\mu}}{\bar{\mu}}\right)^{1/4} \left(1 + \frac{D^2}{\bar{\mu}\bar{\epsilon}} \left(1 - \frac{\breve{\epsilon}}{\bar{\epsilon}}\right)\right)^{-1/4}. \tag{143}$$

Naturally, this expression is the reciprocal of the one given in Eq. (139).

Bifurcation diagrams as functions of λ_c and D_n are presented in Fig. 19 for $c^{(f)} = 0.8$, and contrast between the shear moduli $k = 10$ and dielectric constants $t = 10$. The diagrams are shown for different angles $\phi = 0$, $3\pi/16$, $5\pi/16$, $7\pi/16$, $15\pi/32$ and $\pi/2$. These correspond to the continuous curves marked by triangles, solid squares, circles, solid circles, squares and the dashed curve, respectively. The regions beneath the curves correspond to the unstable domains.

The influence of the angle of the applied electric displacement shows that the most sensitive structure is the one with $\phi = \pi/2$, as its bifurcation curve lies above the ones for $\phi < \pi/2$. It is easy to see from Fig. 19 that for some values of ϕ the composite becomes stable even at large intensities of electric excitation. For example, a composite subjected to the electric excitations at $\phi = 3\pi/16$ is stable even when subjected to large compressive stretch ratios along the layers.

Chapter 4

Microscopic Instabilities in EAPs

Electromechanical instabilities in composite media may occur at any scale. To identify the onset of bifurcations, the Bloch-Floquet technique is applied to periodic media. Motivated by possible applications where the electric excitation is controlled by the potential, here, contrary to the previous work of Bertoldi and Gei (2011) the analysis is performed in terms of the referential electric field instead of electric displacement. To connect the microscopic instability analysis to the macroscopic one, the corresponding macroscopic instability criterion is derived in terms of the referential electric field.

4.1 Theory.

Consider a layered dielectric composite made out of two incompressible phases with volume fractions $c^{(m)}$ and $c^{(f)} = 1 - c^{(m)}$. Here and thereafter, the fields and parameters of the stiffer and the softer phases are denoted by superscripts $(\bullet)^{(f)}$ and $(\bullet)^{(m)}$, respectively. Geometrically, the layers are characterized by their thicknesses $h^{(m)} = hc^{(m)}$ and $h^{(f)} = hc^{(f)}$. The direction normal to the layer plane is the laminate direction $\hat{\mathbf{N}}$, and $\hat{\mathbf{M}}$ is a unit vector tangent to the interface, both in the undeformed configuration (see Fig. 20). Assuming that along the primary branch of the solution all the fields are homogeneous in each phase, I have that the mean nominal electric field in the composite is

$$\bar{\mathbf{E}}^0 = c^{(m)}\mathbf{E}^{0\,(m)} + c^{(f)}\mathbf{E}^{0\,(f)}. \tag{144}$$

The continuity condition on the electric field is

$$\left(\mathbf{E}^{0\,(m)} - \mathbf{E}^{0\,(f)}\right) \cdot \hat{\mathbf{M}} = 0 \quad \text{or} \quad \mathbf{E}^{0\,(m)} - \mathbf{E}^{0\,(f)} = \beta\hat{\mathbf{N}}, \tag{145}$$

where β is a scalar. Accordingly, the referential electric field in each phase can be expressed in the form

$$\mathbf{E}^{0\,(m)} = \bar{\mathbf{E}}^0 + c^{(f)}\beta\hat{\mathbf{N}} \quad \text{and} \quad \mathbf{E}^{0\,(f)} = \bar{\mathbf{E}}^0 - c^{(m)}\beta\hat{\mathbf{N}}. \tag{146}$$

Since the interface is charge free, the continuity condition on the referential electric displacement field is

$$\left(\mathbf{D}^{0\,(m)} - \mathbf{D}^{0\,(f)}\right) \cdot \hat{\mathbf{N}} = 0. \tag{147}$$
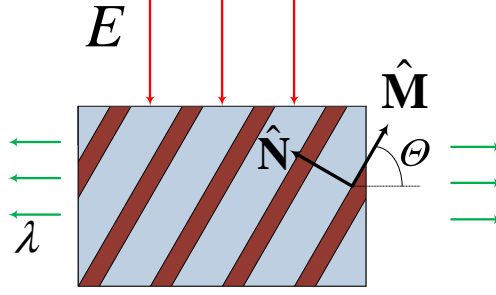
Fig. 20. Electroactive layered composite subjected to electric excitation.

For incompressible laminates the displacement continuity condition (deBotton, 2005) leads to

$$\mathbf{F}^{(m)} = \bar{\mathbf{F}}\left(\mathbf{I} + c^{(f)}\alpha\hat{\mathbf{M}} \otimes \hat{\mathbf{N}}\right) \quad \text{and} \quad \mathbf{F}^{(f)} = \bar{\mathbf{F}}\left(\mathbf{I} - c^{(m)}\alpha\hat{\mathbf{M}} \otimes \hat{\mathbf{N}}\right), \tag{148}$$

where α is a constant. The corresponding interface stress continuity condition (deBotton et al., 2007; Tevet-Deree, 2008) is

$$\left(\mathbf{P}^{(m)} - \mathbf{P}^{(f)}\right) \cdot \hat{\mathbf{N}} = 0. \tag{149}$$

Once the constitutive relations for phases are prescribed, the constants α and β can be determined from the continuity conditions (147) and (149). This completes the solution up to a bifurcation point.

To determine the onset of instabilities in the composites an analysis similar to that used by Triantafyllidis and Maker (1985) and Bertoldi and Gei (2011) is adopted. In each phase I seek a solution of (20) in the form

$$v_i = \tilde{v}_i(x_2)\exp(ik_1x_1), \quad \dot{p} = \tilde{q}(x_2)\exp(ik_1x_1), \quad \dot{E}_i = \tilde{e}_i(x_2)\exp(ik_1x_1), \tag{150}$$

where k_1 is the wave number along the x_1-direction. The incompressibility constraint together with the absence of the electric field vorticity provide two equations for $\tilde{v}_i$ and $\tilde{e}_i$

$$\tilde{v}_2' = -ik_1\tilde{v}_1 \quad \text{and} \quad \tilde{e}_1' = ik_1\tilde{e}_2, \tag{151}$$

where the notation $(\bullet)' = (\bullet)_{,2}$ is introduced. The resulting incremental governing
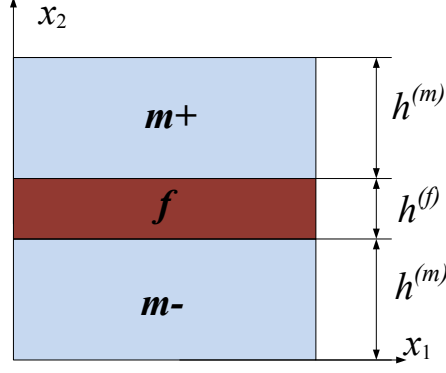
Fig. 21. The unit cell of the layered media.

equations (20) reads

$$k_1^2 \left(\mathcal{A}_{1122} + \mathcal{A}_{1221} - \mathcal{A}_{1111} \right) \tilde{v}_1 + ik_1 \left(2\mathcal{A}_{1112} - \mathcal{A}_{1222} \right) \tilde{v}_1' + \mathcal{A}_{1212} \tilde{v}_1'' - k_1^2 \mathcal{A}_{1121} \tilde{v}_2 +$$
$$ik_1 \mathcal{G}_{111} \tilde{e}_1 + ik_1 \left(\mathcal{G}_{112} + \mathcal{G}_{121} \right) \tilde{e}_2 + \mathcal{G}_{122} \tilde{e}_2' - ik_1 \tilde{q} = 0, \tag{152}$$

$$k_1^2 \left(2\mathcal{A}_{2122} - \mathcal{A}_{1121} \right) \tilde{v}_1 + ik_1 \left(\mathcal{A}_{1221} + \mathcal{A}_{1122} - \mathcal{A}_{2222} \right) \tilde{v}_1' + \mathcal{A}_{1222} \tilde{v}_1'' - k_1^2 \mathcal{A}_{2121} \tilde{v}_2 +$$
$$ik_1 \mathcal{G}_{121} \tilde{e}_1 + ik_1 \left(\mathcal{G}_{122} + \mathcal{G}_{221} \right) \tilde{e}_2 + \mathcal{G}_{222} \tilde{e}_2' - \tilde{q}' = 0, \tag{153}$$

$$k_1^2 \left(\mathcal{G}_{122} + \mathcal{G}_{221} - \mathcal{G}_{111} \right) \tilde{v}_1 + ik_1 \left(\mathcal{G}_{112} + \mathcal{G}_{121} - \mathcal{G}_{222} \right) \tilde{v}_1' + \mathcal{G}_{122} \tilde{v}_1'' - k_1^2 \mathcal{G}_{121} \tilde{v}_2 +$$
$$ik_1 \mathcal{E}_{11} \tilde{e}_1 + 2ik_1 \mathcal{E}_{12} \tilde{e}_2 + \mathcal{E}_{22} \tilde{e}_2' = 0, \tag{154}$$

Equations (151)-(154) provide a set of 6 linear homogeneous first order differential equations that depends on the vector of 6 unknowns $\tilde{\mathbf{u}} = (\tilde{v}_1,\ \tilde{v}_2,\ \tilde{e}_1,\ \tilde{e}_2,\ \tilde{q},\ \tilde{v}_1')$

$$\mathbf{R}\tilde{\mathbf{u}} = \tilde{\mathbf{u}}'. \tag{155}$$

The components of the matrix $\mathbf{R}$ are given in Appendix C. The solution of the system can be determined in the form

$$\tilde{\mathbf{u}} = \mathbf{B}\mathbf{Z}\mathbf{s}, \tag{156}$$

where $\mathbf{s}$ is an arbitrary constant vector that will be determined later from the continuity and quasi-periodicity conditions on the unit cell. In (156), $\mathbf{Z}(x_2) = \text{diag}[\exp(\mathbf{z}x_2)]$ is the diagonal matrix of the eigenvalues vector $\mathbf{z}$ of the matrix $\mathbf{R}$ and the corresponding eigenvectors of $\mathbf{R}$ are the columns of the matrix $\mathbf{B}$.

Consider the periodic unit cell (Fig. 21) of the layered composite. The quasi periodic boundary conditions are

$$\tilde{\mathbf{u}}\left(x_2 + h\right) = \tilde{\mathbf{u}}\left(x_2\right) \exp(ik_2 h), \tag{157}$$

where $k_2 \in [0,\ 2\pi/h]$ is the solution periodicity parameter, also referred to as Floquet

parameter. In the interval $0 < x_2 < h + h^{(m)}$ the solution (156) attains the form

$$
\begin{aligned}
\tilde{\mathbf{u}}(x_2) &= \overset{m}{\mathbf{B}}\overset{m}{\mathbf{Z}}(x_2)\overset{m-}{\mathbf{s}}, \quad 0 < x_2 < h^{(m)}, \\
\tilde{\mathbf{u}}(x_2) &= \overset{f}{\mathbf{B}}\overset{f}{\mathbf{Z}}(x_2)\overset{f}{\mathbf{s}}, \quad h^{(m)} < x_2 < h, \\
\tilde{\mathbf{u}}(x_2) &= \overset{m}{\mathbf{B}}\overset{m}{\mathbf{Z}}(x_2)\overset{m+}{\mathbf{s}}, \quad h < x_2 < h + h^{(m)},
\end{aligned} \tag{158}
$$

where $\overset{m}{\mathbf{z}}, \overset{f}{\mathbf{z}}$ are the eigenvalues of $\mathbf{R}$ in which the electroelastic moduli correspond to the appropriate phase, $\overset{m}{\mathbf{B}}$ and $\overset{f}{\mathbf{B}}$ are the corresponding matrices of eigenvectors. Substitution of (158) into (157) yields

$$
\overset{m+}{\mathbf{s}} = \exp(ik_2 h)\left(\overset{m}{\mathbf{Z}}(h)\right)^{-1}\overset{m-}{\mathbf{s}}. \tag{159}
$$

The jump conditions of the incremental fields at the interfaces are

$$
[[v]] = 0, \quad [[\dot{\mathbf{T}}]]\mathbf{n} = \mathbf{0}, \quad [[\dot{\mathbf{D}}]] \cdot \mathbf{n} = 0 \quad \text{and} \quad \mathbf{n} \times [[\dot{\mathbf{E}}]] = 0, \tag{160}
$$

where $\mathbf{n} = \mathbf{F}^{-T}\hat{\mathbf{N}}$ is normal to the interface at the current configuration, and the notation $[[\bullet]] \equiv (\bullet)^+ - (\bullet)^-$ is used. By making use of (150) and (151) the jump conditions (160) are

$$
[[\tilde{v}_1]] = 0, \quad [[\tilde{v}_2]] = 0, \quad [[\tilde{e}_1]]n_2 - [[\tilde{e}_2]]n_1 = 0, \tag{161}
$$

$$
\begin{aligned}
&[[ik_1(\mathcal{A}_{1111} - \mathcal{A}_{1122} + p)\tilde{v}_1 + \mathcal{A}_{1112}\tilde{v}_1' + ik_1\mathcal{A}_{1121}\tilde{v}_2 + \mathcal{G}_{111}\tilde{e}_1 + \mathcal{G}_{112}\tilde{e}_2 - \tilde{q}]]n_1 + \\
&[[ik_1(\mathcal{A}_{1211} - \mathcal{A}_{1222})\tilde{v}_1 + \mathcal{A}_{1212}\tilde{v}_1' + ik_1(\mathcal{A}_{1221} + p)\tilde{v}_2 + \mathcal{G}_{121}\tilde{e}_1 + \mathcal{G}_{122}\tilde{e}_2]]n_2 = 0,
\end{aligned} \tag{162}
$$

$$
\begin{aligned}
&[[ik_1(\mathcal{A}_{2111} - \mathcal{A}_{2122})\tilde{v}_1 + (\mathcal{A}_{2112} + p)\tilde{v}_1' + ik_1\mathcal{A}_{2121}\tilde{v}_2 + \mathcal{G}_{211}\tilde{e}_1 + \mathcal{G}_{212}\tilde{e}_2]]n_1 + \\
&[[ik_1(\mathcal{A}_{2211} - \mathcal{A}_{2222} - p)\tilde{v}_1 + \mathcal{A}_{2212}\tilde{v}_1' + ik_1\mathcal{A}_{2221}\tilde{v}_2 + \mathcal{G}_{221}\tilde{e}_1 + \mathcal{G}_{222}\tilde{e}_2 - \tilde{q}]]n_2 = 0,
\end{aligned} \tag{163}
$$

$$
\begin{aligned}
&[[ik_1(\mathcal{G}_{111} - \mathcal{G}_{221})\tilde{v}_1 + \mathcal{G}_{121}\tilde{v}_1' + ik_1\mathcal{G}_{211}\tilde{v}_2 + \mathcal{E}_{11}\tilde{e}_1 + \mathcal{E}_{12}\tilde{e}_2]]n_1 + \\
&[[ik_1(\mathcal{G}_{112} - \mathcal{G}_{222})\tilde{v}_1 + \mathcal{G}_{122}\tilde{v}_1' + ik_1\mathcal{G}_{212}\tilde{v}_2 + \mathcal{E}_{12}\tilde{e}_1 + \mathcal{E}_{22}\tilde{e}_2]]n_2 = 0,
\end{aligned} \tag{164}
$$

Equations (161)-(164) can be written in the form $[[\mathbf{Q}\tilde{\mathbf{u}}]] = 0$. The non-zero entries of the matrix $\mathbf{Q}$ are

$$
\begin{aligned}
Q_{11} &= Q_{22} = 1, \quad Q_{33} = n_2, \quad Q_{34} = -n_2, \\
Q_{41} &= ik_1\Big((\mathcal{A}_{1111} - \mathcal{A}_{1122} + p)n_1 + (\mathcal{A}_{1211} - \mathcal{A}_{1222})n_2\Big) \\
Q_{42} &= ik_1\Big(\mathcal{A}_{1121}n_1 + (\mathcal{A}_{1211} + p)n_2\Big), \quad Q_{43} = \mathcal{G}_{111}n_1 + \mathcal{G}_{121}n_2, \quad Q_{44} = \mathcal{G}_{112}n_1 + \mathcal{G}_{122}n_2, \\
Q_{45} &= -n_1, \quad Q_{46} = \mathcal{A}_{1112}n_1 + \mathcal{A}_{1212}n_2, \\
Q_{51} &= ik_1\Big((\mathcal{A}_{2111} - \mathcal{A}_{2122})n_1 + (\mathcal{A}_{2211} - \mathcal{A}_{2222} - p)n_2\Big), \quad Q_{52} = ik_1(\mathcal{A}_{2121}n_1 + \mathcal{A}_{2221}n_2), \\
Q_{53} &= \mathcal{G}_{211}n_1 + \mathcal{G}_{221}n_2, \quad Q_{54} = \mathcal{G}_{212}n_1 + \mathcal{G}_{222}n_2, \quad Q_{55} = -n_2, \\
Q_{56} &= (\mathcal{A}_{2112} + p)n_1 + \mathcal{A}_{2212}n_2, \\
Q_{61} &= ik_1\Big((\mathcal{G}_{111} - \mathcal{G}_{221})n_1 + (\mathcal{G}_{112} - \mathcal{G}_{222})n_2\Big), \quad Q_{62} = ik_1(\mathcal{G}_{211}n_1 + \mathcal{G}_{212}n_2), \\
Q_{63} &= \mathcal{E}_{11}n_1 + \mathcal{E}_{12}n_2, \quad Q_{64} = \mathcal{E}_{12}n_1 + \mathcal{E}_{22}n_2, \quad Q_{66} = \mathcal{G}_{121}n_1 + \mathcal{G}_{122}n_2.
\end{aligned} \tag{165}
$$

Finally, upon usage of (158) I have that

$$
\overset{m}{\mathbf{Q}}\overset{m}{\mathbf{B}}\overset{m}{\mathbf{Z}}\left(h^{(m)}\right)\overset{m-}{\mathbf{s}} = \overset{f}{\mathbf{Q}}\overset{f}{\mathbf{B}}\overset{f}{\mathbf{Z}}\left(h^{(m)}\right)\overset{f}{\mathbf{s}},
$$

$$
\overset{m}{\mathbf{Q}}\overset{m}{\mathbf{B}}\overset{m}{\mathbf{Z}}(h)\overset{m+}{\mathbf{s}} = \overset{f}{\mathbf{Q}}\overset{f}{\mathbf{B}}\overset{f}{\mathbf{Z}}(h)\overset{f}{\mathbf{s}}.
\tag{166}
$$

The combination of (159) and (166) leads to the condition for the existence of a non-trivial solution

$$
\det\left[\left(\overset{m}{\mathbf{Q}}\overset{m}{\mathbf{B}}\right)^{-1}\overset{f}{\mathbf{Q}}\overset{f}{\mathbf{B}}\overset{f}{\mathbf{Z}}\left(h^{(f)}\right)\left(\overset{f}{\mathbf{Q}}\overset{f}{\mathbf{B}}\right)^{-1}\overset{m}{\mathbf{Q}}\overset{m}{\mathbf{B}}\overset{m}{\mathbf{Z}}\left(h^{(m)}\right) - \mathbf{I}\exp(ik_2 h)\right] = 0.
\tag{167}
$$

When condition (167) is satisfied for a combination of mechanical and electrical loads, a solution in the form of Eq. (150) that satisfies Eqs. (157) and (158) exists where k_2 represents the scale of the periodicity of the solution. A similar condition was derived by Triantafyllidis and Maker (1985) for the purely mechanical case and by Bertoldi and Gei (2011) for layered composites with isotropic neo-Hookean phases subjected to a pre-stretch along the layers and electrical displacement excitation perpendicular to the surface.

In the preceding analysis no assumption regarding the phase behavior is made and the composites with *anisotropic* phases can be examined. Moreover, the derived condition can be used for any planar combination of mechanical and electrical loads and is not restricted to the aligned pre-stretch and perpendicular electric excitation (Bertoldi and Gei, 2011).

I recall that Geymonat et al. (1993) rigorously showed in the purely mechanical case that the macroscopic instability onset corresponds to the existence of a non-trivial solution in the long-wave limit $k_1 h \to 0$. A more compact analysis similar to that used by Hill and Hutchinson (1975) can be used for this specific limit of long waves. In the content of the coupled problem, Bertoldi and Gei (2011) demonstrated that the macroscopic instability analysis agrees with the onset of long wave instabilities in layered composites with isotropic neo-Hookean phases subjected to a pre-stretch along the layers and electrical displacement excitation perpendicular to the layers.

Motivated by these works I seek a solution for (20) in the form

$$
v_i = \tilde{v}_i f(\hat{\mathbf{a}} \cdot \mathbf{x}), \quad \dot{p} = \tilde{q} f'(\hat{\mathbf{a}} \cdot \mathbf{x}), \quad \dot{E}_i = \tilde{e}_i f'(\hat{\mathbf{a}} \cdot \mathbf{x}),
\tag{168}
$$

where f is a continuous and sufficiently differentiable function, $\hat{\mathbf{a}}$ is a unit vector; $\tilde{v}_i$, $\tilde{e}_i$ and $\tilde{q}$ are incremental macroscopic quantities which are independent of $\mathbf{x}$. The incompressibility constraint together with the last of (19) provide additional equations for $\tilde{v}_i$ and $\tilde{e}_i$. In particular, for a plane problem

$$
\tilde{v}_1 = -\xi\tilde{v}_2 \quad \text{and} \quad \tilde{e}_1 = \xi^{-1}\tilde{e}_2,
\tag{169}
$$

where $\xi \equiv a_2/a_1$. Upon substitution of expressions (168) together with (169) into (20), elimination of the pressure increment leads to a polynomial equation in ξ, namely

$$\Gamma_6\xi^6 + \Gamma_5\xi^5 + \Gamma_4\xi^4 + \Gamma_3\xi^3 + \Gamma_2\xi^2 + \Gamma_1\xi + \Gamma_0 = 0, \tag{170}$$

where the coefficients Γ_i are given by the electroelastic moduli as follows

$$\Gamma_0 = \mathcal{G}_{121}^2 - \mathcal{A}_{2121}\mathcal{E}_{11}, \tag{171}$$

$$\Gamma_1 = 2\left(-\mathcal{A}_{2121}\mathcal{E}_{12} + (\mathcal{A}_{1121} - \mathcal{A}_{2122})\mathcal{E}_{11} + \mathcal{G}_{121}\left(\mathcal{G}_{221} + \mathcal{G}_{122} - \mathcal{G}_{111}\right)\right), \tag{172}$$

$$\begin{aligned}\Gamma_2 = &-\mathcal{A}_{2121}\mathcal{E}_{22} + 4\left(\mathcal{A}_{1121} - \mathcal{A}_{2122}\right)\mathcal{E}_{12} - \left(\mathcal{A}_{1111} - 2\mathcal{A}_{1122} - 2\mathcal{A}_{1221} + \mathcal{A}_{2222}\right)\mathcal{E}_{11}\\ &- 2\mathcal{G}_{121}\left(\mathcal{G}_{112} + \mathcal{G}_{121} - \mathcal{G}_{222}\right) + \left(\mathcal{G}_{122} + \mathcal{G}_{221} - \mathcal{G}_{111}\right)^2,\end{aligned} \tag{173}$$

$$\begin{aligned}\Gamma_3 = &-2((\mathcal{A}_{1112} - \mathcal{A}_{1222})\mathcal{E}_{11} + (\mathcal{A}_{1111} - 2\mathcal{A}_{1122} - 2\mathcal{A}_{1221} + \mathcal{A}_{2222})\mathcal{E}_{12}\\ &+ (\mathcal{A}_{2122} - \mathcal{A}_{1121})\mathcal{E}_{22} + (\mathcal{G}_{121}\mathcal{G}_{122} - (\mathcal{G}_{111} - \mathcal{G}_{122} - \mathcal{G}_{221})(\mathcal{G}_{112} + \mathcal{G}_{121} - \mathcal{G}_{222}))),\end{aligned} \tag{174}$$

$$\begin{aligned}\Gamma_4 = &-\left(\mathcal{A}_{1111} - 2\mathcal{A}_{1122} - 2\mathcal{A}_{1221} + \mathcal{A}_{2222}\right)\mathcal{E}_{22} - 4\left(\mathcal{A}_{1112} - \mathcal{A}_{1222}\right)\mathcal{E}_{12}\\ &- \mathcal{A}_{1212}\mathcal{E}_{11} + \left(\mathcal{G}_{112} + \mathcal{G}_{121} - \mathcal{G}_{222}\right)^2 + 2\mathcal{G}_{122}\left(\mathcal{G}_{111} - \mathcal{G}_{122} - \mathcal{G}_{221}\right),\end{aligned} \tag{175}$$

$$\Gamma_5 = 2\left(\left(\mathcal{A}_{1222} - \mathcal{A}_{1112}\right)\mathcal{E}_{22} - \mathcal{A}_{1212}\mathcal{E}_{12} + \mathcal{G}_{122}(\mathcal{G}_{112} + \mathcal{G}_{121} - \mathcal{G}_{222})\right), \tag{176}$$

$$\Gamma_6 = \mathcal{G}_{122}^2 - \mathcal{A}_{1212}\mathcal{E}_{22}. \tag{177}$$

When a real solution of (170) exists an instability associated with plane waves may occur. Note that the general condition (170) can be utilized for the macroscopic instability analysis of *multiphase* hyperelastic dielectrics since no restricting assumption was made in its derivation. Once the macroscopic electroelastic moduli are determined either via a homogenization technique or numerically (Rudykh and deBotton, 2012, for mechanical loads), the stable domains can be deduced from (170) for any microstructure and any planar mechanical and electrical loading.

In the case of laminated composites going back to Eqs. (147) and (149) from which the solution for the boundary value problem can be deduced, the energy-density function of the composite can be expressed as the weighted sum of the phase energy-density functions, namely

$$\tilde{\Psi}(\bar{\mathbf{F}}, \bar{\mathbf{E}}^0) = \sum_{r=m,f} c^{(r)}\Psi^{(r)}(\bar{\mathbf{F}}, \bar{\mathbf{E}}^0). \tag{178}$$

The average nominal stress tensor and electric displacement are

$$\bar{\mathbf{P}} = \frac{\partial\tilde{\Psi}}{\partial\bar{\mathbf{F}}} - p\bar{\mathbf{F}}^{-T} \quad\text{and}\quad \bar{\mathbf{D}}^0 = -\frac{\partial\tilde{\Psi}}{\partial\bar{\mathbf{E}}^0}. \tag{179}$$

The macroscopic electroelastic moduli are given by

$$\tilde{\mathcal{A}}^0_{ijkl} = \frac{\partial^2 \tilde{\Psi}}{\partial \bar{\mathbf{F}} \partial \bar{\mathbf{F}}}, \quad \tilde{\mathcal{G}}^0_{ijk} = \frac{\partial^2 \tilde{\Psi}}{\partial \bar{\mathbf{F}} \partial \bar{\mathbf{E}}^0} \quad \text{and} \quad \tilde{\mathcal{E}}^0_{ij} = \frac{\partial^2 \tilde{\Psi}}{\partial \bar{\mathbf{E}}^0 \partial \bar{\mathbf{E}}^0}. \tag{180}$$

Together with (17) the electroelastic moduli (180) provide the coefficients for the polynomial equation (170), consequently the onset of the macroscopic instabilities can be determined.

4.2   Examples.

In the case of an isotropic material, the energy-density function Ψ can be expressed in terms of the invariants of the Cauchy-Green strain tensor $\mathbf{C} \equiv \mathbf{F}^T \mathbf{F}$ and the nominal electric field $\mathbf{E}^0$ Dorfmann and Ogden (2005). It is possible to express these invariants in the form

$$I_1 = \text{Tr} \mathbf{C}, \quad I_2 = \frac{1}{2}(I_1^2 - \text{Tr}(\mathbf{C}\mathbf{C})), \quad I_3 = \det \mathbf{C}, \tag{181}$$

$$I_{4e} = \mathbf{E}^0 \cdot \mathbf{E}^0, \quad I_{5e} = \mathbf{E}^0 \cdot \mathbf{C}^{-1} \mathbf{E}^0, \quad I_{6e} = \mathbf{E}^0 \cdot \mathbf{C}^{-2} \mathbf{E}^0. \tag{182}$$

Accordingly, the energy-density function can be written as

$$\Psi \left(\mathbf{F}, \mathbf{E}^0 \right) = \Psi \left(I_1, I_2, I_3, I_{4e}, I_{5e}, I_{6e} \right). \tag{183}$$

As an example, I examine composites whose phase behaviors are characterized by a constitutive model of neo-Hookean soft dielectrics, namely

$$\Psi = \frac{\mu}{2} \left(I_1 - 3 \right) - \frac{\epsilon}{2} I_{5e}, \tag{184}$$

where μ is the shear modulus. For this choice of energy-density function, α in Eq. (148) is expressed as (deBotton, 2005)

$$\alpha = \frac{\mu^{(f)} - \mu^{(m)}}{c^{(m)} \mu^{(f)} + c^{(f)} \mu^{(m)}} \frac{\bar{\mathbf{F}} \hat{\mathbf{N}} \cdot \bar{\mathbf{F}} \hat{\mathbf{M}}}{\bar{\mathbf{F}} \hat{\mathbf{M}} \cdot \bar{\mathbf{F}} \hat{\mathbf{M}}}, \tag{185}$$

Combining (147) with (146) and the constitutive law for each phase

$$\mathbf{D}^{0\,(r)} = \epsilon^{(r)} J^{(r)} \mathbf{F}^{(r)-1} \mathbf{F}^{(r)-T} \mathbf{E}^{0\,(r)}, \tag{186}$$

together with (148), (185) and noting that $\mathbf{F}^{(r)-T} \hat{\mathbf{N}} = \bar{\mathbf{F}}^{-T} \hat{\mathbf{N}}$ one can find that

$$\beta = \frac{\epsilon^{(f)} - \epsilon^{(m)}}{c^{(m)} \epsilon^{(f)} + c^{(f)} \epsilon^{(m)}} \frac{\left(\bar{\mathbf{F}}^{-T} \bar{\mathbf{E}}^0 \right) \cdot \left(\bar{\mathbf{F}}^{-T} \hat{\mathbf{N}} \right)}{\left(\bar{\mathbf{F}}^{-T} \hat{\mathbf{N}} \right) \cdot \left(\bar{\mathbf{F}}^{-T} \hat{\mathbf{N}} \right)} + \alpha \bar{\mathbf{E}}^0 \cdot \hat{\mathbf{M}}. \tag{187}$$

The difference between pressure in the two phases is

$$p^{(m)} - p^{(f)} = \frac{\left(\epsilon^{(f)} - \epsilon^{(m)}\right) \dfrac{\check{\epsilon}^2}{\epsilon^{(m)}\epsilon^{(f)}} \left(\left(\bar{\mathbf{F}}^{-T}\bar{\mathbf{E}}^0\right) \cdot \left(\bar{\mathbf{F}}^{-T}\hat{\mathbf{N}}\right)\right)^2 + \mu^{(m)} - \mu^{(f)}}{\left(\bar{\mathbf{F}}^{-T}\hat{\mathbf{N}}\right) \cdot \left(\bar{\mathbf{F}}^{-T}\hat{\mathbf{N}}\right)}, \qquad (188)$$

where

$$\check{\epsilon} = \left(\frac{c^{(m)}}{\epsilon^{(m)}} + \frac{c^{(f)}}{\epsilon^{(f)}}\right)^{-1}. \qquad (189)$$

Expression (188) reduces to the result obtained by deBotton (2005) in the purely mechanical case. Note that (185), (187) and (188) provide an exact solution for the fields in each phase as functions of the average macroscopic deformation gradient $\bar{\mathbf{F}}$ and the nominal electric field $\bar{\mathbf{E}}^0$. These expressions for the fields can be used in the analysis to determine the onset of the microscopic instabilities.

Moreover, the total energy-density function of the composite is an exact expression obtained upon substitution of (185) and (187) into (178). Consequently, the electroelastic moduli in Eq. (180) for the composite are explicit expressions stemming from the solution of the homogenization problem. In turn, the onset of the macroscopic failure can be determined by finding a real root of the characteristic equation (170).

I examine the case where, in the undeformed configuration, the applied electric field is aligned with one of the principal axes of the deformation gradient, namely

$$\bar{\mathbf{E}}^0 = E_2 \bar{\mathbf{e}}_2 \quad \text{and} \quad \bar{\mathbf{F}} = \lambda \bar{\mathbf{e}}_1 \otimes \bar{\mathbf{e}}_1 + \lambda^{-1}\bar{\mathbf{e}}_2 \otimes \bar{\mathbf{e}}_2 + \bar{\mathbf{e}}_3 \otimes \bar{\mathbf{e}}_3, \qquad (190)$$

(see Fig. 20). However, in general the layer directions are not aligned with the principal system and in terms of the lamination angle are

$$\hat{\mathbf{N}} = \sin\Theta\,\bar{\mathbf{e}}_1 + \cos\Theta\,\bar{\mathbf{e}}_2 \quad \text{and} \quad \hat{\mathbf{M}} = \cos\Theta\,\bar{\mathbf{e}}_1 - \sin\Theta\,\bar{\mathbf{e}}_2. \qquad (191)$$

The analytical expressions for the governing matrices of the microscopic instability analysis $\mathbf{Q}$ and $\mathbf{R}$ are rather complicated in general. However, for the aligned case $\Theta = 0$, a significant simplification occurs, in particular the non zero entries of $\mathbf{R}$ are

$$R_{12} = 1, \quad R_{21} = k_1^2\lambda^4\left(1 + E_2^2\frac{\epsilon}{\mu}\right), \quad R_{25} = -ik_1 E_2\frac{\epsilon}{\mu}\lambda^3, \quad R_{26} = \frac{ik_1\lambda^2}{\mu}, \, R_{31} = -ik_1,$$

$$R_{45} = ik_1, \quad R_{52} = -ik_1 E_2\lambda, \quad R_{53} = -k_1^2 E_2\lambda, \quad R_{54} = -ik_1, \quad R_{62} = -ik_1\mu\lambda^{-2},$$

$$R_{63} = -k_1^2\lambda^2(\mu + \epsilon E_2^2), \quad R_{64} = -k_1^2\epsilon E_2\lambda. \qquad (192)$$

The corresponding non-zero entries of the matrix $\mathbf{Q}$ are

$$Q_{11} = 1, \quad Q_{23} = 1, \quad Q_{32} = \mu\lambda^{-2}, \quad Q_{33} = ik_1(p - \epsilon E_2^2\lambda^2), \quad Q_{34} = \epsilon E_2\lambda$$

$$Q_{41} = ik_1(3\epsilon E_2^2\lambda^2 - \mu\lambda^{-2} - p), \quad Q_{45} = 2\epsilon E_2\lambda, \quad Q_{46} = -1,$$

$$Q_{51} = -2ik_1\epsilon E_2\lambda, \quad Q_{55} = -\epsilon, \quad Q_{64} = 1. \qquad (193)$$
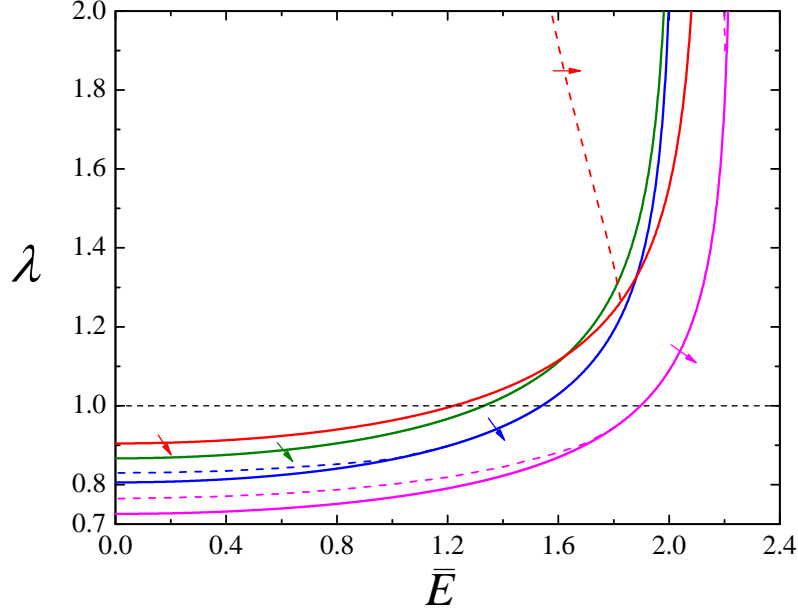
Fig. 22. The dependence of the critical stretch ratio on the electric field for layered composites with $\Theta = 0$. The volume fractions of the stiffer phase are $c^{(f)} = 0.05, 0.1, 0.2, 0.5$ (magenta, blue, green and red curves, respectively). The contrasts in the properties of the phases are $k = t = 10$. The continuous and dashed curves represent the onset of macroscopic and microscopic instabilities, respectively.

Furthermore, the analytical expression for the onset of macroscopic instabilities takes a compact form when $\Theta = 0$. Namely, the critical stretch ratio is

$$\lambda_c = \left(1 - \frac{\check{\mu}}{\bar{\mu}}\right)^{1/4} \left(1 - \bar{E}^2 \left(1 - \frac{\check{\epsilon}}{\bar{\epsilon}}\right) \frac{\check{\epsilon}}{\bar{\epsilon}}\right)^{-1/4}, \tag{194}$$

where

$$\bar{E} = E_2^0 \sqrt{\bar{\epsilon}/\bar{\mu}} \tag{195}$$

and

$$\bar{\mu} = c^{(m)}\mu^{(m)} + c^{(f)}\mu^{(f)}, \quad \check{\mu} = \left(\frac{c^{(m)}}{\mu^{(m)}} + \frac{c^{(f)}}{\mu^{(f)}}\right)^{-1} \quad \text{and} \quad \bar{\epsilon} = c^{(m)}\epsilon^{(m)} + c^{(f)}\epsilon^{(f)}. \tag{196}$$

It is easy to see from (194) that the composites become macroscopically unstable if subjected to an electric excitation higher than $\bar{E}_c$

$$\bar{E}_c = \frac{\bar{\epsilon}}{\sqrt{(\bar{\epsilon} - \check{\epsilon})\check{\epsilon}}}. \tag{197}$$

An example of the bifurcation diagrams is shown in Fig. (22) for composites with $\Theta = 0$ as functions of the critical stretch ratio λ and the referential electric field $\bar{E}$. The curves separate stable domains from those in which an instability may develop. The arrows indicate transitions from stable to unstable domains. The magenta, blue,

55

green and red curves correspond to $c^{(f)} = 0.05$, 0.1, 0.2 and 0.5, respectively. The stiffer to softer phase shear moduli ratio is $k = \mu^{(f)}/\mu^{(m)} = 10$ and the ratio between the dielectric constants is $t = \epsilon^{(f)}/\epsilon^{(m)} = 10$. The continuous and dashed curves represent the onset of macroscopic and microscopic instabilities, respectively.

For the macroscopic curves one can observe that an increase of the electric excitation extends the unstable domain whereas the pre-stretch stabilizes the composite. This continues until the corresponding critical value of the electric field (197) is achieved, beyond this value the composite becomes unstable regardless of the pre-stretch.

In a manner similar to the purely mechanical case, at low electric fields composites with low volume fractions of the stiffer phase ($c^{(f)} = 0.05$, 0.1) are more stable than those with moderate ones ($c^{(f)} = 0.2$, 0.5). However, when the electric field is increased, the curves intersect and instabilities in composites with lower $c^{(f)}$ may occur before those in composites with higher $c^{(f)}$. Specifically, at $\bar{E} = 1.95$ macroscopic instability occurs in a composite with $c^{(f)} = 0.1$ before it does in a composite with $c^{(f)} = 0.2$.

Interestingly, right before the intersection of the macroscopic curves, a curve corresponding to microscopic instability branches out from the curve for the macroscopic instability of the composite with higher $c^{(f)}$ such that practically the composite with higher volume fraction fails first, either at the macroscopic or at the microscopic level.

In composites with low volume fraction of the stiffer phase, there is a clear distinction between the onset of microscopic and macroscopic instabilities at low values of the applied electric field. In this limit, the microscopic instabilities that are associated with short waves appear long before the macroscopic ones. With the increase of the electric field the curves for microscopic and macroscopic instabilities near to the point where the macroscopic instabilities are the first to occur. However, the curves split again at high values of the electric excitation due to the appearance of microscopic instabilities before the macroscopic ones.

At moderate volume fractions of the stiffer phase, the onset of the microscopic instability coincides with the macroscopic one (see the example for $c^{(f)} = 0.2$). The curve for the microscopic instability branches from the curve of microscopic instability only at large values of the electric field.

A similar behavior is observed for composites with large volume fraction of the stiffer phase. However, the branching out of the curve for the microscopic instability occurs at lower values of the applied electric field. These branches of the instability curves reduce the stable domain and cut off the range of the pre-stretches at which the composite is stable. For example, for the composite with $c^{(f)} = 0.5$ subjected to $\bar{E} = 1.6$ the stable region of the stretch ratios is $1.1 < \lambda < 1.88$.

The dependence of the critical electric field on the dimensionless wave number $k_1 h$
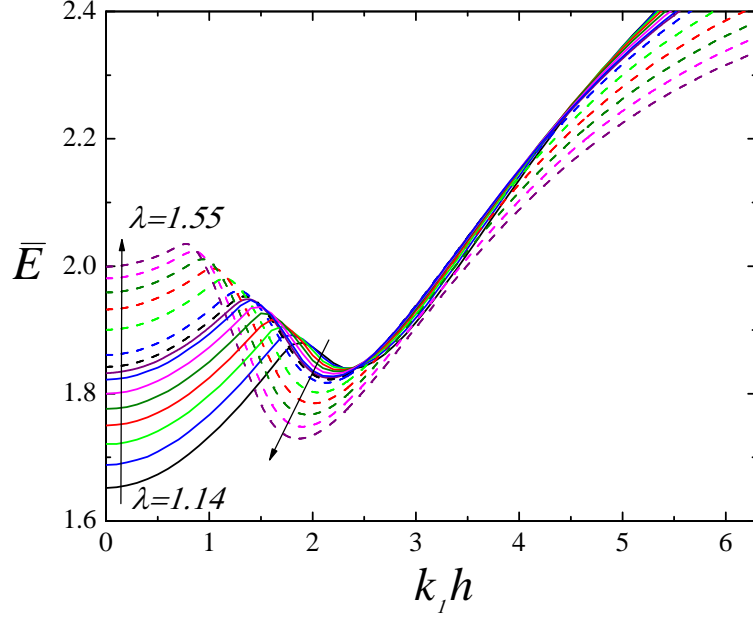
Fig. 23. The dependence of the critical electric field on the dimensionless wave number k_1h for composite with volume fraction of the stiffer phase $c^{(f)} = 0.5$. The contrasts in the properties of the phases are $k = t = 10$. The continuous curves correspond to those loading parameters for which the first instability occurs at $k_1h = 0$ whereas the dashed curves are for those parameters where the instability occurs at a finite wave length.

for composite with volume fraction of the stiffer phase $c^{(f)} = 0.5$ is demonstrated in Fig. (23). The contrasts in the properties of the phases are $k = t = 10$. Along each curve the pre-stretching is held constant. The arrows indicate the direction of larger stretch ratios. Before the branching out point of the curve for the microscopic instability in Fig. (22), the minimal values of the electric field appear at $k_1h \to 0$ corresponding to the macroscopic instabilities. An increase of the stretch ratio λ leads to a branching point at which minima of the corresponding curve in Fig. (23) are attained at two points, one $k_1h \to 0$ and a second at finite value of k_1h. This happens because as the pre-stretch is increased the critical electric field $\bar{E}$ at which the macroscopic instability occurs increases while the minimum at finite k_1h decreases. If one further increases the stretch ratio, the critical value of the wave number changes and the mode of instability shifts from macroscopic to a finite one.

The dependence of the critical stretch ratio on the electric field for the composites with contrasts in the phase properties $k = t = 50$ is shown in Fig. 24. The volume fractions of the stiffer phase are $c^{(f)} = 0.05$, 0.1, 0.2 and 0.5. Likewise the purely mechanical case (Triantafyllidis and Maker, 1985), an increase of the contrast of material
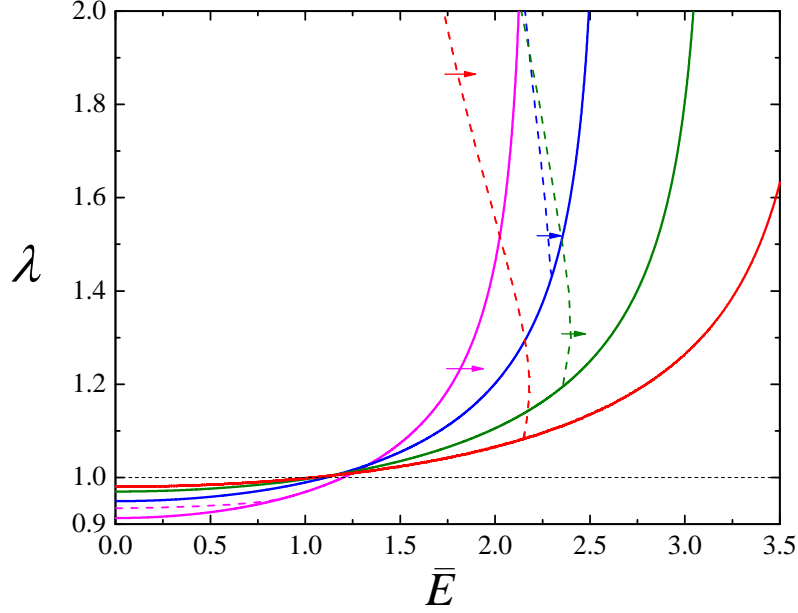
Fig. 24. Bifurcation diagrams of layered composites with contrasts in the phase properties $k = t = 50$ as functions of the critical stretch ratio and the referential electric field. The volume fractions of the stiffer phase $c^{(f)} = 0.05$, 0.1, 0.2 and 0.5 (magenta, blue, green and red curves, respectively). The continuous and dashed curves represent the onset of macroscopic and microscopic instabilities, respectively.

constants results in earlier onsets of instabilities. Differently from the case illustrated in Fig. 22 ($k = t = 10$), here the branching points of the curves corresponding for the microscopic instabilities appear even in composites with lower volume fractions ($c^{(f)} = 0.1$) and at lower values of electric excitation while the short-wave instabilities diminish. So that, the increase of the contrasts in the material properties restrains the short-wave instabilities (appearing at low vale of $c^{(f)}$) and provokes earlier development of the microscopic instabilities characterized by finite wavelengths, comparable with the microstructure size.

To complete the characterization of the composite stable domains, the projections of the bifurcation diagrams in coordinates of the electric field $\bar{E}$ and electric displacement $\bar{D} = D_2^0/\sqrt{\mu^{(m)}\epsilon^{(m)}}$ are given in Fig. 25(a) and (b). The corresponding average referential electric displacement and electric field are related via

$$\bar{\mathbf{D}}^0 = \bar{\epsilon}\bar{\mathbf{F}}^{-1}\bar{\mathbf{F}}^{-T}\bar{\mathbf{E}}^0 + (\check{\epsilon} - \bar{\epsilon})\bar{\mathbf{F}}^{-1}\bar{\mathbf{F}}^{-T}\hat{\mathbf{N}}\frac{\left(\bar{\mathbf{F}}^{-T}\bar{\mathbf{E}}^0\right) \cdot \left(\bar{\mathbf{F}}^{-T}\hat{\mathbf{N}}\right)}{\left(\bar{\mathbf{F}}^{-T}\hat{\mathbf{N}}\right) \cdot \left(\bar{\mathbf{F}}^{-T}\hat{\mathbf{N}}\right)}, \qquad (198)$$

which reduces to the expression $D_2^0 = \check{\epsilon}E_2^0\lambda^2$ reported in Bertoldi and Gei (2011) for the aligned case $\Theta = 0$.

To conclude the characterization of the stable domains I plot the bifurcation diagrams as functions of the applied electric field and the critical deviatoric mean stress

58

Fig. 25. Bifurcation diagrams of layered composites with volume fractions of the stiffer phase $c^{(f)} = 0.05$, 0.1, 0.2 and 0.5 (magenta, blue, green and red curves, respectively) as functions of the electric field $\bar{E}$ and electric displacement $\bar{D}$. The continuous and dashed curves represent the onset of macroscopic and microscopic instabilities, respectively.
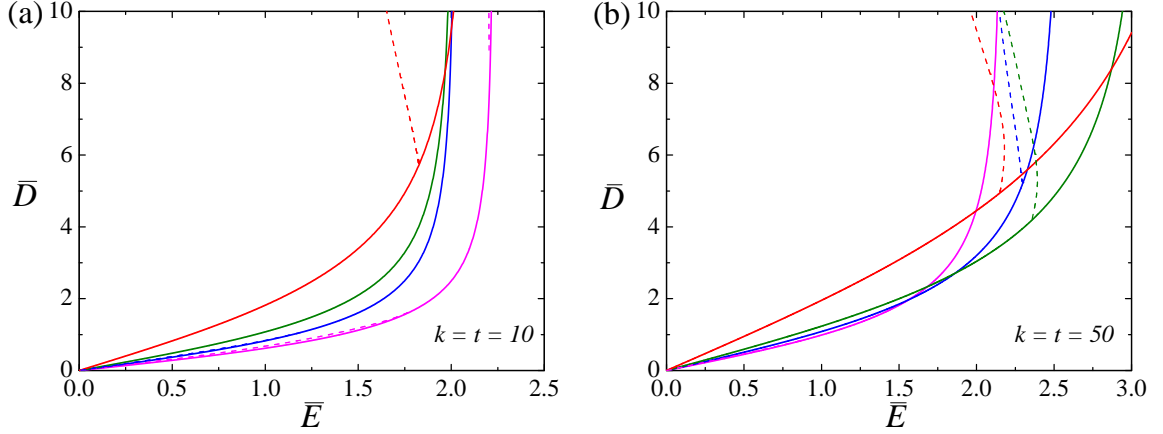
along the layers. These are shown in Fig. 26 for the same contrasts between the phase properties, namely $k = t = 10$ in (a) and $k = t = 50$ in (b). Here, the mean deviatoric stress is related to the stretch ratio and the electric field via

$$\bar{\sigma}^D = \frac{1}{3}\left(\left(2 - \frac{\check{\epsilon}}{\bar{\mu}}\bar{E}^2\right)\lambda^2 - 1 - \lambda^{-2}\right). \tag{199}$$

As anticipated on physical grounds, one can observe that the critical macroscopic longitudinal stress is negative for relatively low applied electric fields. However, an increase of the electric field impacts differently the critical mean stress depending on the material morphology. In particular, for composites with higher contrasts in the properties of the phases the critical stress increases (see Fig. 26(b)), while for composites with lower contrasts the critical stress decreases when the volume fraction of the stiffer phase is low ($c^{(f)} = 0.05$ and 0.1 in Fig. 26(a)) and increases when $c^{(f)}$ is high ($c^{(f)} = 0.2$ and 0.5 in Fig. 26(a)).

Consider the evolution of the stresses in the phases of the material along the equilibrium path of a fixed pre-stretched configuration $\lambda = 2$. Shown in Fig. 27 are the functions of the longitudinal deviatoric stresses in the phases and the applied electric field. The red and blue curves correspond to the stresses in the stiffer and softer phases, respectively, while the mean stresses are represented by the black curves. The dotted, continuous and dashed curves correspond to the stresses along the equilibrium path, and to the onset of macroscopic and microscopic instabilities, respectively. Along the equilibrium path the stresses in the phases are positive at the initial pre-stretch configuration where $\bar{E} = 0$, and an increase of the applied electric field leads to a decrease of the stresses in the phases. Because of the different electric fields in the phases the stress
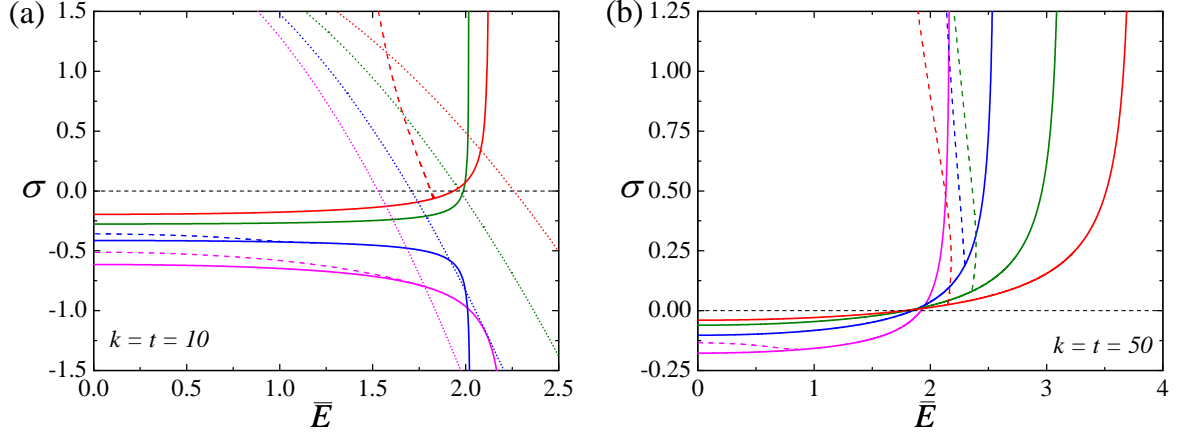
Fig. 26. Bifurcation diagrams of layered composites with volume fractions of the stiffer phase $c^{(f)} = 0.05$, 0.1, 0.2 and 0.5 (magenta, blue, green and red curves, respectively) as functions of the longitudinal mean stress and the referential electric field. The continuous and dashed curves represent the onset of macroscopic and microscopic instabilities, respectively.

in the soft phase decreases faster and becomes negative. The difference in the deviatoric longitudinal stresses increases as the electric field is increased and the equilibrium curves intersect with the corresponding bifurcation curves.

The morphology significantly impacts the composite stability, restraining or promoting different instability modes. To highlight this effect bifurcation diagrams are presented as functions of the critical stretch ratio and the volume fraction of the stiffer phase in Fig. 28. The failure surfaces are shown for composites with contrast ratios $k = t = 10$ subjected to different electrical excitations $\bar{E} = 1.0$, 1.6, 1.8 and 2.0 (red, green, magenta and blue curves, respectively). The continuous and dashed curves correspond to the onset of macroscopic and microscopic instabilities, respectively.

One can observe that for each unstable domain corresponding to a particular electric excitation three subdomains can be distinguished. The first corresponds to the one where macroscopic instabilities ($k_1 h \to 0$) are identified. This macroscopically unstable domain lies beneath the continuous curves. The domain increases with the increase of the applied electric field. The second domain corresponds to a small zone at low volume fractions of the stiffer phase, between the dashed and the continuous curves. Here, instabilities associated with short waves ($k_1 h \to 2\pi$) appear. Differently from the first domain, this one decreases with the increase of the electric excitation. So that the applied electric field restrains the short-wave instabilities and stimulates the long-waves instabilities. The above subdomains were observed for the purely mechanical case by Triantafyllidis and Maker (1985). The peculiar third domain was not revealed in the purely mechanical case. The characteristic scale of these instabilities is demonstrated in
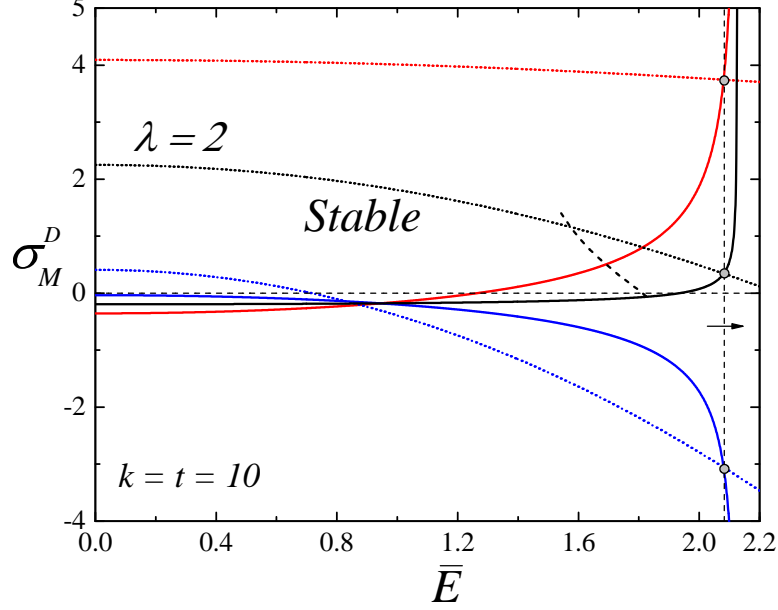
Fig. 27. The longitudinal stresses as functions of applied electric field of layered composites with volume fraction of the stiffer phase $c^{(f)} = 0.5$. The dotted, continuous and dashed curves correspond to the stresses along the equilibrium path $\lambda = 2$, onset of macroscopic and microscopic instabilities, respectively. The red curves represent the stresses in the stiffer phase and the blue ones correspond to the stresses in the softer phase. The black curves represent the mean stresses.

Fig. 23 and it appears to be $k_1 h \sim 2$. This domain is associated with high volume fraction of the stiffer phase and large pre-stretches. When the electric excitation increases the domain expands to include composites with moderate volume fractions at lower levels of the stretch ratio. As the first and third domains expand towards each other as the electric excitation increases, at some value of $\bar{E}$ they intersect. In the figure, I show the distinguishing between them with the aid of the dotted curves.

It was shown by Geymonat et al. (1993) for the purely mechanical case that the long-wave instabilities can be estimated from the loss of strong ellipticity of the corresponding media. Furthermore, the macroscopic instability is an upper bound of the microscopic instabilities. For the fully coupled electromechanical problem, I always observe this phenomenon during calculation of the numerical examples (see, for example, Fig. 23). The numerical results of Bertoldi and Gei (2011) for the aligned composites with some specific volume fractions are also in agreement with those findings. In addition, I observe that for the media with moderate volume fractions of the stiffer phase the macroscopic instability can be used as a good estimate for the material failure.

Consider the influence of lamination angle Θ on the onset of instabilities. Noting that at the lamination angles different from $\Theta = 0$ and $\pi/2$ the microscopic instability analysis becomes rather complicated and for the non-aligned loading cases I consider
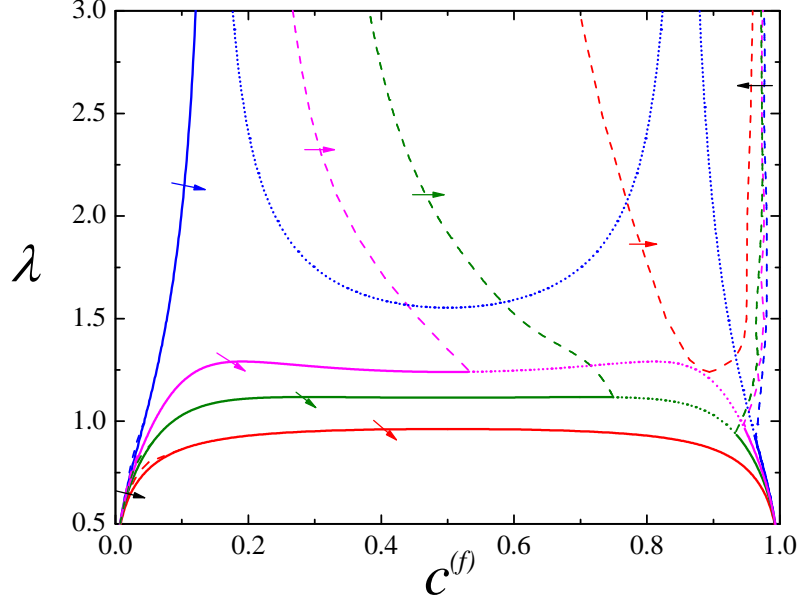
Fig. 28. The failure surfaces of layered composites as functions of the critical stretch ratio and volume fraction of the stiffer phase. The contrasts in the properties of the phases are $k = t = 10$. The red, green, magenta and blue curves correspond to $\bar{E} = 1.0$, 1.6, 1.8 and 2.0, respectively. The continuous and dashed curves correspond to the onset of the macroscopic and microscopic instabilities, respectively. The dotted curves separate the unified unstable domains according to the instability mode associated with each part.

only the onset of *macroscopic* instabilities.

The bifurcation diagrams are presented in Fig. 29 as functions of the critical stretch ratio and the volume fraction of the stiffer phase for composites with different lamination angles $\Theta = 0$, $\pi/16$, $\pi/8$ (blue, red and green continuous curves, respectively). The composites are subjected to electric excitation $\bar{E} = 1.0$ in Fig. 29(a) and $\bar{E} = 2.0$ in Fig. 29(b). In a manner reminiscent of the purely mechanical case (Triantafyllidis and Maker, 1985), the macroscopic failure surfaces are symmetric with respect to $c^{(f)} = 0.5$ and the composites are less stable in the range of moderate volume fraction of the stiffer phase. Composites with volume fractions near $c^{(f)} \sim 0$ and 1 become stable. This effect is intensified with an increase of the lamination angle, once again in a manner similar to the one observed in laminated composites under mechanical loads (Nestorovic and Triantafyllidis, 2004; Agoras et al., 2009a). An increase of the electric excitation results in earlier onset of the macroscopic instability.

The picture alters drastically when the value of the electric field approaches $\bar{E}$ given in Eq. (197). In contrast to the findings in Fig. 29(a), one can observe in Fig. 29(b) that the composites with volume fractions of the stiffer phase in the vicinity of $c^{(f)} \sim 0.144$ and 0.856 become extremely unstable.

To highlight the transition of the composites behavior as the intensity of the electric
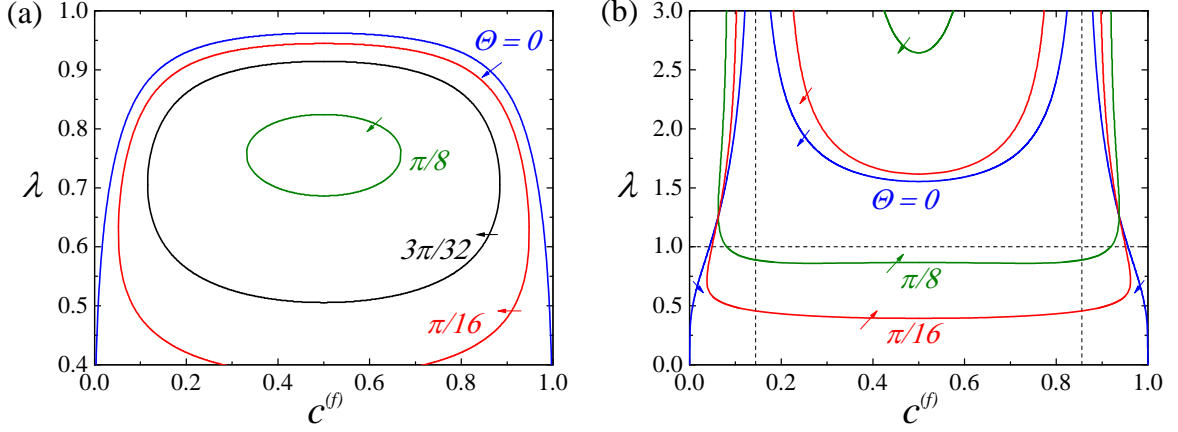
Fig. 29. The macroscopic failure surfaces of layered composites as functions of the stretch ratio and the volume fraction of the stiffer phase. The contrasts in the properties of the phases are $k = t = 10$. (a) - $\bar{E} = 1.0$; (b) - $\bar{E} = 2.0$

field approaches the critical value of the applied electric field, the bifurcation diagrams of composites with aligned layers ($\Theta = 0$) are presented in Fig. 30 for $\bar{E} = 1.9$, 1.925, 1.95, 1.975, 2.0 and 2.025 (blue, red, black, green, magenta and purple curves, respectively). Thus, in contrast to the purely mechanical case where the most macroscopically unstable morphology corresponds to $c^{(f)} = 0.5$, in the electromechanical case the composite behavior changes and the least stable volume fraction shifts. Remarkably, the results of the numerical simulations hint that the dramatic change of the macroscopic curves behavior may be associated with the unifying of the first and third unstable domains in Fig. 28. At this stage, the media become unstable in a large range of $c^{(f)}$ (see Fig. 28).

One can observe that macroscopically, the effect of the lamination angle on the composite stability varies from stabilization at low values of the electric fields to opposite influence at high electric excitations. However, this trend might be different when microscopic instabilities of shorter wave lengths are considered. Therefore, in following examples I consider composites with volume fraction of the stiffer phase $c^{(f)} = 0.2$ since the macroscopic failure mode dominates at this morphology even at relatively high electrostatic excitations.

Shown in Fig. 31 are the bifurcation diagrams for composites with $c^{(f)} = 0.2$. The bifurcation diagrams are presented as functions of the critical stretch ratio λ and the referential electric field $\bar{E}$. The contrasts in the properties of the phases are $k = t = 10$. The lamination angles in the ranges $0 \leq \Theta \leq \pi/4$ and $\pi/4 < \Theta \leq \pi/2$ are presented in Figs 31(a) and (b), respectively. The continuous curves correspond to the macroscopic failure surfaces and the blue dashed curve in Fig. 31(a) represents the onset of the microscopic instability for the aligned case ($\Theta = 0$).

63
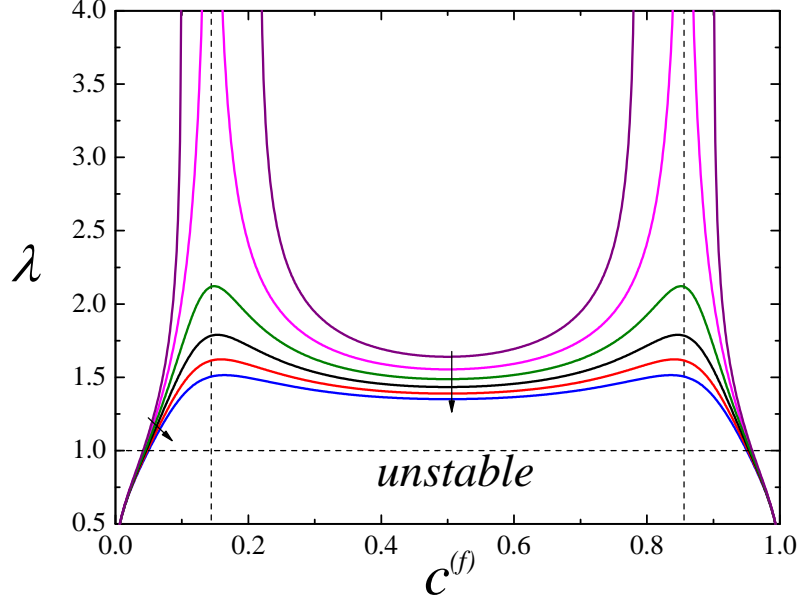
Fig. 30. Failure surfaces of layered composites with $\Theta = 0$ as functions of the stretch ratio and volume fraction of the stiffer phase. The contrasts in the properties of the phases are $k = t = 10$. The blue, red, black, green, magenta and purple curves correspond to $\bar{E} = 1.9, 1.925, 1.95, 1.975, 2.0$ and 2.025, respectively.

The corresponding expression for the critical stretch ratio takes a compact form when $\Theta = \pi/2$

$$\lambda_c = \left(1 - \frac{\check{\mu}}{\bar{\mu}} - \bar{E}^2\Big(1 - \frac{\check{\epsilon}}{\bar{\epsilon}}\Big)\right)^{-1/4}. \tag{200}$$

In contrast to the aligned case ($\Theta = 0$), here an increase of the applied electric field stabilizes the media. It is easy to see from (200) that whenever the applied electric field exceeds the value

$$\bar{E}_c = \sqrt{\frac{(\bar{\mu} - \check{\mu})\bar{\epsilon}}{(\bar{\epsilon} - \check{\epsilon})\bar{\mu}}}, \tag{201}$$

the composite becomes macroscopically stable. For the composite with identical shear to dielectric constants ratio of the phases $r^{(f)} = \mu^{(f)}/\epsilon^{(f)} = r^{(m)} = \mu^{(m)}/\epsilon^{(m)} = r$, this value of the electric field is $E_2^{0\,(c)} = \sqrt{r}$ which corresponds to $\bar{E}_c = 1$ (thin dashed line in Fig. 31(b)).

In the pure mechanical case, the composites loose the stability only when the layers are compressed in the lamination direction. If the composite is laminated at an angle higher than a critical one, any applied compression will never lead to failure, since the layers switch from compression to tension being rotated at angle $\pi/4$ in the deformed configuration (Rudykh and deBotton, 2012). However, in the coupled electromechanical case, when the electrostatic excitation is high enough even these composites may become unstable. For instance, the composites with $\Theta = \pi/8$ and $\Theta = \pi/4$ are represented in
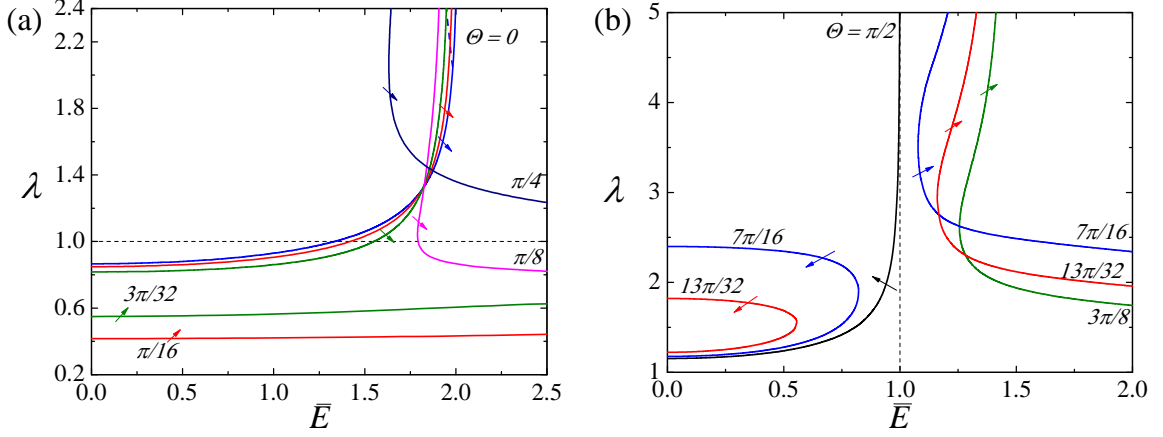
Fig. 31. The bifurcation diagrams of layered composites with different lamination angles as function of the critical stretch ratio and the referential electric field. The volume fraction of the stiffer phase is $c^{(f)} = 0.2$ and the contrasts in the properties of the phases are $k = t = 10$. (a) - small angles; (b) - large angles

Fig. (31) by the pink and purple curves, respectively. While in the pure mechanical case, the failure surfaces possess the property $\lambda(\Theta) = 1/\lambda(\Theta + \pi/2)$, the failure surfaces of the coupled problem do not.

In the limiting cases $\Theta = 0$ and $\Theta = \pi/2$ I note the different role of the electric field, which is to stimulate instabilities in the first case while stabilizing in the second. The behaviors of composites with intermediate angles of lamination are associated with transition between the limiting cases (from $\Theta = 0$ to $\Theta = \pi/2$) as the role of the electric field is concerned. Obviously, at some lamination angle in the deformed configuration the role of the electric field switches.

This is illustrated in Fig. (32) as a conclusive example for the composite with similar to the previously considered material properties and volume fraction of the stiffer phase. The diagrams show the dependence of the critical stretch ratio on the lamination angle. The black, bright green, orange, green, magenta, blue and red curves correspond to applied electric excitations $\bar{E} = 0.0, 0.5, 1.0, 1.5, 1.8, 1.9$ and 2.0, respectively. The bifurcation diagrams are symmetric with respect to 0 and $\pi/2$ and periodic in π. In agreement with the previous discussion, at low lamination angles the electric field promotes instabilities, whereas at the lamination angles close to $\pi/2$ the applied electric field stabilizes the composites. Due to this stabilization effect in composites with lamination angles close to $\pi/2$, instabilities may occur only under relatively low electric fields ($\bar{E} < 1$). One can observe that for moderate levels of the electric field (e.g., $\bar{E} = 1.5$ and $\bar{E} = 1.8$) there are two disjoint unstable domains. The first contains the aligned composite ($\Theta = 0$) and the other includes composites with larger lamination angles at large critical stretch ratios. Composites with lamination angles between these

65
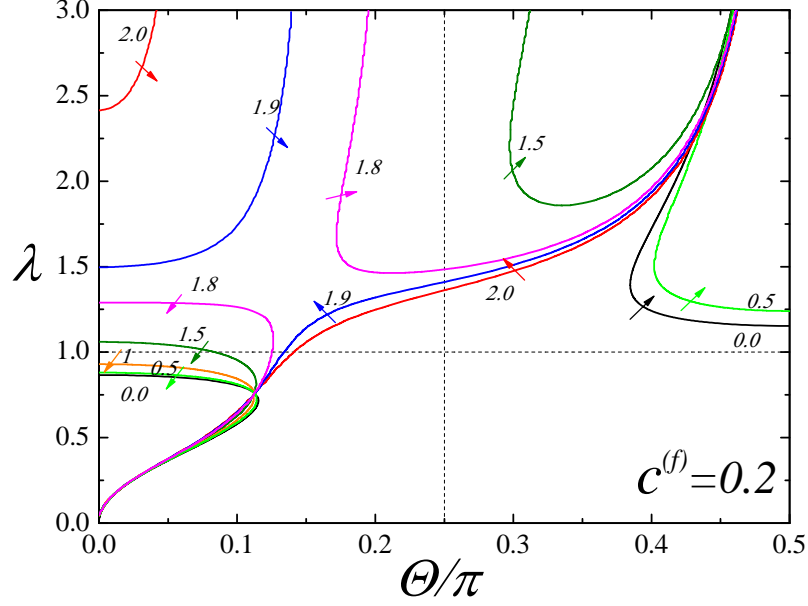
Fig. 32. Bifurcation diagrams as functions of the stretch ratio and lamination angle. The contrasts in properties of the phases are $k = t = 10$.

two domains are stable materials at these levels of excitations (e.g., composites with $0.11\pi < \Theta < 0.3\pi$ for $\bar{E} = 1.5$). With increase of the electric field the unstable domains near one to another. That continues up to a certain value of the electric field is achieved at which the two domains unite (e.g., the transition from $\bar{E} = 1.8$ to $\bar{E} = 1.9$). Beyond this value of the electric field the only stable morphology is the one with $\Theta = \pi/2$. Remarkably, the value of the electric field at which the domains unite corresponds to the situation where the influence of lamination angles switches from stabilization to the opposite one.

Note that for the composites with isotropic phases in the cases $\Theta = n\pi$, $\pi/2 + n\pi$, where $n = 0, 1, 2...$, coefficients Γ_1, Γ_3, Γ_5 vanish in the polynomial equation (170) and the condition for ellipticity loss can be written in terms of the bi-cubic polynomial

$$\Gamma_6\xi^6 + \Gamma_4\xi^4 + \Gamma_2\xi^2 + \Gamma_0 = 0. \tag{202}$$

Analogous results in terms of the nominal electric displacement instead of the referential electric field, were reported by Dorfmann and Ogden (2010) for surface instabilities in half space isotropic dielectrics and by Bertoldi and Gei (2011) for long wave instabilities in layered composites with isotropic phases and lamination angle $\Theta = 0$.

66

4.3 Concluding Remarks

A systematic study of the multiscale instabilities in soft composite dielectrics was conducted in terms of physically relevant variables. First, a *general criterion* for onset of instabilities associated with long waves was introduced. Second, a condition for the onset of microscopic instability was introduced for the layered composites with *anisotropic* phases. Third, a closed form expression for energy-density function of these media is deduced. This allowed us to detect that whenever the medium fails it occurs in one of the three unstable domains depending on the composite morphology and electromechanical loadings

(i) *long-wave* instabilities dominate at moderate volume fractions of the stiffer phase

(ii) *interface instabilities* appear at low volume fractions of the stiffer phase

(iii) *instabilities of microstructure characteristic scales* occur at high volume fractions of the stiffer phase

An increase of electric field suppresses the (ii)-type of instabilities and promotes the (i)- and (iii)- types. Thus, the unstable domains of the long and finite waves unite and create a new unstable domain. At this point the composite becomes extremely unstable at a large variety of its morphologies. This critical point can be detected by a more compact analysis of macroscopic instabilities only. Whenever the macroscopic failure surfaces alters drastically in the illustrated way, the critical situation is achieved. These can be strictly determined from the *closed form expressions* for critical values of the pre-stretch depending on the applied electric fields. Thanks to these analytical expressions the critical values of the electric fields are revealed

1. composites with lamination angle $\Theta = 0$ lose the stability whenever electric excitation exceeds the value given in (197)

2. composites with lamination angle $\Theta = \pi/2$ become macroscopically stable whenever electric excitation exceeds the value given in (201)

Based on the macroscopic analysis it is found that at low values of the electric field an increase of lamination angles stabilizes the media and has an opposite effect at high electric fields. The transition between these opposite influences occurs when two macroscopically unstable domains meet and unite.

Chapter 5

Thick-Wall EAP Balloon

A major limitation of EAP originates in the need for relatively large electric fields. However, usage of instability phenomena (Mockensturm and Goulbourne, 2006; Dorfmann and Ogden, 2010) may reduce the intensity of the required electric field. Accordingly, I analyze the response of EAP balloons and demonstrate that a relatively small electrostatic field can be used as a trigger for large deformations. I follow the theory of nonlinear electroelasticity by Toupin (1956); McMeeking and Landis (2005), where the total stress is

$$\sigma_{ij}^{(t)} = \sigma_{ij}^{(c)} + \sigma_{ij}^{(m)}. \tag{203}$$

Here, $\sigma_{ij}^{(c)}$ is the Cauchy *mechanical* stress, $\sigma_{ij}^{(m)} = \epsilon\epsilon_0 E_i E_j - \frac{\epsilon_0}{2} E_n E_n \delta_{ij}$ is the Maxwell stress induced by the electric field E, ϵ is a dielectric modulus, and ϵ_0 is the vacuum permittivity. Assume that $\epsilon = 6$, which is typical for common polymers, is constant. I adopt a quite general constitutive law for *incompressible isotropic* materials, in which the principal stresses are

$$\sigma_k^{(c)} = \sum_{p=1}^{N} \mu_p \lambda_k^{\alpha_p} - q, \tag{204}$$

where λ_k are the principal stretches, q is an arbitrary hydrostatic pressure, μ_p are shear moduli, and α_p are material constants. In the case $N = 1$ with $\alpha_1 = 2$, the model (204) which is commonly denoted Ogden model, reduces to the neo-Hookean one. With $N = 3$ an excellent correlation with experimental data for elastomers is revealed (Treloar, 1975). Accordingly, I assume the following typical values for the elastic constants of soft polymers (Treloar, 1975) $\mu_1 = 6.3 \cdot 10^5$Pa, $\mu_2 = 1.2 \cdot 10^3$Pa, $\mu_3 = -1 \cdot 10^4$Pa, $\alpha_1 = 1.3$, $\alpha_2 = 5$, and $\alpha_3 = -2$. In the vicinity of the reference configuration this polymer behaves like a neo-Hookean material with shear modulus $\mu = \frac{1}{2}\sum_{p=1}^{3}\mu_p\alpha_p = 4.225 \cdot 10^5$Pa.

Consider a spherical balloon made out of a dielectric elastomer with inner R_i and outer R_o radii. Here and thereafter, the notations $(\bullet)_i$ and $(\bullet)_o$ are used to specify quantities at the inner and outer radii, respectively. The thickness of the balloon wall is $H = R_o - R_i$. The inner and outer surfaces of the balloon wall are covered with thin electrodes with negligible elastic modulus (Bhattacharya et al., 2001) that enable to induce an electric field across the wall. The balloon can be inflated with inner pressure
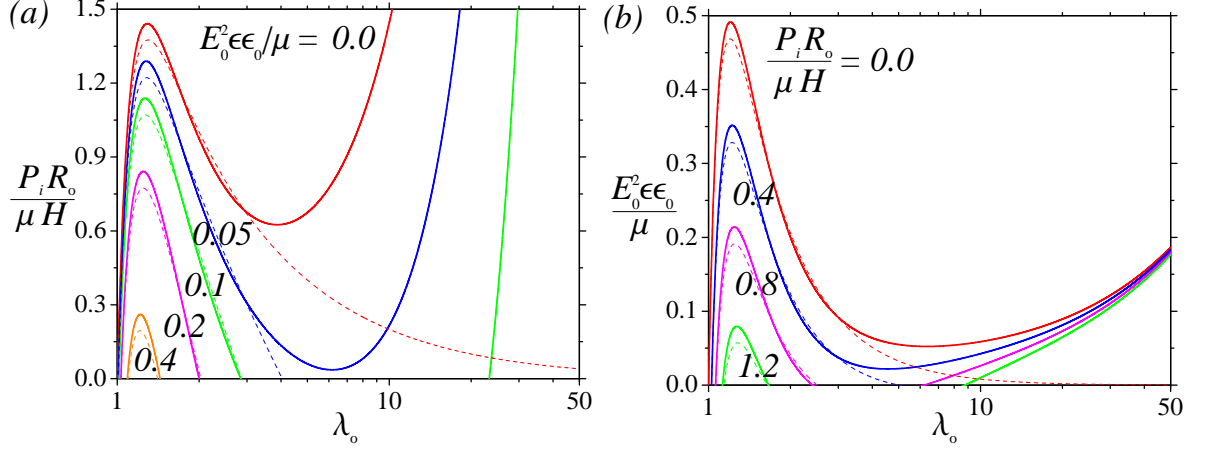
Fig. 33. Deformation of a thick-wall balloon due to (a) inflation pressure and (b) electrostatic excitation. The continuous and dashed curves correspond to Ogden and neo-Hookean materials, respectively.

P_i, and electrically exited with electric potential φ_o between the two electrodes. The associated boundary conditions are

$$\sigma_{rr}^{(t)}(r_i) = -P_i, \ \sigma_{rr}^{(t)}(r_o) = 0, \ \varphi(r_i) = 0, \ \varphi(r_o) = \varphi_o, \tag{205}$$

where r is the radius in the deformed configuration.

In a spherical coordinate system the principal stretch ratios are

$$\lambda_r = \frac{\mathrm{d}r}{\mathrm{d}R} = \lambda^{-2}, \quad \lambda_\theta = \lambda_\phi = \frac{r}{R} = \lambda, \tag{206}$$

where $\lambda(R) = (1 + (R_o/R)^3(\lambda_o^3 - 1))^{1/3}$. Maxwell equations reduce to Laplace equation for the electrical potential φ, which is solved in the deformed configuration. The components of the electric field $E \equiv -\nabla\varphi$ satisfying the electrostatic boundary conditions in (205) are

$$E_r = \frac{\varphi_o r_o r_i}{r_i - r_o} \frac{1}{r^2}, \ E_\theta = E_\phi = 0. \tag{207}$$

The solution of the equilibrium equation

$$\frac{\mathrm{d}}{\mathrm{d}r}\sigma_{rr}^{(t)} = -\frac{2}{r}\left(\sigma_{rr}^{(t)} - \sigma_{\theta\theta}^{(t)}\right), \tag{208}$$

with boundary conditions (205) and relations (203), (204) and (206) reads

$$P_i = \sum_{p=1}^{N}\frac{2\mu_p}{3}\left\{\mathrm{B}\left[\lambda_i^{-3}, \lambda_o^{-3}, 1 - \frac{\alpha_p}{3}\right] + \mathrm{B}\left[\lambda_o^{-3}, \lambda_i^{-3}, 1 + \frac{2\alpha_p}{3}\right]\right\}$$
$$+ \frac{1}{2t^2}\frac{(t-1)^2}{\lambda_i^2\lambda_o^2}\frac{t^4\lambda_i^4 - \lambda_o^4}{(t\lambda_i - \lambda_o)^2}\epsilon\epsilon_0 E_0^2, \tag{209}$$

where $\mathrm{B}\left[z_0, z_1, a\right] = \int_{z_0}^{z_1} x^{a-1}(1-x)^{-1}\mathrm{d}x$ is the generalized incomplete Beta function, $t = R_i/R_o$, and $E_0 = \varphi_o/H$ is a referential electric field.

69
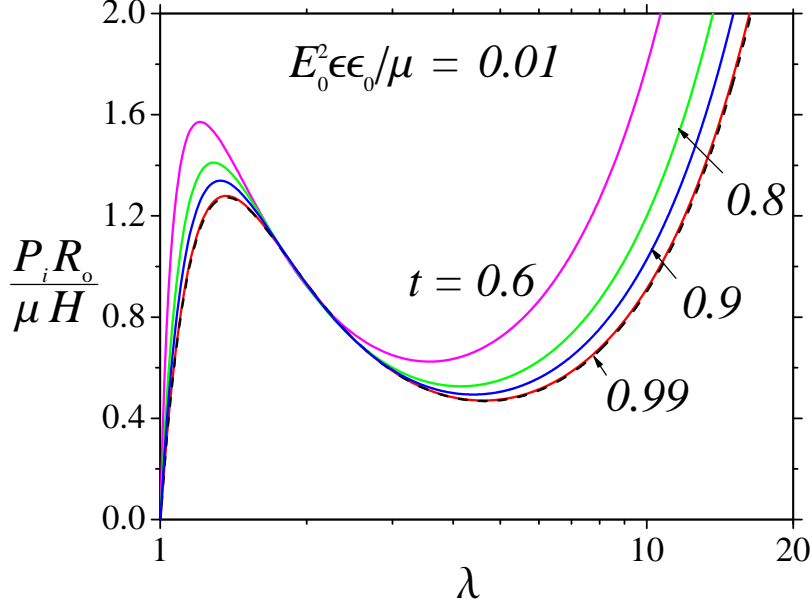
Fig. 34. The deformations of balloons with different wall thicknesses as functions of the pressure with fixed electric excitation. The dashed curve corresponds to the thin-wall approximation (210).

Results for a thick-wall balloon ($t = 0.8$) are presented in Fig. 33. Shown in Fig. 33a is the inflation pressure versus the stretch ratio for a few fixed electric fields. Fig. 33b shows the electric field versus the stretch ratio for a few values of the inflation pressure. The results for the Ogden and the neo-Hookean materials are denoted by continuous and dashed curves, respectively.

With the increase of the inflation pressure the balloon slowly expands until a critical pressure is reached. Further increase in the pressure leads to a sudden jump in the size of the balloon to a new stable state. This phenomenon is commonly denoted "snap-through". Application of electric field reduces the critical pressure at which the balloon snaps. One can observe that this effect cannot be recovered with the neo-Hookean material (Zhu et al., 2010). Similarly, electrostatic excitation which is applied in the undeformed configuration leads to expansion of the balloon up to a critical electric field. Further increase in the electric potential results in a snap-through of the balloon. When applied to a pre-inflated balloon, the critical electric field at which the instability occurs decreases. Note that after instability occurs, the slopes of the curves decrease. This implies that once the balloon snaps to its new state, smaller variations in the electric field result in larger actuations.

For thin-wall spheres (Mockensturm and Goulbourne, 2006) Eq. (209) can be simplified to

$$P_i = \frac{2H}{R} \left(\sum_{p=1}^{N} \mu_p \left(\lambda^{\alpha_p - 3} - \lambda^{-2\alpha_p - 3} \right) - \epsilon_0 \epsilon E_0^2 \lambda \right). \tag{210}$$

70
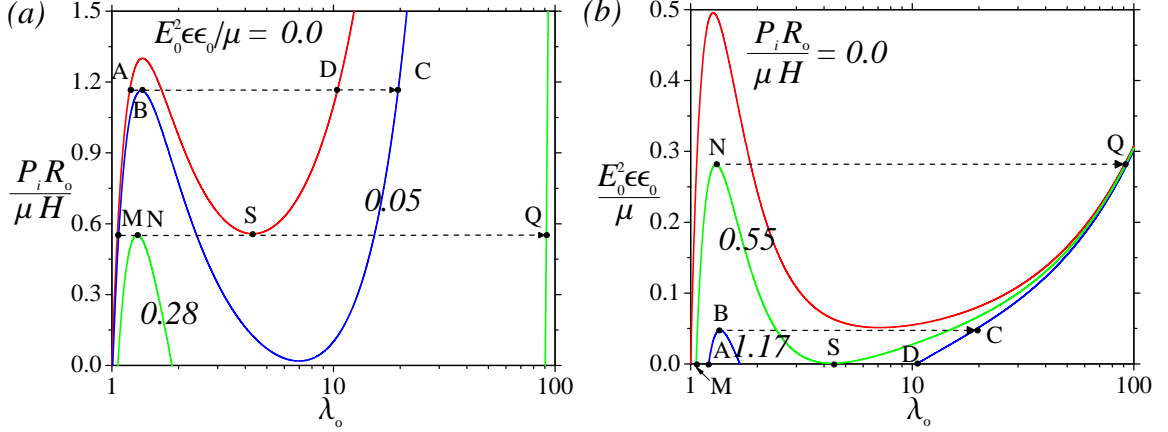
Fig. 35. Actuation cycles of a dielectric balloon subjected to (a) inflation pressure and (b) electrostatic excitation.

With $N = 1$ and $\alpha_1 = 2$, Eq. (210) further reduces to the case of a thin-wall neo-Hookean sphere (Zhu et al., 2010). In Fig. 34 a comparison of solution (209) with approximation (210) is carried out for different thickness ratios. Note that Eq. (210) provides a fair estimate for $t > 0.9$. However, for micro-actuators with a diameter of a few tenth of micrometers this approximation will lead to considerable errors.

I consider next two snap-through cycles in which the inner pressure is fixed and the actuation is electrically controlled. To this end I show in Fig. 35 the deformation of a thin-wall balloon ($t = 0.99$) as a function of (a) the inflation pressure and (b) the electrostatic excitation.

The first actuation cycle is "irreversible", and once the balloon deforms, it remains in a deformed state even after removal of the electric field. This cycle is represented by the path A-B-C-D. Initially, the balloon is inflated, with $\varphi_o = 0$, to point A. Application of a relatively low electric field will result in expansion to point B, where the balloon snaps to a stable state at point C. Upon removal of the electrostatic field, the balloon shrinks to point D that corresponds to a stable configuration under zero electric excitation.

The second actuation cycle is "reversible" in the sense that upon removal of the electric excitation the balloon returns to the original configuration. This cycle corresponds to the path M-N-Q-S. As before, the balloon is initially inflated with $\varphi_o = 0$, to point M. Application of an electric field results in gradual inflation to point N, followed by abrupt expansion to point Q. Removal of the electric potential will result in shrinking of the balloon to point S, followed by a jump back to point M.

Lastly, in Fig. 36 I examine the usage of the dielectric balloon as a micro-pump. Consider a balloon with inlet and outlet unidirectional valves. When the balloon expands at a pressure lower than a specific negative threshold pressure P_1 the inlet valve
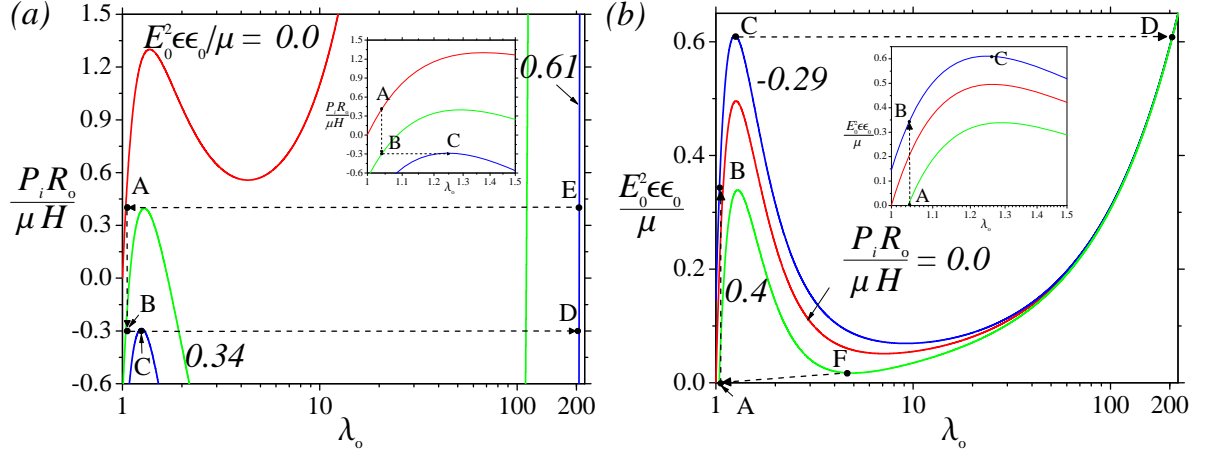
Fig. 36. Pumping cycle of a dielectric balloon subjected to (a) inflation pressure and (b) electrostatic excitation.

opens and allows liquid to flow into the balloon. When the balloon shrinks, at some positive threshold pressure P_2 the outlet valve opens and liquid flows out. In a way of an example, in Fig. 36 the normalized pressures are $P_1 = -0.29$ and $P_2 = 0.4$. The pumping cycle starts at point A at which the internal pressure is slightly lower than P_2. Once the balloon is excited, due to the electrostatic forces that act to shrink its wall, the internal pressure drops to P_1 at constant λ (since the balloon cannot deform as long as both valves are close). At this point the inlet valve opens, and the balloon expands while liquid flows in (segment B-C). At point C, due to the instability, the balloon further expands to point D. This is a stable point at which the inlet valve closes, terminating the sucking stage. As the electric excitation is removed, due to the elasticity of the balloon the inner pressure increases as long as the pressure is lower than P_2 (segment D-E). At point E the pressure reaches P_2, the outlet valve opens and liquid flows out of the balloon as it starts to shrink. This process continues till the balloon returns back to point A through point F.

Conclusions

This thesis concerns multiscale instabilities in electroactive composites undergoing finite deformations. First, large scale or macroscopic instabilities were considered. In the context of the purely mechanical problem, the onset of macroscopic instability is detected when the governing incremental equations loose the ellipticity and bifurcations of the solution occur. This idea together with the implementation of the micromechanical approach to composites with random distribution of aligned fibers, resulted in a closed form compact expression for the critical stretch ratio of composites with *neo-Hookean* and *Gent* constituents. These analytical findings were fairly compared with the 3-D FE simulations for which an instability analysis algorithm was developed in the framework of finite deformation elasticity.

A *general criterion* for the onset of macroscopic electromechanical instabilities was derived. This can be utilized for identification of the instability onset even in *multiphase* composites. Since possible application of electroactive materials are controlled by the applied voltage, an approach involving the referential electric field as a primary variable was adopted. Furthermore, a similar electromechanical instability criterion was derived in terms of the referential electric displacement as a primary variable. By application of the criterion to a class of layered anisotropic materials for which an exact analytical solution was derived, the unstable domains were revealed. It was found that the electric excitation promotes instabilities if applied perpendicular to the layers. If the electric excitation is parallel to the layers the composite is stabilized. Generally, an increase of the pre-stretch in the layers direction stabilizes the media. Remarkably, when the physically relevant approach of the referential electric field as a primary variable is utilized important stability properties are recovered, most of them cannot be predicted by the convenient formulation in terms of the electric displacement. For instance, there are electric fields beyond which the composites become unstable regardless of the pre-stretch, whereas for every value of the applied electric displacement there exists a pre-stretch for which the composite remains stable. Depending on the contrast between the phase properties, extremely unstable morphologies can be found. Once again, these cannot be detected when analysis in terms of the electric displacement is adopted.

The core of the work is the analysis of electromechanical microscopic instabilities. A condition for the onset of microscopic instabilities was derived by application of Bloch-Floquet technique to periodic layered structure with general *anisotropic* phases.

This allowed to detect that whenever the layered medium fails, it occurs in one of the three unstable domains depending on the composite morphology and electromechanical loadings

(i) *long-wave* instabilities dominate at moderate volume fractions of the stiffer phase

(ii) *interface instabilities* appear at low volume fractions of the stiffer phase

(iii) *instabilities of microstructure characteristic scales* occur at high volume fractions of the stiffer phase

The results for the first mode of instabilities agree with the ones obtained from the general criterion for the macroscopic instabilities. Whereas the first and second modes of instabilities were detected in the purely mechanical case, the third mode is unique and appears only in the coupled case. These domains evolve with changes in the applied electric field such that the overall unstable domain increases when the electric field is increased.

Finally, a possible application of the instability phenomenon in thick wall spherical balloon was examined. To this end an exact analytical solution was derived and actuation mechanisms for micro-pumps were proposed.

Appendix A

Kinematic tensors of the TI invariants

The explicit expressions for the kinematic tensors of the physically motivated invariants are

$$\frac{\partial \lambda_n^2}{\partial \mathbf{F}} = 2\mathbf{F}\hat{\mathbf{N}} \otimes \hat{\mathbf{N}}, \tag{A.1}$$

$$\frac{\partial \lambda_p^2}{\partial \mathbf{F}} = \lambda_p^2 \mathbf{F}^{-T} - \frac{\lambda_p^2}{\lambda_n^2}\mathbf{F}\hat{\mathbf{N}} \otimes \hat{\mathbf{N}}, \tag{A.2}$$

$$\frac{\partial \gamma_n^2}{\partial \mathbf{F}} = \frac{2}{\lambda_n^2}(\mathbf{F}\hat{\mathbf{N}} \otimes \mathbf{C}\hat{\mathbf{N}} + \mathbf{F}\mathbf{C}\hat{\mathbf{N}} \otimes \hat{\mathbf{N}}) - 2\Big(\frac{\gamma_n^2}{\lambda_n^2} + 2\Big)\mathbf{F}\hat{\mathbf{N}} \otimes \hat{\mathbf{N}} \tag{A.3}$$

and

$$\frac{\partial \gamma_p^2}{\partial \mathbf{F}} = 2\mathbf{F} - 2\lambda_p^2\mathbf{F}^{-T} + 2\Big(\frac{\gamma_n^2 + \lambda_p^2}{\lambda_n^2} + 1\Big)\mathbf{F}\hat{\mathbf{N}} \otimes \hat{\mathbf{N}} - \frac{2}{\lambda_n^2}(\mathbf{F}\hat{\mathbf{N}} \otimes \mathbf{C}\hat{\mathbf{N}} + \mathbf{F}\mathbf{C}\hat{\mathbf{N}} \otimes \hat{\mathbf{N}}). \tag{A.4}$$

Appendix B

Kinematic tensors of the electromechanical invariants

$$\frac{\partial I_1}{\partial F_{ij}} = 2F_{ij} \tag{B.1}$$

$$\frac{\partial^2 I_1}{\partial F_{ij} \partial F_{kl}} = 2\delta_{ik}\delta_{jl}, \tag{B.2}$$

$$\frac{\partial I_{5e}}{\partial F_{pq}} = -2C_{qj}^{-1} E_j^0 F_{ip}^{-1} E_i^0, \tag{B.3}$$

$$\frac{\partial I_{5e}}{\partial E_i^0} = 2C_{ij}^{-1} E_j^0 \tag{B.4}$$

$$\frac{\partial^2 I_{5e}}{\partial F_{pq} \partial F_{kl}} = 2\left\{ C_{qj}^{-1} E_j^0 F_{ik}^{-1} E_i^0 F_{lp}^{-1} + \left(C_{li}^{-1} E_i^0 F_{qk}^{-1} + F_{ik}^{-1} E_i^0 C_{lq}^{-1} \right) F_{jp}^{-1} E_j^0 \right\}, \tag{B.5}$$

$$\frac{\partial^2 I_{5e}}{\partial F_{pq} \partial E_k^0} = -2 \left(C_{qj}^{-1} E_j^0 F_{kp}^{-1} + C_{qk}^{-1} E_j^0 F_{jp}^{-1} \right), \tag{B.6}$$

$$\frac{\partial^2 I_{5e}}{\partial E_i^0 \partial E_j^0} = 2C_{ij}^{-1}, \tag{B.7}$$

$$\frac{\partial C_{ij}^{-1}}{\partial F_{pq}} = -C_{qj}^{-1} F_{ip}^{-1} - C_{qi}^{-1} F_{jp}^{-1}. \tag{B.8}$$

Appendix C

R-Matrix of the electromechanical instability analysis

The non-zero entries of $\mathbf{R}$ can be written as

$$R_{11} = k_1^2 b\Big(\mathcal{G}_{122}(\mathcal{G}_{122} + \mathcal{G}_{221} - \mathcal{G}_{111}) - (\mathcal{A}_{1122} + \mathcal{A}_{1221} - \mathcal{A}_{1111})\mathcal{E}_{22}\Big),$$

$$R_{12} = k_1^2 b\left(\mathcal{A}_{1121}\mathcal{E}_{22} - \mathcal{G}_{121}\mathcal{G}_{122}\right), \quad R_{13} = -ik_1 b\Big(\mathcal{G}_{111}\mathcal{E}_{22} + \mathcal{G}_{122}\mathcal{E}_{11}\Big),$$

$$R_{14} = ik_1 b\Big(2\mathcal{G}_{122} - (\mathcal{G}_{112} + \mathcal{G}_{121})\mathcal{E}_{22}\mathcal{E}_{12}\Big), \quad R_{15} = ik_1 b\mathcal{E}_{22},$$

$$R_{16} = ik_1 b\Big(\mathcal{G}_{122}(\mathcal{G}_{112} + \mathcal{G}_{121} - \mathcal{G}_{222}) - (2\mathcal{A}_{1112} - \mathcal{A}_{1222})\mathcal{E}_{22}\Big)$$

$$R_{21} = bk_1^2 \mathcal{E}_{22}^{-1}(\mathcal{G}_{122}^2 - \mathcal{A}_{1212}\mathcal{E}_{22})\Big((\mathcal{A}_{1121} - 2\mathcal{A}_{2122})\mathcal{E}_{22} + \mathcal{G}_{222}(\mathcal{G}_{122} + \mathcal{G}_{221} - \mathcal{G}_{111})\Big) -$$
$$(\mathcal{A}_{1222} - \mathcal{E}_{22}^{-1}\mathcal{G}_{122}\mathcal{G}_{222})R_{11},$$

$$R_{22} = -k_1^2\Big\{ b\Big(\mathcal{G}_{122}(\mathcal{A}_{1222}\mathcal{G}_{121} + \mathcal{A}_{1121}\mathcal{G}_{222}) - \mathcal{A}_{1121}\mathcal{A}_{1222}\mathcal{E}_{22} - \mathcal{A}_{1212}\mathcal{G}_{121}\mathcal{G}_{222}\Big) + \mathcal{A}_{2121}\Big\},$$

$$R_{23} = ik_1\Big\{\mathcal{G}_{121} - \Big(\mathcal{A}_{1222}\mathcal{E}_{22}\mathcal{G}_{111} + (\mathcal{A}_{1212}\mathcal{G}_{222} - \mathcal{A}_{1222}\mathcal{G}_{122})\mathcal{E}_{11}\Big)b\Big\},$$

$$R_{24} = -ik_1\Big\{ \Big(\mathcal{E}_{22}\mathcal{A}_{1222}(\mathcal{G}_{112} + \mathcal{G}_{121}) - 2\mathcal{E}_{12}(\mathcal{A}_{1222}\mathcal{G}_{122} + \mathcal{A}_{1212}\mathcal{G}_{222}) - \mathcal{G}_{122}(\mathcal{G}_{112} + \mathcal{G}_{121})\mathcal{G}_{222}\Big)b +$$
$$\mathcal{G}_{122} + \mathcal{G}_{221} \Big\}, \quad R_{25} = ik_1 b(\mathcal{A}_{1222}\mathcal{E}_{22} - \mathcal{G}_{122}\mathcal{G}_{222}),$$

$$R_{26} = -ik_1\mathcal{E}_{22}^{-1}\Big\{ \Big((2\mathcal{A}_{1112} - \mathcal{A}_{1222})\mathcal{E}_{22} - \mathcal{G}_{122}(\mathcal{G}_{112} + \mathcal{G}_{121} - \mathcal{G}_{222})\Big)(\mathcal{A}_{1222}\mathcal{E}_{22} - \mathcal{G}_{122}\mathcal{G}_{222})b -$$
$$(\mathcal{A}_{1122} + \mathcal{A}_{1221} - \mathcal{A}_{2222})\mathcal{E}_{22} - (\mathcal{G}_{112} + \mathcal{G}_{121} - \mathcal{G}_{222})\mathcal{G}_{222}\Big\},$$

$$R_{31} = k_1^2 b\Big((\mathcal{A}_{1111} - \mathcal{A}_{1122} - \mathcal{A}_{1221})\mathcal{G}_{122} + \mathcal{A}_{1212}(\mathcal{G}_{122} + \mathcal{G}_{221} - \mathcal{G}_{111})\Big),$$

$$R_{32} = k_1^2 b\Big(\mathcal{A}_{1212}\mathcal{G}_{121} - \mathcal{A}_{1121}\mathcal{G}_{122}\Big), \quad R_{33} = ik_1 b\Big(\mathcal{G}_{111}\mathcal{G}_{122} - \mathcal{A}_{1212}\mathcal{E}_{11}\Big),$$

$$R_{34} = ik_1 b\Big((\mathcal{G}_{112} + \mathcal{G}_{121})\mathcal{G}_{122} - \mathcal{A}_{1212}\mathcal{E}_{12}\Big), \quad R_{35} = -ik_1 b\mathcal{G}_{122},$$

$$R_{36} = -ik_1 b\Big((\mathcal{A}_{1222} - 2\mathcal{A}_{1112})\mathcal{G}_{122} + \mathcal{A}_{1212}(\mathcal{G}_{112} + \mathcal{G}_{121} - \mathcal{G}_{222})\Big),$$

$$R_{41} = -ik_1, \quad R_{54} = ik_1, \quad R_{66} = 1. \tag{C.1}$$

where $b = (\mathcal{A}_{1212}\mathcal{E}_{22} - \mathcal{G}_{122}^2)^{-1}$.

Bibliography

Agoras, M., Lopez-Pamies, O. and Ponte Castañeda, P. (2009a). A general hyperelastic model for incompressible fiber-reinforced elastomers, *J. Mech. Phys. Solids* **57**: 268–286.

Agoras, M., Lopez-Pamies, O. and Ponte Castañeda, P. (2009b). Onset of macroscopic instabilities in fiber-reinforced elastomers at finite strain, *J. Mech. Phys. Solids* **57**: 1828–1850.

Aravas, N., Cheng, C. and Ponte Castañeda, P. (1995). Steady-state creep of fiber-reinforced composites: Constitutive equations and computational issues, *Int. J. Solids Structures* **32**: 2219–2244.

Bar-Cohen, Y. (2001). EAP history, current status, and infrastructure, *in* Y. Bar-Cohen (ed.), *Electroactive Polymer (EAP) Actuators as Artificial Muscles*, SPIE press, Bellingham, WA, chapter 1, pp. 3–44.

Bertoldi, K. and Boyce, M. C. (2008). Wave propagation and instabilities in monolithic and periodically structured elastomeric materials undergoing large deformations, *Phys. Rev. B* **78**: 184107.

Bertoldi, K. and Gei, M. (2011). Instabilities in multilayered soft dielectrics, *J. Mech. Phys. Solids* **59**: 18–42.

Bhattacharya, K., Li, J. Y. and Xiao, Y. (2001). Electromechanical models for optimal design and effective behavior of electroactive polymers, *in* Y. Bar-Cohen (ed.), *Electroactive Polymer (EAP) Actuators as Artificial Muscles*, SPIE press, chapter 12, pp. 309–330.

Biot, M. A. (1965). *Mechanics of Incremental Deformations*, John Wiley and Sons, New-York.

Budiansky, B. (1983). Micromechanics, *Computers & Structures* **16**: 3–12.

Carpi, F. and DeRossi, D. (2005). Improvement of electromechanical actuating performances of a silicone dielectric elastomer by dispersion of titanium dioxide powder, *IEEE Transactions on Dielectrics and Electrical Insulation* **12**(4): 835–843.

Carpi, F., Salaris, C. and De Rossi, D. (2007). Folded dielectric elastomer actuators, *Smart Materials & Structures* **16**: 300–305.

deBotton, G. (2005). Transversely isotropic sequentially laminated composites in finite elasticity, *J. Mech. Phys. Solids* **53**: 1334–1361.

deBotton, G. (2008). Composites with one and two families of fibers, Presented at the Composites and Polycrystals Mini-Symposium at the SIAM conference on Mathematical aspects of materials science, Philadelphia, PA.

deBotton, G. and Hariton, I. (2006). Out-of-plane shear deformation of a neo-Hookean fiber composite, *Physics Letters A* **354**: 156–160.

deBotton, G., Hariton, I. and Socolsky, E. A. (2006). Neo-Hookean fiber-reinforced composites in finite elasticity, *J. Mech. Phys. Solids* **54**: 533–559.

deBotton, G. and Schulgasser, K. (1996). Bifurcation of orthotropic solids, *J. Appl. Mech., Trans. ASME* **63**: 317–320.

deBotton, G. and Shmuel, G. (2009). Mechanics of composites with two families of finitely extensible fibers undergoing large deformations, *J. Mech. Phys. Solids* **57**: 1165–1181.

deBotton, G. and Shmuel, G. (2010). A new variational estimate for the effective response of hyperelastic composites, *J. Mech. Phys. Solids* **58**: 466–483.

deBotton, G. and Tevet-Deree, L. (2006). Electroactive polymer composites - analysis and simulation, *in* W. D. Armstrong (ed.), *Smart Structures and Materials 2006: Active Materials: Behavior and Mechanics*, Vol. 6170 of *Proc. of SPIE*, San Diego, CA, pp. 2401–2410.

deBotton, G., Tevet-Deree, L. and Socolsky, E. A. (2007). Electroactive heterogeneous polymers: analysis and applications to laminated composites, *Mechanics of Advanced Materials and Structures* **14**: 13–22.

Dorfmann, A. and Ogden, R. W. (2005). Nonlinear electroelasticity, *Acta. Mech.* **174**: 167–183.

Dorfmann, A. and Ogden, R. W. (2010). Nonlinear electroelastostatics: Incremental equations and stability, *International Journal of Engineering Science* **48**: 1–14.

Ericksen, J. L. and Rivlin, R. S. (1954). Large elastic deformations of homogeneous anisotropic materials, *Arch. Rational. Mech. Anal.* **3**: 281–301.

Fleck, N. (1997). Compressive failure of fiber composites, *Advances in Applied Mechanics* **33**: 43–117.

Gei, M., Roccabianca, S. and Bacca, M. (2010). Controlling band gap in electroactive polymer-based structures, *IEEE-ASME Transactions on Mechatronics (in press)* .

Gent, A. N. (1996). A new constitutive relation for rubber, *Rubber Chemistry and Technology* **69**: 59–61.

Geymonat, G., Müller, S. and Triantafyllidis, N. (1993). Homogenization of nonlinearly elastic materials, microscopic bifurcation and macroscopic loss of rank-one convexity, *Arch. Rational. Mech. Anal.* **122**: 231–290.

He, Q. C., Le Quang, H. and Feng, Z. Q. (2006). Exact results for the homogenization of elastic fiber-reinforced solids at finite strain, *J. of Elasticity* **83**: 153–177.

Hill, R. (1972). On constitutive macro-variables for heterogeneous solids at finite strain, *Proc. R. Soc. Lond. A* **326**: 131–147.

Hill, R. and Hutchinson, J. W. (1975). Bifurcation phenomena in the plane tension test, *J. Mech. Phys. Solids* **23**: 239–264.

Horgan, C. and Saccomandi, G. (2002). A molecular-statistical basis for the gent constitutive model of rubber elasticity, *J. of Elasticity* **68**: 167–176.

Huang, C. and Zhang, Q. M. (2004). Enhanced dielectric and electromechanical responses in high dielectric constant all-polymer percolative composites, *adv. func. mater.* **14**: 501–506.

Huang, C., Zhang, Q. M., deBotton, G. and Bhattacharya, K. (2004). All-organic dielectric-percolative three-component composite materials with high electromechanical response, *Applied Physics Letters* **84**: 4391–4393.

Khisaeva, Z. and Ostoja-Starzewski, M. (2006). On the size of rve in finite elasticity of random composites, *J. of Elasticity* **85**: 153–173.

Kittel, C. (2004). *Introduction to Solid State Physics*, 8 edn, Wiley.

Kofod, G., Sommer-Larsen, P., Kornbluh, R. and Pelrine, R. (2003). Actuation response of polyacrylate dielectric elastomers, *Journal of Intelligent Material Systems and Structures* **14**: 787–793.

Lacour, S.-P., Prahlad, H., Pelrine, R. and Wagner, S. (2004). Mechatronic system of dielectric elastomer actuators addressed by thin film photoconductors on plastic, *Sensors and actuators A-physical* **111**: 288–292.

Liu, L., Liu, Y., Zhang, Z., Li, B. and Leng, J. (2010). Electromechanical stability of electro-active silicone filled with high permittivity particles undergoing large deformation, *Smart Materials & Structures* **19**(11).

Lopez-Pamies, O. and Idiart, M. (2010). Fiber-reinforced hyperelastic solids: a realizable homogenization constitutive theory, *J. of Engineering Mathematics* **68**: 57–83.

Lopez-Pamies, O. and Ponte Castañeda, P. (2004). Second-order estimates for the macroscopic response and loss of ellipticity in porous rubbers at large deformations, *J. of Elasticity* **76**: 247–287.

McMeeking, R. M. and Landis, C. M. (2005). Electrostatic forces and stored energy for deformable dielectric materials, *J. Appl. Mech., Trans. ASME* **72**: 581–590.

Merodio, J. and Ogden, R. W. (2002). Material instabilities in fiber-reinforced nonlinearly elastic solids under plane deformation, *Archives of Mechanics (IPPT)* **54**: 525–552.

Merodio, J. and Pence, T. J. (2001). Kink surfaces in a directionally reinforced neo-hookean material under plane deformation: Ii. kink band stability and maximally dissipative band broadening, *J. of Elasticity* **V62**(2): 145–170.

Michel, J. C., Lopez-Pamies, O., Castañeda, P. P. and Triantafyllidis, N. (2007). Microscopic and macroscopic instabilities in finitely strained porous elastomers, *J. Mech. Phys. Solids* **55**: 900–938.

Mockensturm, E. M. and Goulbourne, N. (2006). Dynamic response of dielectric elastomers, *Int. J. Nonlinear Mech.* **41**: 388 – 395.

Molberg, M., Crespy, D., Rupper, P., Nueesch, F., Manson, J., Loewe, C. and Opris, D. (2010). High Breakdown Field Dielectric Elastomer Actuators Using Encapsulated Polyaniline as High Dielectric Constant Filler, *Advanced Functional Materials* **20**(19): 3280–3291.

Moraleda, J., Segurado, J. and LLorca, J. (2009). Finite deformation of incompressible fiber-reinforced elastomers: a computational micromechanics approach, *J. Mech. Phys. Solids* **57**: 1596–1613.

Nestorovic, M. D. and Triantafyllidis, N. (2004). Onset of failure in finitely strained layered composites subjected to combined normal and shear loading, *J. Mech. Phys. Solids* **52**: 941–974.

Ogden, R. W. (1974). On the overall moduli of non-linear elastic composite materials, *J. Mech. Phys. Solids* **22**: 541–553.

Ogden, R. W. (1997). *Non-Linear Elastic Deformations*, Dover Publications, New York.

Ogden, R. W. (2008). Nonlinear elasticity and fibrous structure in arterial wall mechanics, *Lecture Notes for Summer School on Modeling and Computation in Biomechanics*, Graz University of Technology, Austria.

O'Halloran, A., O'Malley, F. and McHugh, P. (2008). A review on dielectric elastomer actuators, technology, applications, and challenges, *J. Appl. Phys.* **104**: 071101.

Pelrine, R., Kornbluh, R., Pei, Q.-B. and Joseph, J. (2000). High-speed electrically actuated elastomers with strain greater than 100%, *Science* **287**: 836–839.

Plante, J.-S. and Dubowsky, S. (2006). Large-scale failure modes of dielectric elastomer actuators, *Int. J. Solids Struct.* **43**: 7727–7751.

Qiu, G. and Pence, T. (1997). Loss of ellipticity in plane deformation of a simple directionally reinforced incompressible nonlinearly elastic solid, *J. of Elasticity* **49**: 31–63.

Rosen, B. W. (1965). Mechanics of composite strengthening, *Fibre Composite Materials*, Am. Soc. Metals, Ohio, pp. 37–75.

Rudykh, S., Bhattacharya, K. and deBotton, G. (2012a). Multiscale instabilities in soft heterogeneous dielectrics.

Rudykh, S., Bhattacharya, K. and deBotton, G. (2012b). Snap-through actuation of thick-wall electroactive balloons, *Int. J. Nonlinear Mech.* **47**: 206–209.

Rudykh, S. and deBotton, G. (2011). Stability of anisotropic electroactive polymers with application to layered media, *Z. Angew. Math. Phys.* **62**: 1131–1142.

Rudykh, S. and deBotton, G. (2012). Instabilities of hyperelastic fiber composites: micromechanical versus numerical analyses, *J. of Elasticity* **106**: 123–147.

Rudykh, S., Lewinstein, A., Uner, G. and deBotton, G. (2011). Giant enhancement of the electromechanical coupling in soft heterogeneous dielectrics, *Arxiv preprint arxiv:1105.4217*
.

URL: *http://arxiv.org/abs/1105.4217v1*

Shmuel, G. and deBotton, G. (2010). Out-of-plane shear of fiber composites at moderate stretch levels, *J. of Engineering Mathematics* **68**: 85–97.

Singamaneni, S., Bertoldi, K., Chang, S., Jang, J., Young, S. L., Thomas, E. L., Boyce, M. C. and Tsukruk, V. V. (2009). Bifurcated Mechanical Behavior of Deformed Periodic Porous Solids, *Advanced Functional Materials* **19**(9): 1426–1436.

Stoyanov, H., Kollosche, M., Risse, S., McCarthy, D. and Kofod, G. (2011). Elastic block copolymer nanocomposites with controlled interfacial interactions for artificial muscles with direct voltage control, *Soft Matter* **7**(1): 194–202.

Suo, Z., Zhao, X. and Greene, W. H. (2008). A nonlinear field theory of deformable dielectrics, *J. Mech. Phys. Solids* **56**(2): 467–486.

Tevet-Deree, L. (2008). *Electroactive Polymer Composites - Analysis and Simulation*, PhD thesis, Ben-Gurion University.

Tian, L., Tevet-Deree, L., deBotton, G. and Bhattacharya, K. (2012). Dielectric elastomer composites, *J. Mech. Phys. Solids* **60**: 181–198.

Toupin, R. A. (1956). The elastic dielectric, *Arch. Rational. Mech. Anal.* **5**: 849–915.

Treloar, L. R. G. (1975). *The Physics of Rubber Elasticity*, Clarendon Press, Oxford.

Triantafyllidis, N. and Maker, B. N. (1985). On the comparison between microscopic and macroscopic instability mechanisms in a class of fiber-reinforced composites, *J. Appl. Mech., Trans. ASME* **52**: 794–800.

Triantafyllidis, N., Nestorovic, M. D. and Schraad, M. W. (2006). Failure surfaces for finitely strained two-phase periodic solids under general in-plane loading, *J. Appl. Mech., Trans. ASME* **73**(3): 505–515.

Wang, Q., Zhang, L. and Zhao, X. (2011). Creasing to cratering instability in polymers under ultrahigh electric fields, *Phys. Rev. Lett.* **106**(11): 118301.

Yeoh, O. H. (1993). Some forms of the strain-energy function for rubber, *Rubber Chemistry and Technology* **66**: 754–771.

Zhang, Q. M., Li, H., Poh, M., Xia, F., Cheng, Z.-Y., Xu, H. and Huang, C. (2002). An all-organic composite actuator material with a high dielectric constant, *Nature* **419**: 284–289.

Zhu, J., Cai, S. and Suo, Z. (2010). Nonlinear oscillation of a dielectric elastomer balloon, *Polymer International* **59**(3): 378–383.

תקציר

עבודה זו דנה באספקטים תיאורטיים של התפתחות של אי יציבות בחומרים דיאלקטריים הטרוגניים אשר יכולים לעבור דפורמציות גדולות. קריטריון כללי הינו מוכנס על מנת לזהות מקרה גבולי של אי יציבות מקרוסקופית.   אי יציבות בכל הסקאלות הנם נקבעים ע״י יישום בשיטת Bloch-Floquet לחומרים מחזוריים. הנני מתחיל עם בעיה מכאנית טהורה ופיתוח קריטריון להתחלת אי יציבות   מקרוסקופית בחומרים מרוכבים מרחבים עם סיבים מכוונים לכיוון מועדף שמפולגים באופן אקראי. לפיכך, ניתן להצהיר שהחומר המרוכב נכשל כאשר הלחיצה לכיוון הסיבים מגיע לערך הקריטי הנתון ע״י נוסחא מפורשת בצורה קומפקטית. התוצאות הנן מאושרות ע״י אימות בדמיה מרחבית בשיטת האלמנט הסופי. כאשר למטרה הזו פותח אלגוריתם ייחודי המאפשר לזהות את ההתחלה של אי יציבות.

במהלך המחקר התבצע האנליזה המצומדת האלקטרו-מכאנית במונחים המתאימים מבחינה פיזיקאלית דהינו במונחים של שדה חשמלי במצב לא מעוות. המוטיבציה לכך נובעת מאופן השליטה בעירור חשמלי בניסויים ויישומים אפשריים. בנוסף לכך, בוצע אנליזה במונחים חילופיים כלומר, במונחים של הזזת חשמליות ביחס למצב הייחוס.

התקבל פתרון מדויק ליציבות של חומרים אלקטרו-אקטיביים רב שכבתיים עם פאזות מחומר היפראלסטי neo-Hookean . יתרה על כך, התקבל קריטריון להתחלת אי יציבות מיקרוסקופית בחומרים רב שכבתיים עם פאזות מחומר אנאיזוטרופי.   בעזרת הקריטריון התגלתה חשיבות רבה של מיקרו מבנה של החומרים בהתפתחות של אי יציבות, כלומר

i. אי יציבות מקרוסקופית שולטת בחומרים עם אחוז נפחי בינוני של הפאזה הקשיחה

ii. אי יציבות המאופיינת על״י עורכי גל קטנים מופיעה בחומרים עם אחוז נפחי נמוך של הפאזה הקשיחה

iii. אי יציבות בסקאלות סופיים של מיקרו מבנה של החומר מופיעה בחומרים עם אחוז נפחי גבוהה של הפאזה הקשיחה

אי יציבות מהסוג iii הינה חדשה ומופיע אך ורק בבעיה מצומדת. התחומים של אי יציבות מתפתחים עם שינוי בעירור חשמלי: גדלים או קטנים, נפגשים ומתאחדים באופן ייחודי.

לבסוף, קיבלתי פתרון מדויק עבור בלונים כדוריים עבי דופן העשויים מחומר אלקטרו-אקטיבי וניתנים לעירור על״י לחץ פנימי והפרש פוטנציאל חשמלי. הנני מדגים יישומים אפשריים של תופעות של אי יציבות במבנים האלה ומציע מכאניזם למיקרו משאבה.

פולימרים אלקטרואקטיביים מרוכבים: יציבות מקרוסקופית ומיקרוסקופית

מחקר לשם מילוי חלקי של דרישות לקבלת
תואר "דוקטור לפילוסופיה"

מאת

סטפן   רודיך

הוגש לסנאט אוניברסיטת בן גוריון בנגב

אישור המנחה_____

אישור דיקן בית הספר ללימודי מחקר מתקדמים ע״ש קרייטמן_____

אלול תשע״ב   אוקטובר 2011

באר שבע

פולימרים אלקטרואקטיביים מרוכבים: יציבות מקרוסקופית ומיקרוסקופית

מחקר לשם מילוי חלקי של דרישות לקבלת
תואר ״דוקטור לפילוסופיה״

מאת

סטפן   רודיך

הוגש לסנאט אוניברסיטת בן גוריון בנגב

אלול תשע״ב   אוקטובר 2011

באר שבע